Adsorption and Electrokinetics at Silica-Electrolyte Interfaces

A Molecular Simulation Study

Döpke, M.F.

DOI
10.4233/uuid:65db94ec-c7b6-4c54-82b8-273dc18b3081

Publication date
2022

Document Version
Final published version

Citation (APA)
Döpke, M. F. (2022). *Adsorption and Electrokinetics at Silica-Electrolyte Interfaces: A Molecular Simulation Study*. [Dissertation (TU Delft), Delft University of Technology]. https://doi.org/10.4233/uuid:65db94ec-c7b6-4c54-82b8-273dc18b3081

Adsorption and Electrokinetics at Silica-Electrolyte Interfaces

A Molecular Simulation Study

Adsorption and Electrokinetics at Silica-Electrolyte Interfaces

A Molecular Simulation Study

Proefschrift

ter verkrijging van de graad van doctor
aan de Technische Universiteit Delft,
op gezag van de Rector Magnificus prof. dr. ir. T.H.J.J. van der Hagen,
voorzitter van het College voor Promoties,
in het openbaar te verdedigen op donderdag 26 Januari 2023 om 15:00 uur

door

Max Felipe DÖPKE

Master of Science in Aerospace Engineering,
Technische Universiteit Delft, Nederland,
geboren te Troisdorf, Duitsland.

Dit proefschrift is goedgekeurd door de

Promotor: prof. dr. ir. J.T. Padding
Copromotor: dr. R.M. Hartkamp

Samenstelling promotiecommissie:

Rector Magnificus,	voorzitter
Prof. dr. ir. J.T. Padding	Technische Universiteit Delft, promotor
Dr. ir. R.M. Hartkamp	Technische Universiteit Delft, copromotor
Onafhankelijke leden:	
Prof. dr. R. Netz	Freie Universität Berlin, Duitsland
Prof. dr. M. Předota	Jihočeská univerzita v Českých Budějovicích, Tsjechische Republiek
Prof. dr. ir. R.H.H.G. van Roij	Universiteit Utrecht
Prof. dr. E.A. Pidko	Technische Universiteit Delft
Prof. dr. F.G. Mugele	Universiteit Twente
Prof. dr. ir. R. Pecnik	Technische Universiteit Delft, reservelid

Keywords: Molecular Simulation, Molecular Dynamics Simulation, Interface, Solid-Fluid Interface, Amorphous silica, Electrolyte, Silica-Electrolyte Interface
Printed by: Ridderprint, Ablasserdam

ISBN 978-94-6384-404-8

An electronic version of this dissertation is available at
http://repository.tudelft.nl/.

Contents

Summary

Experimentally investigating the nanoscale behavior at oxide-electrolyte interfaces has proven to be extremely challenging. Molecular Dynamics (MD) simulations have arisen as a potential computational alternative to gain atomic level insights at these interfaces. But how accurately do these simulations represent the physics and chemistry at the interface? In many situations we do in fact not know. Validation at the interface remains challenging. The force fields used in MD simulations, that describe the inter-particle interactions, are generally optimized for purposes deviating considerably from interfaces. Yet, these same force fields are blindly used to model surface-fluid interactions, yielding wildly varying results of for example ion adsorption. This dissertation tackles the problem of simulating interfaces by critically looking at MD simulations and proposing novel solutions, both for MD simulations in general and specifically targeting their validity and limitations with regards to modeling interfaces.

In Ch. 2, various water and ion force field parameters are combined in order to give a perspective of the typical mix-and-match approach that is frequent in the literature, and to determine unambiguously, from the chosen selection of force fields, the best combination of ion and water force fields for a given set of properties. In particular, the combinations were assessed on hydration properties, ion dynamics, and finite concentration effects such as solubility and ion pairing. Having determined the best combinations of parameters for the fluid electrolyte phase, a realistic silica surface is prepared by heating and cooling a β-cristobalite and functionalizing the surface as described in Ch. 3. Subsequently, the amorphous silica surface and the fluid electrolyte are put in contact to investigate the effect of surface roughness on electrolyte mixtures. Specifically, in Ch. 3 the ion-specificity of a the surface is assessed with respect to the ion hydration properties. For example, Ca^{2+} is expected to adsorb preferentially at a surface compared to Na^{+}, owing to their higher coulombic charge. However, the surface roughness is found to be able to pose steric hindrances to the ion hydration shells, such that some surface sites display preferential adsorption of Na^{+} ions. While this exact mechanism cannot be observed in experiments owing to its complexity and small time and length scales, several studies have suggested such counter intuitive ion-specificity. These results thus provide a viable hypothesis to shed light on these experiments.

In an attempt to bridge the gap between experiments and simulations in a more tangible way, in Ch. 4, we explore opportunities within an electrokinetic framework. In particular, we find that the conditions at which ζ-potential is zero serves as an ideal control point due to its unique definition. Following the Helmholtz-Smoluchowski theory, the conditions at which a zero ζ-potential is obtained are independent of the solvent dielectric permittivity and viscosity and the functional form relating to each electrokinetic measurement technique, thereby, providing a control point that is unambiguously defined, while at the same time eliminating errors and uncertainties

from the modeled solvent and/or confinement effects in experiments and/or simulations. Exploiting this fact, we then show how the experimental conditions at which $\zeta = 0$ can be reproduced for a $CaCl_2$ electrolyte in contact with amorphous silica by a simple adjustment of the Lennard-Jones ion-surface interactions. While the work here is limited to a single pH and concentration at which $\zeta = 0$, an infinite number of conditions can be created at which $\zeta = 0$ by changing the pH and/or concentration accordingly. This work thus provides the stepping stone to optimize and/or validate the electrokinetic properties of MD simulations directly with experiments over a large pH and concentration range.

Finally, in Ch. 5 limitations of MD simulations regarding surface proton exchange reactions are investigated. Typically, these reactions can only be modeled by reactive MD simulation, but their computational cost limits the properties that can be studied. To overcome this limitation, we first develop a novel framework to include surface reactions in MD simulations at no additional computational cost, and second investigate their impact on the interfacial fluid structure and dynamics. The surface reactions are mimicked in our approach by turning on (protonation) and off (deprotonation) the proton interactions without explicitly adding or removing the atom, nor creating and breaking a bond. Using this simple, yet robust approach, we then show that reaction rates in the same order of magnitude as predicted by more computationally expensive dissociative MD simulations can have a non-negligible impact on the electric double layer structure and dynamics. In particular, we observe a shift from specific to non-specific ion adsorption and a reduction of ion residence times as the reaction rate increases. We then discuss the limiting cases of a non-reactive and a very reactive surface in the framework of the Boltzmann equation, providing a framework to rationalize the observed impact of protolysis reactions.

Samenvatting

Experimenteel onderzoek naar het gedrag van oxide-elektrolyt-oppervlakken op nanoschaal is een grote uitdaging. Moleculaire dynamica (MD) simulaties lijken een kansrijk computationeel alternatief voor het verkrijgen van nieuwe inzichten over wat er gebeurt op atomair niveau aan deze oppervlakken. Maar hoe nauwkeurig is de fysische en chemische weergave van deze simulaties? In veel situaties hebben we geen idee, het valideren blijft een uitdaging. De krachtvelden die gebruikt worden in MD simulaties om interacties tussen deeltjes te beschrijven zijn vaak geoptimaliseerd voor andere systemen dan oppervlakken. Toch worden deze krachtvelden vaak direct overgenomen voor het modeleren van oppervlak-vloeistofinteracties. Dit resulteert in sterk afwijkende resultaten voor bijvoorbeeld de adsorptie van ionen. In dit proefschrift wordt kritisch gekeken naar het simuleren van interfaces met MD simulaties en worden nieuwe oplossingen geboden voor zowel simulaties in het algemeen als hun betrouwbaarheid en beperkingen voor oppervlakken.

In Hoofdstuk 2 worden verschillende krachtvelden voor water en ionen gecombineerd om een overzicht te geven van de typische mix-en-matchaanpak die vaak gebruikt wordt. Op die manier wordt de beste keuze gemaakt van krachtvelden voor het voorspellen van bepaalde verzamelingen van eigenschappen. In het bijzonder wordt daarbij gekeken naar hydratie-eigenschappen, dynamica van ionen en de effecten van de eindige concentratiegrootte zoals oplosbaarheid en ionenassociatie. Met de gekozen krachtvelden voor de elektrolytische vloeistof wordt vervolgens een silica-oppervlak gecreëerd door het verhitten en afkoelen van een β-cristobaliet zoals beschreven in Hoofdstuk 3. Daarna worden het amorfe silica-oppervlak en de elektrolytische vloeistof samengebracht om onderzoek te doen naar het effect van de ruwheid van het oppervlak op elektrolytische vloeistoffen. Bovendien wordt in Hoofdstuk 3 gekeken naar het verband tussen de *ion specificity* van het oppervlak en de hydratie-eigenschappen van het ion. Zo zou men verwachten dat Ca^{2+} makkelijker adsorbeert aan het oppervlak dan Na^{+} vanwege de grotere lading van het ion. Het blijkt echter dat de ruwheid van het oppervlak sterische hindering kan veroorzaken in de hydratieschillen van het ion waardoor sommige *sites* makkelijker Na^{+}-ionen adsorberen. Hoewel het precieze mechanisme achter dit gedrag lastig waar te nemen valt in experimenten vanwege de complexiteit en kleine tijd- en lengteschalen, wordt in een aantal onderzoeken dit principe wel als verklaring gegeven voor deze onverwachte adsorptie-eigenschappen. De resultaten van het onderzoek dat hier wordt gepresenteerd dragen dus bij aan de onderbouwing van de verklaring voor het waargenomen gedrag.

In Hoofdstuk 4 wordt een poging gedaan om de parallel tussen experimenten en simulaties tastbaarder te maken door gebruik te maken van een elektrokinetisch *framework*. Wanneer de ζ-potentiaal nul is, zien we dat de thermodynamische omstandigheden zich prima lenen als controlepunt vanwege de unieke definitie. Vanuit

de Helmholtz-Smoluchowski theorie volgt dat die omstandigheden onafhankelijk zijn van de diëlektrische permitiviteit en viscositeit van het oplosmiddel en de functionele vorm met betrekking tot elke elektrokinetische meettechniek. Daardoor wordt een eenduidig controlepunt vastgelegd en worden tegelijkertijd fouten en onzekerheden weggenomen van het gemodelleerde oplosmiddel en/of eindige grootte-effecten in experimenten en/of simulaties. Met gebruik van deze kennis wordt dan aangetoond hoe de omstandigheden van een experiment met $\zeta = 0$ kunnen worden gereproduceerd voor $CaCl_2$ en amorf silica door een eenvoudige aanpassing van de Lennard-Jones parameters voor de ion-oppervlakte-interacties. Hoewel het werk hier gebonden is aan één enkele pH-waarde en concentratie, zodat $\zeta = 0$, kunnen er oneindig veel situaties worden gecreëerd door de pH-waarde en concentratie op de juiste manier te kiezen. Er wordt hier dus een eerste stap gezet voor het optimaliseren en/of valideren van elektrokinetische eigenschappen in MD simulaties direct vanuit experimenten met verschillende pH-waarden en concentraties.

In hoofdstuk 5 worden tenslotte de beperkingen van MD simulaties onderzocht op het gebied van oppervlakte-proton reacties. Deze reacties kunnen typisch alleen gemodelleerd worden met reactieve MD simulaties. De eigenschappen die hiermee onderzocht kunnen worden zijn echter beperkt vanwege de hoge rekentijd die hiervoor nodig is. Daarom ontwikkelen we een nieuw *framework* om de oppervlaktereacties te simuleren zonder extra rekentijd, en onderzoeken we de invloed van deze reacties op de vloeistofstructuur aan het oppervlak en de dynamica. De oppervlaktereacties worden gemodelleerd door de protoninteracties aan te zetten (protonering) en uit te zetten (deprotonering) zonder het atoom te verwijderen of bindingen te verbreken. Met deze methode laten we zien dat de reactiesnelheden, die van dezelfde ordegrootte zijn als bepaald in dissociatieve MD simulaties die meer rekenkracht vereisen, een niet-verwaarloosbaar effect hebben op de elektrische dubbele laag structuur en dynamica. In het bijzonder nemen we een verschuiving waar van specifiek naar niet-specifieke ion-adsorptie en een kortere duur van ion-opname als de reactiesnelheid hoger is. We bekijken dan de limietgevallen, niet-reactieve en sterk reactieve oppervlakken, in het licht van de Boltzmann-vergelijking die ons handvatten biedt voor een beter begrip van het waargenomen gedrag in protolyse.

1

Introduction

After another rainy day in The Netherlands, the people and animals, the trees and houses, and the cars and streets, are all wet. Yet, it was a day of light rain. No puddles or water streams are found anywhere. Also not on the stone tiles in my garden (Fig. 1.1). The tiles adsorbed all the water in a more or less sponge-like fashion. The same rain water however, forms droplets on the *Hedera Helix* leaves in my backyard, as if an invisible layer was keeping the water inside a balloon (Fig. 1.1). The difference between the tiles of the footpath and *Hedera* leaves are their surface properties. The stone tiles are *hydrophilic*, which derives from the greek *hydro*, meaning water, and *philic* meaning love. As a result, water molecules feel attracted to the surface wetting the tiles, making them look wet. In contrast, the *Hedera Helix* leaves are *hydrophobic*, which translates to water-fearing, resulting in water molecules feeling repelled and forming droplets on the surface. While the effects of water on tiles and *Hedera* leaves are visible to the naked eye, the hydrophilicity/hydrophobicity of a surface is determined by the surface chemistry at the nanoscale. In particu-

Figure 1.1: Photo of a *Hedera Helix* leave on stone tiles taken in my backyard after a rainy day.

lar, the atomic interactions between surface atoms and water molecules. Studying and understanding these interactions however, is not trivial. Experimental techniques generally lack the spatial and/or temporal resolution, while the realism of many computational methods is questionable [1]. For example, particle-based simulations can shed light onto time and length scales not available in experiments, but their parametrization typically requires the difficult to obtain representative experimental data. A symbiotic relationship between experiments and simulations should thus yield a very promising prospect to better understand interfaces. Yet, two severe bottlenecks are found that currently hinder a harmonious relationship:

1. a lack of detailed insights from experiments complicates the development and parametrization of computational methods that can capture the intricacies of interfaces,

2. the available computational power limits the level of detail and system size that can be modeled.

In this dissertation, we will tackle both these bottlenecks focusing on Molecular Dynamics (MD) simulations by first establishing the state of the art in simulating interfaces (Chs. 2 and 3), second defining a framework to validate the modeled interface (Ch. 4), and third expanding the level of detail modeled at no additional computational cost (Ch. 5).

But first, a few key concepts will be introduced and discussed in this introduction followed by a more detailed outline of the present work.

1.1. The Solid-Liquid Interface

Solid-liquid interfaces are omnipresent in nature and central to many scientific fields such as colloid and materials science, phase separation and catalysis, and electrochemistry and energy harvesting. A better understanding of interfaces can thus potentially lead to improved designs of many devices including batteries, osmotic power membranes, drug delivery capsules or nuclear waste disposal sites. For example, consider that nuclear waste is typically disposed of in metal bins that are subsequently stored underground, often in old salt mines or in especially constructed concrete bunkers. The idea of this approach is obviously to avoid our ecosystem from being exposed to nuclear waste. Unfortunately, both the metal containers and the underground storage facilities corrode, posing serious environmental and health risks. It is thus of paramount importance to design the nuclear waste bins and disposal sites to minimize dissolution. For drug delivery capsules the problem may occasionally be reversed. Imagine a drug designed to be taken orally and to dissolve in the stomach. In this case, the capsule needs to be designed to dissolve in specific environments (stomach). Finally, consider a lithium ion battery, in which lithium moves from one side (anode) to the other (cathode), and vice-versa, when charging/discharging the battery. This repeated motion of ions over time, leads to so called dendrite growth, where the ions slowly build up on the anode. As a result, fewer mobile ions are left reducing the battery performance, and on top of that if the

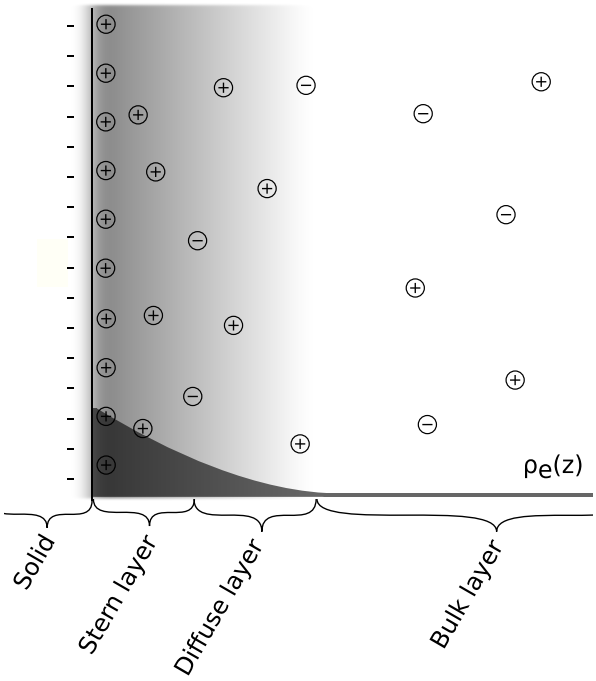

Figure 1.2: Schematic of an idealized solid-liquid interface. The solid in this case is negatively charged

dendritic lithium reaches the cathode a short circuit occurs, essentially killing the battery. Improving our understanding of solid-liquid interfaces is thus hugely important for the scientific community, with impacts reaching our every day lives. But how do these interfaces look like at the nanoscale? Typically, the solid surface will assume a given surface charge, which depends on the material and surrounding conditions, such as temperature and pH, and the fluid will layer itself at the interface. Water molecules will either orient themselves towards or away from the surface, and ions will feel attracted or repelled, depending on their charge. The resulting interface is thus the surface with a surface charge, layered water molecules, and layered ions as shown in Fig. 1.2.

The fluid particles within the interface, can further be divided into layers [2, 3]. The layer nearest to the surface is called the Stern layer, and is considered to consist of immobile particles, that are tightly connected to the surface. The layer to the right of the Stern layer in Fig. 1.2 is the diffuse layer. In this layer particles are mobile, but experience a certain impact from the surface. For example, in the case as shown in Fig. 1.2, the amount of cations will exceed the amount of anions in this layer, resulting in a charge imbalance, and the water molecules will still experience an orientational preference. Additionally, it is often argued that the fluid properties in this layer are neither those of the mobile bulk fluid, nor those of the immobile Stern layer, but somewhere in between [1]. Finally, the fluid particles further away from the surface are considered to be part of the bulk. In other words, the particles

within the bulk are not influenced by the presence of the surface, i.e. the number of anions and cations is similar, and the generally known fluid properties such as the viscosity are assumed to reign in this layer.

The drawing in Fig. 1.2 might lead the uninitiated reader to believe that the interface is fairly understood, but nothing could be further from the truth. The picture presented in Fig. 1.2 is quite idealized. The surface is flat, and both anions and cations are of the same valency and size. In real life however, surfaces are not perfectly flat. Consider for example the stones in Fig. 1.1, which when touched by a human finger feel rough. This roughness also continues for most materials on the nanoscale. The layering as described in Fig. 1.2 thus starts to break down, and locally the layers may overlap. Additionally, most aqueous solutions contain a multitude of different salts, with different sizes and valencies, which compete to adsorb at the surface. Which salt will adsorb however, depends on many factors, which are not all known and/or understood. Despite these clear shortcomings however, most theoretical models that interpret the interface are based on the idealized interpretation as given in Fig. 1.2. But how can we then obtain a better picture of the interface, including the all the intricacies of the interface?

Starting from a classical approach, a scientist would start by observing the interface. For example the scientist may put the interface under a microscope or use his/her own finger to feel any properties at the interface. This empirical approach also leads to the most common experimental methods, which broadly can be classified into optical methods, touch based methods, and electrokinetic methods.

In **optical methods**, specific properties are observed using imaging devices. In the most basic form, cameras are used to record water droplets on a surface. To gain insights at the nanoscale however, more advanced methods are needed. These can broadly be defined as reflecting light beams on a surface as shown in red in Fig. 1.3, and measuring for example the wavelength, frequency, intensity and/or angle of the reflected beams [4]. From these measurements, for example the surface structure, as well as the orientation of water molecules near the surface can be inferred. The reflected beams however essentially only provide information about the vibrations of atoms, and thus cannot provide full atomistic positions as given in Fig. 1.2.

As mentioned above, **contact methods** work in a similar manner as when our fingers touch an object such as the stones or leaf of Fig. 1.1 However, our fingers are fairly large, and cannot provide any details of the interface below a few mm. In order to study interfaces, a sort of needle is thus used that is passed over the surface to measure all the individual hills and ravines of the surface as shown in Fig. 1.3. This approach is known as Atomic Force Microscopy (AFM) [5], in which a needle with a tip radius in the order of a few nm (1 nm = 1×10^{-6} mm) is typically used. As becomes obvious when passing a needle over one's skin, this method is however quite intrusive, the surface feels the needle, and the needle may thus alter the interface at every pass, such that some scientist consider that only transient properties can be measured. As a result, the properties that can be obtained using AFM, are limited to for example determining the surface charge and/or calculating the dissolution rate. Additionally, the scientific community is at odds whether the AFM tip (needle) is in contact with the surface, or one of the first layers of water molecules. Think for

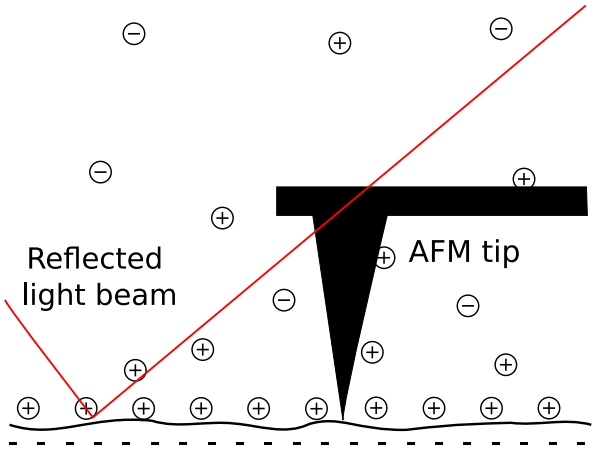

Figure 1.3: Simplified schematic of a surface when exposed to a light beam (red) to be reflected in an optical experimental method such as non-linear spectroscopy and an Atomic Force Microscopy tip passing over the surface.

example of the humidity on our fingers when touching the brick. Do we really touch the brick, or only the water between the brick and our fingers?

The last class of experimental methods discussed here are the **electrokinetic methods** [6]. In essence, these methods exploit the fact that a surface tends to attract either positive or negative ions, and repel the other ones. This in turn generates a charge imbalance in the diffuse layer as shown in Fig. 1.2, where more cations than anions are found near the surface. When applying an external force to the fluid tangential to the surface, such as a pressure gradient, the fluid will move parallel to the surface, and drag ions along. Owing to the distribution of mobile and immobile ions (see for example Fig. 1.2 where in the diffuse layer more cations are mobile), more cations than anions will move along with the fluid inducing an electric current. Finally, this current is measurable, and can be used to infer various properties of the interface, such as the charge within the diffuse layer and/or the surface charge. Thus again, individual atomic positions cannot be determined with these methods.

As an alternative to classical experimental methods based on empiricism and observations, simulations have presented themselves as a viable alternative to interpret and observe nature. This is also the case for solid-liquid interfaces, which at a nanoscale can be studied best using molecular modeling, a technique employed to model and/or mimic the behavior of particles/molecules. Within Molecular Modeling, a distinction can further be made between quantum chemistry [7] and classical molecular mechanics methods. Within quantum chemistry, the smallest individual units are typically electrons surrounding lumps that include protons and neutrons. Within classical molecular mechanics [8], which involves the use of classical Newtonian mechanics, atoms or molecules are typically treated as the smallest individual units. It is within the second group, classical molecular mechanics, that the length- and time-scales relevant for this dissertation (from angstrom to nanometers and from

femtoseconds to nanosecons) are generally studied, using so-called Molecular Dynamics (MD) simulations. It is these simulations, that will also be used throughout this work and are therefore introduced in the next section.

1.2. Molecular Dynamics Simulations

Molecular Dynamics (MD) is a particle-dynamics based computational technique that analyzes the interactions between particles (can be atoms and/or molecules) following classical Newtonian mechanics [8]. It falls within the big picture of computational methods between quantum and meso-scale approaches as shown in Fig. 1.4. Based on the interactions between particles, these will experience a certain force $\mathbf{F}_i$ that causes a motion following Newton's second law $\mathbf{F}_i = m_i\mathbf{a}_i$ (m_i being the mass or particle i and $\mathbf{a}_i$ being the acceleration of particle i), giving rise to the dynamic evolution of the system or trajectories:

$$\frac{d\mathbf{r}_i}{dt} = \mathbf{u}_i \tag{1.1}$$

$$\frac{d\mathbf{u}_i}{dt} = \frac{\mathbf{F}_i}{m_i}. \tag{1.2}$$

From these trajectories (particle positions $\mathbf{r}_i$ and velocities $\mathbf{u}_i$ for each particle i over time t), various thermodynamic, structural and dynamic properties can be calculated with the help of statistical mechanics. For example, ion adsorption can be determined based on the ion position with respect to surface atoms, the temperature is derived from particle vibrations and the pressure is given by the particle density within a given region as explained in more detail below. Equivalently, system conditions such as the temperature and pressure can be controlled by scaling the particle velocities and positions as will be discussed later. MD simulations thus provide a powerful bottom-up approach to attain detailed atomic level insights, where global properties at a macroscopic level result directly from the interactions at the microscopic level.

Integrating the system of Eqs. (1.1) and (1.2) numerically in time advancing time t with a time step Δt O(fs)) using a truncated Taylor series expansion and leapfrog integration yields the famous velocity-Verlet algorithm

$$\mathbf{r}_i(t+\Delta t) = \mathbf{r}_i(t) + \mathbf{u}_i(t)\Delta t + \frac{\mathbf{F}_i(t)}{2m_i}(\Delta t)^2 \tag{1.3}$$

$$\mathbf{u}_i(t+\Delta t) = \mathbf{u}_i(t) + \frac{\mathbf{F}_i(t) + \mathbf{F}_i(t+\Delta t)}{2m_i}\Delta t, \tag{1.4}$$

where the force is given by

$$\mathbf{F}_i = -\frac{dU}{d\mathbf{r}_i}, \tag{1.5}$$

with U being the potential energy determined by the inter-particle interactions.

Two main types of inter-particle interactions can be defined, bonded and non-bonded interactions. Non-bonded interactions are those that occur between particles that are not linked by covalent bonds, for example, between different water

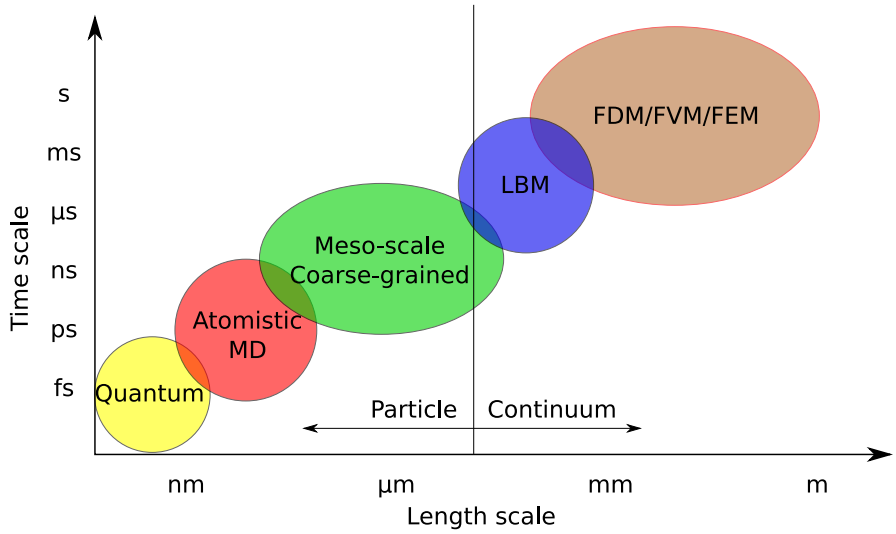

Figure 1.4: Schematic of computational techniques at different time and length scales. The acronyms are as follows: Molecular Dynamics, Lattice Botlzmann Method, Finite Difference Method, Finite Volume Method, Finite Element Method.

molecules or ions, and bonded interactions are those that result from covalent bonds, for example, the interaction between oxygen and hydrogen within the same water molecule. The most common types of non-bonded interactions are the van der Waals attraction and Pauli repulsion, expressed together by the Lennard Jones (LJ) potential, and Coulombic (electrostatic) forces. The most common bonded interactions are spring-like constraints on bonds and angles. The addition of both non-bonded and bonded interactions results in the potential energy

$$U = \sum_{\text{non-bonded},ij} \underbrace{\left\{4\epsilon_{ij}\left[\left(\frac{\sigma_{ij}}{|\mathbf{r}_{ij}|}\right)^{12} - \left(\frac{\sigma_{ij}}{|\mathbf{r}_{ij}|}\right)^{6}\right]}_{\text{LJ}} + \underbrace{\frac{q_i q_j}{4\pi\varepsilon_0\varepsilon_r|\mathbf{r}_{ij}|}\right\}}_{\text{Coulomb}} + \underbrace{\sum_{\text{bonds}} \frac{1}{2}k_b\left(r_b - r_{b0}\right)^2 + \sum_{\text{angles}} \frac{1}{2}k_\theta\left(\theta - \theta_0\right)^2}_{\text{bonded}}. \tag{1.6}$$

In this expression, the summation $\sum_{\text{non-bonded},ij}$ indicates that non-bonded interactions of a particle i with respect to all other particles $j \neq i$ are pairwise additive.

The LJ potential (first term in Eq. (1.6)) describes the distance dependent attraction (van der Waals) and repulsion (Pauli) that occurs between 2 non-covalently bonded atoms/molecules due to their electron clouds. At short distances electron clouds overlap resulting in a strong repulsion, while as the distance increases, particles attract each other as shown in Fig. 1.5. ϵ and σ represent respectively the depth of potential or dispersion energy and distance at which the particle potential

is zero.

The Coulombic interaction between 2 charged and non-covalently bonded particles i and j is given by the second term in Eq. (1.6), with ε_0 and ε_r being the vacuum and relative dielectric permittivity, respectively. Equally charged particles will repel each other and differently charged particles will attract each other as shown in Fig. 1.5.

Bonded interactions (third and fourth term in Eq. (1.6)) follow the principle of harmonic springs (other possibilities exist, but are not used throughout this work). A corrective energy is applied based on the deviation from an equilibrium position, $(r_b - r_{b0})^2$ for bonds and $(\theta - \theta_0)^2$ for angles, and a given spring constant k (subscript b for bonds and θ for angle).

From the inter-particle interactions described above, ϵ, σ, q, k_b, r_{b0}, k_θ and θ_0 are all parameters that need to be described per particle i, particle pair ij and in the case of an angle per group of 3 atoms. This description is typically encompassed in so called force fields. These are sets of parameters for these parameters optimized to reproduce a specific set of properties. For example the SPC/E water model specifies these parameters to reproduce typical water properties at ambient conditions, for example density, pressure and temperature. Specifically, the SPC/E water model specifies σ, ϵ and q parameters per atom type i, k_b and r_{b0} for the OH bond and k_θ and θ_0 for the HOH angle. Non-bonded ij pair interactions are resolved using combination rules. While the use of combination rules is not universal and some force fields describe non-bonded ij interactions explicitly, they are used in a lot of force fields. The most common combination rules are the Lorentz-Berthelot and geometric combination rules

$$\text{Lorentz-Berthelot:} \begin{cases} \sigma_{ij} &= \frac{\sigma_i + \sigma_j}{2} \\ \epsilon_{ij} &= \sqrt{\epsilon_i \epsilon_j} \end{cases} \tag{1.7}$$

$$\text{Geometric:} \begin{cases} \sigma_{ij} &= \sqrt{\sigma_i \sigma_j} \\ \epsilon_{ij} &= \sqrt{\epsilon_i \epsilon_j}. \end{cases} \tag{1.8}$$

More details on the force fields used throughout this dissertation will be disclosed in the individual chapters.

Finally, for computational efficiency, simulations only model a limited number of particles to represent an infinite system. This is achieved by using so-called periodic boundary conditions. In essence this means that a primary simulation cell as shown in 2D in Fig. 1.6, is surrounded by identical replicas. Any motion that occurs in the primary cell, will thus also occur in the replicas. Leading to the fact that when a particle leaves the primary cell on one edge, it re-enters on the opposing edge as shown for the magenta particle in Fig. 1.6. Additionally, since calculating inter-particle interactions with an infinite number of replicas would be computational madness, the minimum image convention is applied. In other words, for every interaction between 2 particles, only the nearest replica is considered. This is shown in Fig. 1.6 between the full magenta and green particles by a green tick and a red cross. The tick signaling the distance used computationally, and the cross signaling the distance that is discarded.

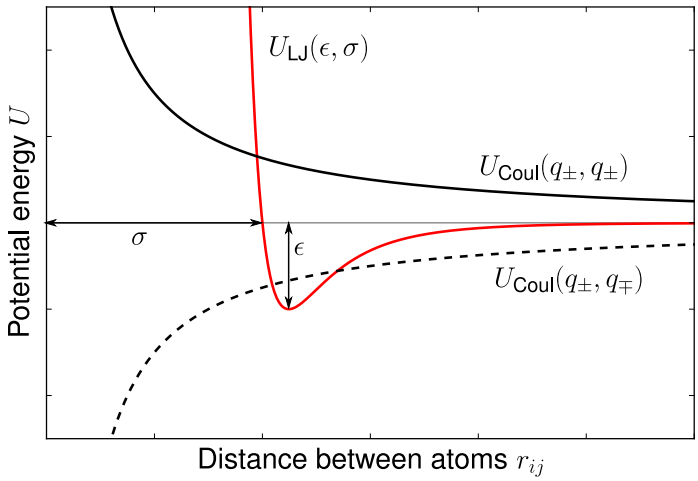

Figure 1.5: Typical non-bonded interactions in Molecular Dynamics simulations. In red are the Lennard-Jones interactions. In black the Coulomb interactions, continuous line for Coulomb interactions between equally charged particles and dashed line for Coulomb interactions between differently charged particles.

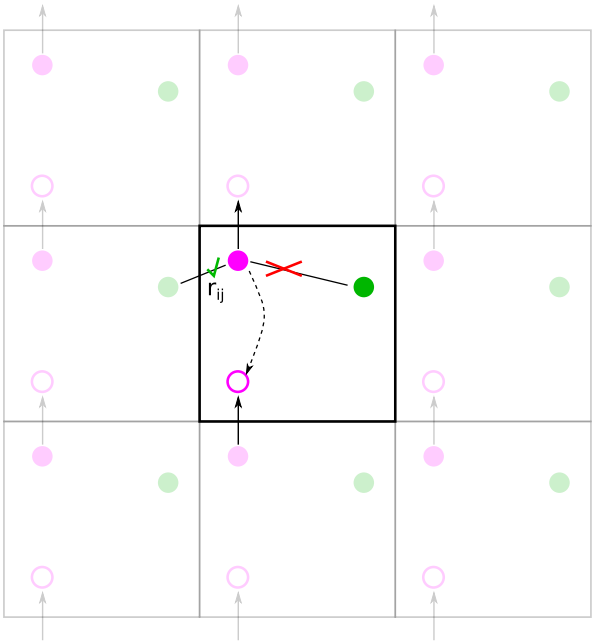

Figure 1.6: Schematic to display the workings of periodic boundary conditions.

1

Thus far, the presented framework would only allow simulations in the micro-canonical or NVE ensemble. Meaning the number of particles N, volume V and total energy E of the system are conserved. When reproducing real experimental conditions however, these are not always the most favored and representative conditions. In such cases conserving and/or controlling the temperature and/or pressure is preferred. This is achieved by for example scaling the velocities to control the temperature yielding the canonical or NVT ensemble, and/or the particle positions and simulation volume to control the pressure yielding the isothermal-isobaric or NPT ensemble. Note that other ensembles exist, but these are not relevant for the present dissertation.

In the NVT ensemble the number of particles N, volume V and temperature T of the system are conserved. In its most basic form, the velocities $\mathbf{u}_i$ are scaled by

$$\gamma = \sqrt{T_0/T} \tag{1.9}$$

where T_0 is the target temperature, set by the user, and T is the current temperature determined from the particle vibrations following

$$T = \frac{1}{nk_B N} \sum_N m_i \mathbf{u}_i^2, \tag{1.10}$$

with k_B being the Boltzmann constant and n indicating the dimensionality (1D, 2D or 3D) [9]. This direct scaling however, leads to unrealistic fluctuations, i.e. instantaneous scaling of the velocity to the right temperature, such that the Nosé-Hoover thermostat is typically preferred. Rather than scaling the velocities directly and instantaneously, in the Nosé-Hoover thermostat [10] the velocities are scaled slowly by including the coupling factor γ

$$\frac{d\gamma}{dt} = \sum_N m_i \mathbf{u}_i^2 - (nN+1)k_B T_0, \tag{1.11}$$

into the equations of motion

$$\frac{d\mathbf{r}_i}{dt} = \mathbf{u}_i, \tag{1.12}$$

$$\frac{d\mathbf{u}_i}{dt} = \frac{\mathbf{F}_i}{m_i} - \frac{\gamma}{Q_T}\mathbf{u}_i. \tag{1.13}$$

Here, Q_T is an effective coupling mass that determines the intensity of the oscillations (scales with $dk_B T$).

The most common approach to control the pressure (ideal gas or kinetic contribution plus internal forces between atoms)

$$p = \frac{Nk_B T}{V} + \frac{1}{nV}\langle \sum r_{ij}\mathbf{F}_{ij} \rangle, \tag{1.14}$$

is via a Nosé-Hoover style barostat [10]. This method is quite similar to the Nosé-Hoover thermostat, by introducing a coupling parameter α to the equations of motion

(5.4) to scale the particle positions, velocities and box size, resulting in

$$\frac{d\mathbf{r}_i}{dt} = \mathbf{u}_i + \frac{\alpha}{Q_p}\alpha\mathbf{r}_i, \tag{1.15}$$

$$\frac{d\mathbf{u}_i}{dt} = \frac{\mathbf{F}_i}{m_i} - \frac{\alpha}{Q_p}\mathbf{u}_i, \tag{1.16}$$

$$\frac{dV}{dt} = nV\frac{\alpha}{Q_p}. \tag{1.17}$$

with

$$\frac{d\alpha}{dt} = nV(p - p_0) \tag{1.18}$$

$$\tag{1.19}$$

and Q_p being an effective coupling mass that determines the oscillation intensity (scales with nNk_BT), p is the current pressure and p_0 is the desired pressure.

When combining the Nosé-Hoover thermostat and barostat, the following equations are obtained:

$$\frac{d\mathbf{r}_i}{dt} = \mathbf{u}_i + \frac{\alpha}{Q_p}\mathbf{r}_i, \tag{1.20}$$

$$\frac{d\mathbf{u}_i}{dt} = \frac{\mathbf{F}_i}{m_i} - \frac{\alpha}{Q_p}\mathbf{u}_i - \frac{\gamma}{Q_T}\mathbf{u}_i, \tag{1.21}$$

$$\frac{dV}{dt} = nV\frac{\alpha}{Q_p}. \tag{1.22}$$

with

$$\frac{d\alpha}{dt} = nV(p - p_0) - \frac{\alpha\gamma}{Q_T}, \tag{1.23}$$

$$\frac{d\gamma}{dt} = \sum_N m_i\mathbf{u}_i^2 - (nN + 1)k_BT_0 + \frac{\alpha^2}{Q_p}. \tag{1.24}$$

The toolbox to carry out relevant MD simulations is now complete, and the work as carried out in this dissertation can begin.

1.3. Outline

In this dissertiation, the limitations and possibilities of modeling interfaces within a MD framework are discussed. Particularly, the effects of surface roughness are highlighted, a novel framework to validate electrokinetic properties is presented, and a method to account for surface reactions is developed. As a case study a silica-electrolyte interface is selected due to its omnipresence in nature and relevance in many scientific fields such as colloid and materials science, phase separation and catalysis, and electrochemistry and energy harvesting. Yet, the observed

phenomenology and newly developed approaches presented here are more broadly applicable.

Before investigating the interface itself, in Ch. 2, MD simulations of electrolytes are performed and assessed [11]. The most common rigid water models (SPC/E [12, 13], TIP3P [14], TIP4P/Ew [15] and TIP4P/2005 [16]) are combined with the many different ion parameters available in literature (Smith and Dang [17], Joung and Cheatham [18], Mamatkulov *et al.* [19], Li *et al.* [20], Benavides *et al.* [21], Zeron *et al.* [22]), and the validity of a mix-and-match approach that has become the norm when combining water and ion force fields is investigated. The metrics used include the ion solvation free energy, the ion-oxygen (water) distance, the ion self-diffusivity, ion-pairing, density variations and the mean ionic activity coefficient. The solvation free energy and ion-oxygen distance are standard metrics used when deriving ion force fields, while the effects at finite concentrations, such as ion pairing, density variations and mean ionic activity coefficients are often ignored. In fact only in the development of 2 out of the 6 ion force fields mentioned above, finite concentration effects were considered. These 2 force fields, also perform best on these metrics. They underperformed however in terms of solvation free energy. In conclusion, it is shown that while in some instances the mix-and-match approach is justified, in other instances fluid properties vary widely depending on the force fields that are combined.

Having carefully analysed combinations of water and ion force fields, in Ch. 3, the interplay between an amorphous silica surface and an electrolyte is studied [23]. First, amorphous silica is formed starting from a β-cristobalite using the annealing and quenching technique [24]. Second, a surface is generated by performing a cut through the amorphous silica and functionalizing the surface groups. In other words, the single bonded oxygens are protonated, and the silanol (SiOH) density is adjusted based on experimental results. Third, the surface is put in contact with an electrolyte mixture containing NaCl-$CaCl_2$, and the surface charge is set in accordance with the concentration and pH by deprotonating silanols to form SiO^- groups [25]. Fourth, MD simulations are performed in which the interface is investigated, with focus on the differences between Na^+ and Ca^{2+} adsorption. It is found that the surface roughness resulting from the cut, directly influences the specific ion adsorption. In particular, Na^+ ions are capable of penetrating deeper into the surface, owing to their smaller hydration shell compared to Ca^{2+} ions. As a result, some surface sites present preferential adsorption of Na^+, whereas the adsorption of Ca^{2+} ions would be expected from theoretical calculations owing to their greater coulombic charge. It is thus hypothesized, that the surface roughness can pose steric hindrances that favor ions based on their hydration properties (size, coordination-number and energy). Unfortunately, experimental data to validate this finding was not available.

In an attempt to bridge the gap between simulation and experimental results, in Ch. 4, an approach is proposed to optimize simulations to experimental results, while at the same time minimizing errors arising in both, experimental and computational set-ups [26]. The concept is derived from combining electrokinetic theory and the iso-electric point (IEP) (pH at which the ζ-potential is zero). Owing to the linear relationship in the Helmholtz-Smoluchowski theory between measured quantity

and the ζ-potential, it is found that at the IEP, the ζ-potential is zero irregardless of the experimental set-up (electro-osmosis, streaming current, streaming potential, ...) and fluid properties such as viscosity and/or dielectric permittivity [27, 28]. The IEP, thus serves as an ideal comparison point between experiments and simulations while eliminating errors from the experimental set-up and the water force field. However, varying the pH in a simulation and for most interfaces simulating at the IEP is not straightforward. In order to overcome this issue, in an analogy to the IEP, we introduce and define the iso-electric concentration (IEC), as the concentration at which the ζ-potential is zero (for a fixed pH). We then optimize the interaction parameters between ion and surface atoms, successfully reproducing the experimentally found IEC for a $CaCl_2$ electrolyte in a silica nanochannel. It is found that the determining factor to reproduce the IEC successfully is finding the right distribution between specifically and non-specifically adsorbed ions.

Having proposed a method to optimize simulations to reproduce more accurately the interfacial behavior, a method to include surface reactions at the interface is developed. In particular, a numerical scheme is designed and presented in Ch. 5 to include protolysis reactions in classical MD simulations at no additional computational cost [29]. Protolysis reactions are selected due to their relevance on most oxide surfaces [30, 31], but the method developed here is no way limited to protolysis reactions, and may easily be adapted to include any other type of surface reactions. Importantly, our approach differs from reactive MD simulations as it does not require the explicit definition of bond breaking and bond making. Instead, the hydrogen atom interactions of SiO^-/SiOH groups are turned on/off at a user defined rate, while adjusting the oxygen parameters accordingly. Setting the reaction rate to values found in literature [32, 33], we were then able to demonstrate that reactions have a non-negligible effect on ion adsorption and dynamics at the interface. Particularly, ion adsorption shifted from specific adsorption to non-specific adsorption, ion diffusion coefficients near the surface increased, and ion adsorption residence times decreased. This newly developed method, thus provides an important step for future developments, by on the one hand showcasing the importance of surface reactions on interfacial fluid phenomena, and on the other hand serving as a manual to include surface reactions in a computational cost effective manner, thus potentially leading to new scientific discoveries and/or products and product improvements.

Finally, concluding remarks to this dissertation are provided in Ch. 6.

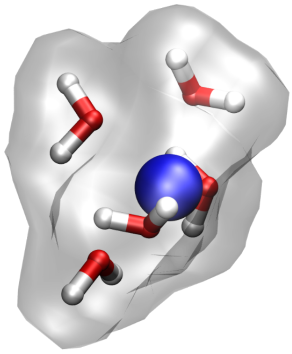

2

Transferability of Ion Parameters in Molecular Simulations

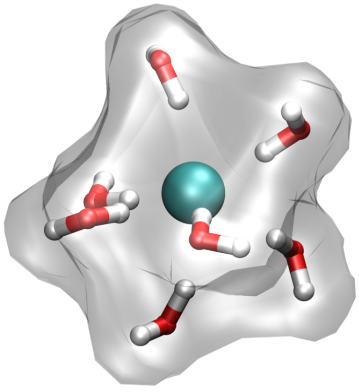

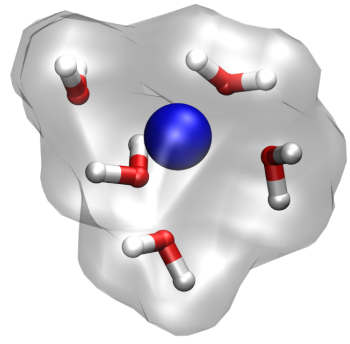

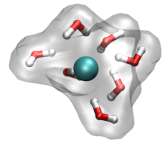

This chapter is based on the paper:

M. F. Döpke, O. A. Moultos and R. Hartkamp, *On the transferability of ion parameters to the TIP4P/2005 water model using molecular dynamics simulations*, J. Chem. Phys, **152**, 024501 (2020).

2.1. Introduction

Aqueous electrolyte solutions have been studied extensively using Molecular Dynamics (MD), for applications ranging from water desalination to osmotic power harvesting [34–36]. These simulations rely strongly on the selection of force field parameters. To simulate an aqueous electrolyte, one needs a force field to describe the interactions between water molecules, at least one to describe the interactions between ions, and a combination rule or parameters to describe interactions between water and ions. In principle, any set of water and ion parameters could be combined, but this is not guaranteed to produce physically meaningful results. Ion parameters are optimized in combination with a specific water model and for certain physical properties, which are not necessarily conserved with a different water model. The focus in this chapter, is on the transferability of ion parameters between water models, leaving the combination rules aside. However, the reader should be aware that many shortcomings in ionic systems have also been attributed to combination rules [37, 38]. A variety of force fields optimized to reproduce different properties of water exist. These water models range from polarizable to rigid force fields, each with their own benefits and disadvantages. Our focus will be on rigid water force fields, since these are most commonly used to represent water in aqueous electrolyte solutions.

Some of the most common rigid water force fields are the SPC/E [12, 13], TIP3P [14], TIP4P/Ew [15] and TIP4P/2005 [16] water models. The TIP4P/2005 model has emerged as one of the best all-around models [16, 39, 40]. Despite this, many of the widely used ion parameters are optimized with TIP3P or TIP4P/Ew, since these water models are used in the AMBER [41] and CHARMM [42] force fields. Even when ion parameters optimized in combination with TIP4P/2005 are available, ions optimized with other water models might represent some physical properties more accurately, depending also on the optimization criteria of the parameter set. As a result, many studies [23, 43–64] used ion parameters optimized for other water models in combination with TIP4P/2005, hoping to leverage the strengths of both the ion and water parameter sets.

One of the first studies combining ions and the TIP4P/2005 water model was performed by Alejandre *et al.* [43]. In this study, crystal formation in water was studied using 8 NaCl force field models combined with SPC/E, SPC/Fw [65], TIP4P/2005 and SPC/Fh [43] water models. Despite not using ion parameters optimized for TIP4P/2005, it was found that cluster formation was best predicted by the TIP4P/2005 water model and by a water model introduced in the same study (SPC/Fh). Two years later, Pérez and Rubio [46] studied droplet nucleation of a supersaturated vapor using the TIP4P/2005 water model combined with OPLS [66] ion parameters. While transferability to TIP4P/2005 water was not directly studied, the authors noted that the ion parameters would require reparametrization. Shortly after, Moučka *et al.* [47] used the Joung and Cheatham (JC) [18] TIP4P/Ew-optimized ion parameters combined with TIP4P/2005. The choice was justified by finding good agreement of the predicted and experimental chemical potential of NaCl. In the following years, a variety of studies have followed suit, combining the JC TIP4P/Ew-optimized ion parameters or other ion parameters with the TIP4P/2005 water model [23, 48–64].

Following the increased use of TIP4P/2005 and demand of ion parameters specif-

ically optimized for TIP4P/2005, the Vega group started working on obtaining parameters for NaCl in terms of solubility [67, 68]. The final parameters are presented in [21]. Recently, additional ion parameters were published for Li^+, Na^+, K^+, Mg^{2+}, Ca^{2+}, Cl^- and SO_4^{2-} [22]. However, their performance considering hydration free energies, relies on a scaling parameter in order to account for the reduced charges as will be shown in Sec. 2.4. Furthermore, modeling of many applications such as waste water treatment, nuclear waste disposal, or heavy metal removal, require modeling of for example RbCl, $SrCl_2$ or $LaCl_3$. Higher valency ions remain rare in literature, and also cannot be combined easily with the Benavides *et al.* [21] and/or Zeron *et al.* [22] ions due to the use of $\pm 0.85e$ and $\pm 1.7e$ as partial charges for monovalent and divalent ions, respectively. This choice of partial charges, known as Electronic Charge Correction (ECC), was argued to be necessary in a non-polarizable model to account for the electronic contribution to the dielectric constant [69, 70]. ECC has received increased attention in recent years [52, 57, 71–73], but remains unusual for most ion force fields.

Because of the large body of studies combining various ion parameters with the TIP4P/2005 water model, we aim at providing a comprehensive transferability study of the most commonly used ion parameters in combination with TIP4P/2005 water in terms of solvation properties. The here presented results can thus serve as a baseline for safely combining ion parameters with the TIP4P/2005 water model in cases where no suitable ion parameters are available. It will be shown that in some situations, even though parameters optimized combined with TIP4P/2005 are available, mixing force fields may yield better performance in terms of specific properties of interest.

We focus on the Hydration Free Energy (HFE or ΔG_{solv}), Ion-Oxygen Distance (r_{IO}) and Coordination Number (CN) of the first hydration shell, ion self-diffusion coefficient ($D_{i,\text{self}}$), chemical potential (μ), and mean ionic activity coefficients (γ), of which ΔG_{solv} and r_{IO} are commonly fitted in the parametrization procedure of ions in water. For many parametrization studies, ΔG_{solv} is used as the first step in the optimization, with r_{IO} generally being provided as an independent check of quality and validity of the parameters [17–20, 66, 74–76]. For example, Smith and Dang [17] optimized Na^+ and Cl^- ions for SPC/E water by fitting to experimental gas-phase binding energies for small ion-water clusters and to solvation energies, ΔG_{solv}, of ionic solutions. The r_{IO} was provided as an independent check to match the experimental data. The parameters of Smith and Dang [17] have been used frequently, and the corresponding ion properties have been evaluated in combination with a multitude of water models, from the prediction of mean ionic activity coefficients to thermodynamic transport properties [77–79]. Joung and Cheatham [18] performed a thorough optimization by first mapping ΔG_{solv} for a range of Lennard-Jones (LJ) length σ and energy ϵ parameters, assuming a unitary partial charge. Second, they computed the lattice constant and energy of salt crystals by varying σ across the LJ parameter space, while keeping ΔG_{solv} constant. Finally, quantum mechanical simulations were used to tune r_{IO} of various ion-water structures. Mamatkulov and coworkers [19, 76] followed a similar strategy for divalent cations, first mapping ΔG_{solv} for a σ-ϵ parameter space, but as a second step they fitted the mean ionic activity coefficients using Kirkwood-Buff theory. The radii of first hydration shell were computed with the

final parameters and shown to be in good agreement with experimental results. The JC and Mamatkulov ions have gained popularity in MD studies and many properties have also been investigated for these ions [53, 67, 68, 77]. Trivalent and quadrivalent cations were parametrized by Li *et al.* [20], who fitted ion parameters to experimental ΔG_{solv} and r_{IO} values. However, for these highly charged ions, it was found that the standard 12-6 LJ potential (see Eq. (1.6)) could not simultaneously reproduce both properties accurately. Therefore, a 12-6-4 LJ potential was introduced, with which both ΔG_{solv} and r_{IO} could be reproduced reasonably well. Because this 12-6-4 LJ potential is not implemented in common MD packages, Nikitin and Del Frate [73] recently optimized monovalent and multivalent ion parameters using the standard 12-6 LJ potential and ECC. However, these ions were optimized in combination with the TIP3P water model and were shown to be poorly transferable to the TIP4P/Ew water model. Finally, Benavides *et al.* [21] and very recently Zeron *et al.* [22] produced the only ion parameters known to us specifically optimized for the TIP4P/2005 water model. Benavides *et al.* [21] adjusted Na^+ and Cl^- LJ parameters and charges to reproduce electrolyte properties at finite concentrations, such as the solubility and mean ionic activity coefficients, whereas Zeron *et al.* [22] optimized Li^+, Na^+, K^+, Mg^{2+}, Ca^{2+}, Cl^- and SO_4^{2-} parameters in terms of solution densities and structural properties at multiple finite ion concentrations.

In this work, we took ion parameters from Smith and Dang [17], Joung and Cheatham [18], Mamatkulov *et al.* [19], Li *et al.* [20], Benavides *et al.* [21] and Zeron *et al.* [22], and calculated the ΔG_{solv}, r_{IO}, CN and $D_{i,\text{self}}$ at infinite dilution (no ion-ion interactions are considered) and standard atmospheric conditions combined with the TIP4P/2005 water model. We also computed the density, ion pairing, chemical potential and mean ionic activity coefficients for selected ion parameters to assess their performance at finite concentrations. These properties are often neglected during parameter optimization. An exception to this are the studies of Benavides *et al.* [21] and Zeron *et al.* [22], which considered these properties during their parameter optimization, obtaining good agreement with experiments. We verified our simulation approach by reproducing the results obtained from these ion parameters with the water model that they were originally optimized for. Additionally, some of the properties calculated here, such as the CN and $D_{i,\text{self}}$, have not been published previously for many ion parameters. As such, our results provide an extensive overview and analysis that will assist in the selection of ion parameters for the TIP4P/2005 water model by providing a clear overview of their performance and transferability. It will be shown that TIP4P/Ew optimized ion parameters can be used safely combined with the TIP4P/2005 water model, benefiting from the ability of TIP4P/2005 to accurately represent water properties.

The remainder of this chapter is organized as follows: The methodology is described in Sec. 2.2 and its implementation verified in Sec. 2.3. The results are presented in Sec. 2.4, and the conclusions provided in Sec. 2.5.

2.2. Methods

The systems simulated can be divided into two types: 1) infinite dilution systems with a single solvated ion, and 2) finite concentration systems with a finite number of ion pairs.

In the infinite dilution systems, a single ion was placed in a cubic periodic box containing 523 water molecules, whereas in the finite concentration systems between 1 and 60 ion pairs were placed in a cubic periodic box containing either 555 or 1,110 water molecules (0.05, 0.1, 0.5, 1, 2, 4 and 6 mol/kg). Each system was energy minimized using the conjugate gradient method, followed by an initialization phase in the NPT ensemble at 1 atm and 298 K to eliminate overlaps between molecules. During the initialization, the time step was increased in consecutive runs of 10,000 steps from $dt = 0.001$ fs to 0.01, 0.1, 0.2, 0.5, until reaching a time step of 1 fs, which was used in all subsequent simulations. The systems were then equilibrated in the NPT ensemble, for 100 ps in the case of infinite dilution systems, and 500 ps in the case of finite concentration systems.

Two types of production simulations were performed: 1) Thermodynamic Integration cycle from which the ΔG_{solv} was obtained, and 2) a bulk simulation from which the density, ion pairing, Radial Distribution Functions (rdf) and the $D_{i,\text{self}}$ were obtained.

All simulations were performed with the LAMMPS simulation package [80] using the Nosé-Hoover thermostat and barostat where appropriate, with coupling constants of 100 dt and 1000 dt, respectively [81, 82]. A cut off of 10 Å was used for LJ and Coulombic interactions, and long range electrostatic interactions were computed with the particle-particle particle-mesh (pppm) method with a relative precision of 10^{-6}. In all simulations the Lorentz-Berthelot mixing rule was used (see Eq. (1.7)), except for the simulations including the Benavides *et al.* [21] or Zeron *et al.* [22] ions, for which cross-species interactions were given explicitly.

2.2.1. Hydration Free Energy

The HFE was obtained using a two-stage thermodynamic integration method [83]. In the first stage (*annihilation*), the charge of the ion was slowly neutralized in water, followed by the second stage (*decoupling*) in which the van der Waals interactions were slowly removed. For the *annihilation* phase 6 integration windows from 1 to 0 with equal spacing were used, and for the *decoupling* phase unequal spacing with $\lambda_i = 1.0, 0.8, 0.6, 0.5, 0.4, 0.35, 0.3, 0.25, 0.2, 0.15, 0.1, 0.05, 0.0$ was used. This number and spacing of integration windows was found to be sufficient for accurate results as shown in Fig. 2.1, which shows that identical results for ΔG_{solv} are obtained for the *annihilation* with 12 and 6 λ_i states, and for the *decoupling* with 26 and 13 λ_i states. Each integration window was equilibrated for 100 ps, followed by 500 ps production run in the NPT ensemble. Furthermore, for the *decoupling* phase a soft

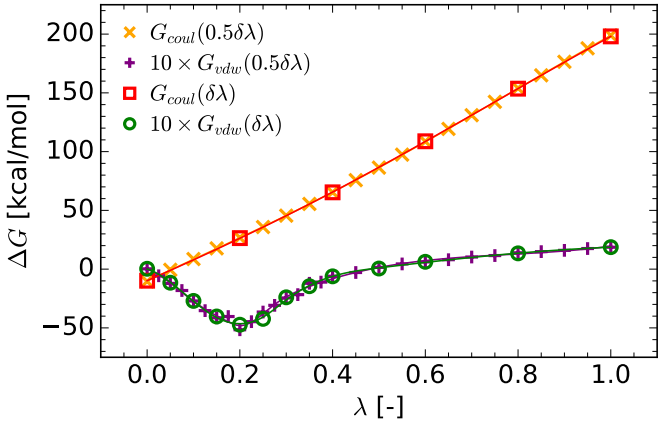

Figure 2.1: Change in solvation free energy ΔG_{solv} at the respective lambda states λ.

core potential (U being the potential energy) of the form

$$U = \lambda^n 4\epsilon \left\{ \frac{1}{\left[\alpha_{\text{LJ}} (1-\lambda)^2 + \left(\frac{r}{\sigma}\right)^6\right]^2} - \frac{1}{\alpha_{\text{LJ}} (1-\lambda)^2 + \left(\frac{r}{\sigma}\right)^6} \right\}, \tag{2.1}$$

was used to avoid singularities [84]. ϵ and σ have the usual LJ potential meanings and r represents the distance between two particles. $n = 1$ and $\alpha_{\text{LJ}} = 0.5$ are fitting constants chosen to produce the smallest variance in the results [85–88].

For each integration window, $\langle \partial U/\partial\lambda \rangle_{\lambda_i}$ was calculated using the perturbation method

$$\frac{\partial U(\lambda_i)}{\partial \lambda} = \left\langle \frac{U(\lambda_i + \delta) - U(\lambda_i)}{\delta} \right\rangle_{\lambda_i}, \tag{2.2}$$

with a perturbation of $\delta = 0.002$ [89]. This method calculates the Gibbs free energy at λ_i and $\lambda_i + \delta$ without changing the particle positions. The obtained λ_i states were fitted with a cubic spline and finally ΔG_{solv} was obtained integrating over the spline. Path independence was verified by reversing the *annihilation* and *decoupling* phases to go from $\lambda = 0$ to $\lambda = 1$.

Some studies [19, 75, 90] have suggested that ΔG_{solv} needs to be corrected by accounting for various effects such as finite size effects

$$\Delta G_{\text{fs}} = -z^2 \frac{\text{N}_\text{A} e^2}{4\pi\varepsilon_0} \frac{1}{2L} \left[\frac{\xi_{\text{Ew}}}{\varepsilon_r} + \left(1 - \frac{1}{\varepsilon_r}\right) \left(\frac{4\pi}{3} \left(\frac{r_{\text{IO}}}{L}\right)^2 - \frac{16\pi^2}{45} \left(\frac{r_{\text{IO}}}{L}\right)^5 \right) \right], \tag{2.3}$$

the hypothetical transfer of ions from ideal gas to ideal solution

$$\Delta G_{\text{press}} = \text{N}_\text{A} k_B T \ln p_1/p_0 = 1.9 \text{ kcal/mol}, \tag{2.4}$$

and/or the surface potential at the air-water interface

$$\Delta G_{\text{surf}} = -\nu_i \times 12.1415 \text{ kcal/mol}. \tag{2.5}$$

Here ν_i is the ion valency of ion i, N_A is the Avogadros constant, k_B the Boltzmann constant, T the temperature, p the pressure, e the electron charge, ε_0 the dielectric permitivity of vacuum, ε_r the dielectric permitivity of the water model used, $\xi_{\text{Ew}} = 2.837297$ the Wigner constant, L the box side length, and r_{IO} the Ion-Oxygen Distance. However, to maintain consistency between all literature results and our results, the transfer of ions from ideal gas to ideal solution and the surface potential at the air-water interface, were not considered in the present study. Additionally, in simulation boxes with 66, 523 and 4,179 SPC/E water molecules (12.5, 25 and 50 Å box side lengths) and a single Smith and Dang [17] Na^+ ion, we have shown the finite size effect to be negligible. Without finite size-corrections hydration energies of 88.3, 87.5 and 87.5 kcal/mol were obtained, whereas with the correction 90.8, 88 and 87.7 kcal/mol were obtained, respectively.

Finally, results obtained with force fields that use ECC, need to be corrected following [69, 70]

$$\Delta G_{\text{solv}} = \Delta G_{\text{MD}} + \Delta G_{\text{el}} \tag{2.6}$$

where ΔG_{MD} is obtained from the MD simulations and ΔG_{el} is given by

$$\Delta G_{\text{el}} = \frac{q^2}{2R}\left(1 - \frac{1}{\epsilon_{\text{el}}}\right), \tag{2.7}$$

with R representing the spherical cavity radius of the first hydration shell. Assuming a continuum solvent, ΔG_{MD} can furthermore be rewritten to

$$\Delta G_{\text{MD}} = \frac{q^2}{2R\epsilon_{\text{el}}}\left(1 - \frac{1}{\epsilon_{\text{MD}}}\right), \tag{2.8}$$

which when combined with Eq. (2.7) yields

$$\Delta G_{\text{el}} = \Delta G_{\text{MD}}\left[\frac{\epsilon_{\text{el}}}{1 - \frac{1}{\epsilon_{\text{MD}}}}\left(1 - \frac{1}{\epsilon_{\text{el}}}\right)\right]. \tag{2.9}$$

In the limit of $\epsilon_{\text{MD}} >> 1$, Eq. (2.9) can further be simplified to

$$\Delta G_{\text{el}} = \Delta G_{\text{MD}}\left[\frac{\epsilon_{\text{el}}}{1 - 0}\left(1 - \frac{1}{\epsilon_{\text{el}}}\right)\right] = \Delta G_{\text{MD}}\left(\epsilon_{\text{el}} - 1\right). \tag{2.10}$$

Inserting Eq. (2.10) into Eq. (2.6), then yields

$$\Delta G_{\text{solv}} = \Delta G_{\text{MD}} + \Delta G_{\text{MD}}\left(\epsilon_{\text{el}} - 1\right) = \Delta G_{\text{MD}}\epsilon_{\text{el}}, \tag{2.11}$$

with ϵ_{el} being the scaling factor $\epsilon_{\text{el}} = q^2/q_{\text{ECC}}^2$ such that $\Delta G_{\text{solv}} = \Delta G_{\text{solv,ECC}} q^2/q_{\text{ECC}}^2$.

Uncertainty quantification was performed for a single Joung and Cheatham [18] SPC/E optimized Na^+ ion in SPC/E water using 5 independent simulations with different starting conditions. HFE values were found to be almost identical for the independent simulations ($\Delta G = (89.1, 89.1, 89.1, 89.0, 89.0)$). Therefore, we did not run independent simulations for other ion-water combinations for computational efficiency.

2.2.2. Ion-Oxygen Distance and Coordination Number

The r_{IO} and CN were obtained from 4 independent 2 ns simulations with a single solvated ion in the NVT ensemble. The simulations were started as described previously, followed by 100 ps equilibration before every production run.

The RDF given by the fraction of local density $\rho(r)$ over global density ρ

$$g(r) = \frac{\rho(r)}{\rho} \tag{2.12}$$

was sampled every 1 fs up to a distance of 10 Å with 2000 bins. The radii of first hydration shell, r_{IO}, were obtained by identifying the location of the first peak of the RDF. The CN of the first hydration shell was computed by integrating over the RDF up to the first minimum following that peak.

Finite size independence of the RDF was verified for simulations with 66, 523 and 4,179 SPC/E water molecules (12.5, 25 and 50 Å box side lengths) and a single Smith and Dang [17] Na^+ ion. The obtained r_{IO} and CN were respectively: 2.36, 2.37 and 2.36 Å, and 5.7, 5.7 and 5.8.

2.2.3. Self-Diffusion Coefficient

The self-diffusion coefficient was obtained from 4 independent simulations with a single solvated ion. The simulations were started as described previously, followed by 100 ps equilibration and 2 ns production runs in the NVT ensemble. During the production runs the Mean Squared Displacement (MSD= $\left(r_{j,i}(t) - r_{j,i}(0)\right)^2$) was sampled, from which the self-diffusion coefficient was obtained following

$$D_{i,\text{sim}} = \lim_{t\to\infty} \frac{1}{6tN_i} \left\langle \sum_{j=1}^{N_i} \left(r_{j,i}(t) - r_{j,i}(0)\right)^2 \right\rangle, \tag{2.13}$$

where t indicates the time, N_i the number of atoms of species i and $r_{j,i}$ the position of the j-th atom of species i [91]. The MSD was sampled every 1 ps using the OCTP LAMMPS plugin from Jamali *et al.* [92], which calculates the MSD on the fly using the order$-n$ algorithm [93]. The self-diffusion coefficient then follows from the linear regime in a loglog plot as shown in Fig. 2.2 and Eq. (2.13).

For the diffusion coefficient, a finite-size correction was found to be necessary. For simulation boxes with 66, 523 and 4,179 SPC/E water molecules (12.5, 25 and 50 Å box side lengths) and a single Smith and Dang Na^+ ion, diffusion coefficients of 0.9, 1.1 and 1.4 $\times 10^{-9}$ m^2/s were obtained without finite-size correction and 1.6, 1.5 and 1.6 $\times 10^{-9}$ m^2/s with finite size correction. In order to account for the finite size effects, the correction of Yeh and Hummer [94]

$$D_{i,\text{self}} = D_{i,\text{sim}} + \frac{\xi k_B T}{6\pi\eta L}, \tag{2.14}$$

is applied, where η stands for the viscosity.

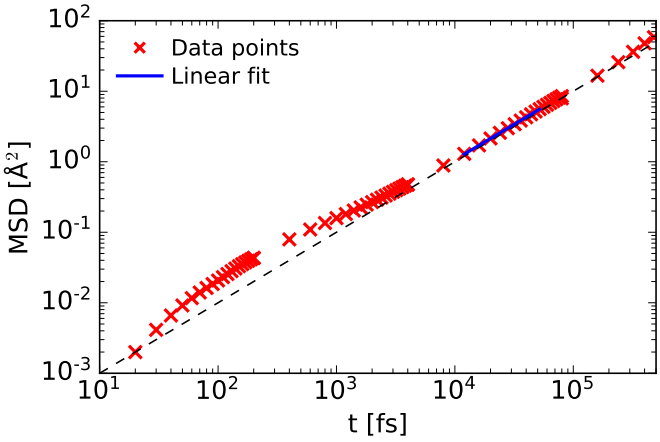

Figure 2.2: MSD obtained for a single SD Na^+ ion in TIP4P/2005 water. Ballistic regime is found at at $t < 10$, and linear regime at $t > 10$ ps. Linear regression was done from 10 to 50 ps obtaining the slope. Coefficients of determination for the regression were above 0.999 for all simulations.

2.2.4. Mean Ionic Activity Coefficients

Mean ionic activity coefficients, henceforth referred to as activity coefficients, were obtained from the solvation energies at various molalities following the approach presented by Mester and Panagiotopoulos [78]. In short, the activity coefficient γ as a function of molality m can be expressed in terms of the chemical potential μ as:

$$\begin{aligned}\mu &= \mu^{\dagger} + 2k_B T \ln m + 2k_B T \ln \gamma \\ &= \mu^{\dagger} + 2k_B T \ln m + 2k_B T \ln 10 \left(-\frac{A\sqrt{m}}{1 + B\sqrt{m}} + bm + Cm^2 + Dm^3 \right),\end{aligned} \tag{2.15}$$

where B, b, C and D are fitting parameters, A is given by

$$A = \frac{1.824 \times 10^6}{(\varepsilon_0 \varepsilon_r T)^{3/2}}, \tag{2.16}$$

and $\mu^{\dagger}$ is Henry's law standard chemical potential, which can be obtained combining the Debye-Hückel limiting law activity coefficient

$$\ln \gamma = \frac{\nu_i^2 e^2 k}{8\pi \varepsilon_0 \varepsilon_r k_B T}, \tag{2.17}$$

with the chemical potential obtained from a simulation at low molality ($m = 0.05$ kg/mol in our case). Here k is the inverse of the Debye length

$$k^2 = \frac{2Ie}{\varepsilon_0 \varepsilon_r k_B T}, \tag{2.18}$$

with I being the ionic strength as a function of the molar concentration c_i of species i

$$I = \frac{1}{2}\sum_{i=1}^{n} c_i z_i^2. \tag{2.19}$$

The chemical potential μ can furthermore be split up into the ideal gas contribution μ_{ig} and the contribution from the interactions of the ion pair μ_{ex} as

$$\mu = \mu_{\text{ig}} + \mu_{\text{ex}} \tag{2.20}$$

with

$$\mu_{\text{ig}} = \mu_0^{cation} + \mu_0^{anion} + 2k_B T \ln \frac{k_B T N_{ion-pairs}}{\text{N}_\text{A} P \langle V \rangle} \tag{2.21}$$

and

$$\mu_{\text{ex}} = \Delta G_{\text{solv}} \tag{2.22}$$

The standard chemical potentials μ_0 are obtained from the NIST-JANAF thermochemical tables [95].

The solvation energies ΔG_{solv} of an ion pair at multiple molalities were obtained following the approach described in Sec. 2.2.1 with some modifications. For better resolution, the λ_i steps were increased and spaced uniformly from 0 to 1 in steps of 0.05 for *annihilation* and *decoupling*. Furthermore, each integration window was extended to 300 ps equilibration and 1500 ps production.

2.3. Verification

Our simulation and analysis protocol was verified by reproducing the results from Smith and Dang [17], Benavides *et al.* [21], Joung and Cheatham [18] and Mamatkulov *et al.* [19], as shown in Fig. 2.3. The results from the HFE calculations are shown on the left and for the n_{IO} calculations on the right.

For the SD and Benavides ions, the single ion ΔG_{solv} were combined following $\Delta G^{\text{NaCl}} = \Delta G^{\text{Na}^+} + \Delta G^{\text{Cl}^-}$ to form the ion pair ΔG_{solv} reported in the original papers. It is found that this approach predicts an ion pair ΔG_{solv} below the reported value by 3 % for the SD ions and 8 % for the Benavides ions. The reason for this discrepancy is unknown as no corrections were applied to either results and finite size effects have been shown to be negligible above 500 water molecules. We consider the possibility that the strategy involved to compute the ΔG_{solv} is responsible, as neither Smith and Dang [17] nor Benavides *et al.* [21], used thermodynamic integration. Furthermore, these authors simulated ion pairs, avoiding issues arising from simulations with a charge imbalance. The results of Joung and Cheatham [18] could be reproduced with errors below 1 %. Once we corrected the data from Mamatkulov *et al.* [19] to remove the hypothetical transfer of ions from ideal gas to ideal solution and the surface potential at the air-water interface, their results could also be reproduced with errors below 1 %.

In terms of the n_{IO}, we were able to reproduce the results from Smith and Dang [17] and Benavides *et al.* [21] with errors below 2 %, and for the JC ions [18] the

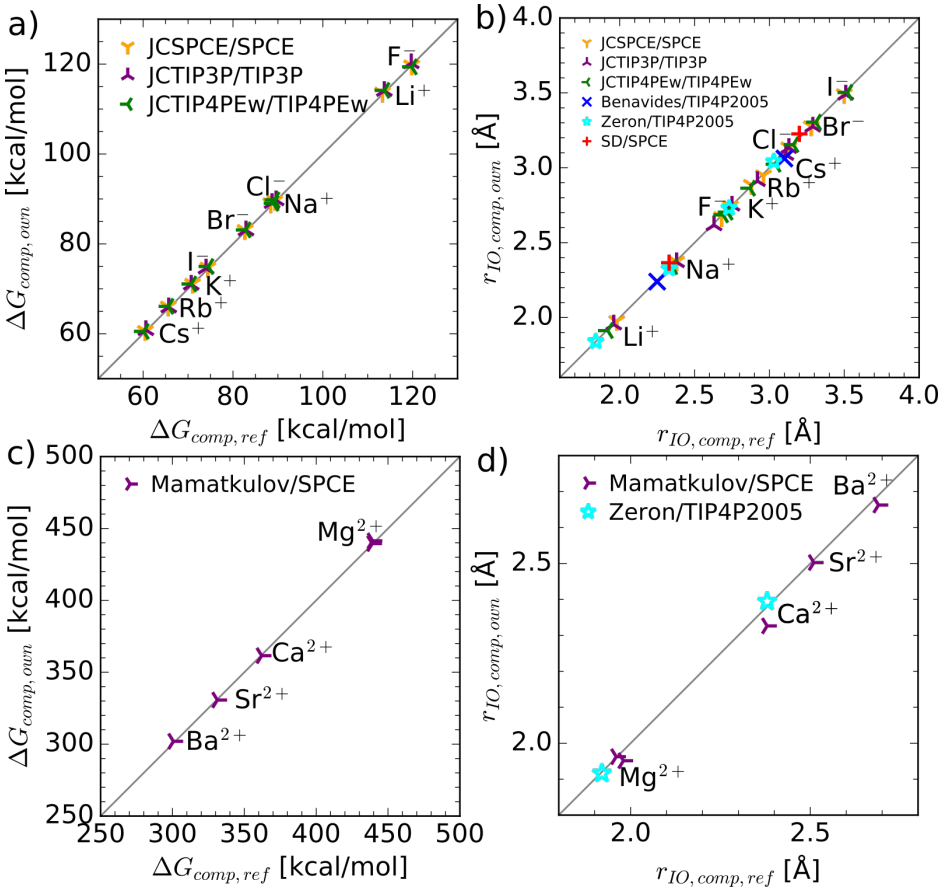

Figure 2.3: Verification of our methodology by reproducing the results from Smith and Dang [17], Benavides *et al.* [21], Joung and Cheatham [18] and Mamatkulov *et al.* [19]. (a) and (c) show the ΔG_{solv} and (b) and (d) the r_{IO}.

differences found were always below 1 %. The Mamatkulov ions [19] showed the largest differences, with errors up to 2 % for Ca^{2+}.

In conclusion, our simulation and analysis procedure is shown to accurately reproduce results from the literature with very limited errors.

2.4. Results

Simulations for a variety of ion parameters [17–22] and water models were performed to test the transferability of ion parameters optimized for SPC/E [12], TIP3P [14] and TIP4P/Ew [15] water models to the TIP4P/2005 [16] water model in terms of the hydration free energy, radius and coordination number of first hydration shell, and self-diffusion coefficient at infinite dilution. The results are displayed throughout Figs. 2.4-2.8, which show ΔG_{solv}, r_{IO}, CN and $D_{i,\text{self}}$ obtained from the simulations

and experimental results where available. The second hydration shell r_{IO} and CN are given in Figs. 2.10-2.14 together with different scalings of the diffusion coefficients. For selected ion parameters also finite concentration properties were evaluated as shown throughout Figs. 2.15 to 2.17. The naming convention of the references henceforth will be as follows: SD for the Smith and Dang [17] ion parameters, JC for the Joung and Cheatham [18] parameters, Mamatkulov for the Mamatkulov *et al.* [19] parameters, Li for the Li *et al.* [20] parameters, Benavides for the Benavides *et al.* [21] parameters and Zeron for the Zeron *et al.* [22] ion parameters. For the trivalent and quadrivalent ions from Li we consider only the parameters derived for the 12-6 LJ potential, with LiHFE referring to the ion parameters optimized for ΔG_{solv} and LiIOD referring to the ion parameters optimized for r_{IO}.

2.4.1. Hydration Free Energy

Monovalent Ions

Figs. 2.4a and 2.5a show ΔG_{solv} of monovalent ions in SPC/E, TIP3P, TIP4PEw and TIP4P/2005 water. We will discuss the results in chronological order of publication, starting with the SD ions, followed by the JC ions and concluding with the Benavides and Zeron ions.

The SD Na^+ and Cl^- ϵ and σ parameters were originally tuned to reproduce the gas-phase binding energy and liquid phase hydration energy of NaCl together with the SPC/E water model [17]. After parametrization, $\Delta G_{\mathrm{solv}} = 182 \pm 3$ kcal/mol was reported, which is close to the experimental value of 188 kcal/mol from Friedman and Krishnan [98]. We attempted to reproduce this result by adding $\Delta G_{\mathrm{solv}}^{\mathrm{Na}^+} + \Delta G_{\mathrm{solv}}^{\mathrm{Cl}^-}$ from two separate infinite dilution simulations, obtaining 175.5 kcal/mol. The discrepancy may arise due to the method used to compute ΔG_{solv}. Smith and Dang [17] calculated the total potential energy of the system, and subtracted the energy of the water molecules, while we used thermodynamic integration for single ions in water. Despite this, 175.5 kcal/mol is actually in better agreement with more recent experimental results [96], which report $\Delta G_{\mathrm{solv}}^{\mathrm{NaCl}} = 177.7$ kcal/mol. The single ion ΔG_{solv} for the SD Na^+ and Cl^- ions are 87.5 and 88.3 kcal/mol when in SPC/E water, and 85.1 and 90.4 kcal/mol when in TIP4P/2005 water, as shown in Figs. 2.4a and 2.5a. These values compare well to the experimental results of Marcus [97] (87.2 and 81.3 kcal/mol) and Schmid *et al.* [96] (88.7 and 89.1 kcal/mol, for Na^+ and Cl^-, respectively). As a result the SD ion parameters display good agreement with experimental results in terms of hydration free energy with both water models, SPC/E and TIP4P/2005.

Joung and Cheatham [18] performed a comprehensive optimization of monovalent ion-parameters for three water models, SPC/E, TIP3P and TIP4P/Ew. For each combination, the JC ion parameters performed well in terms of ΔG_{solv} compared to the experimental results (errors below ± 1 %) provided by Schmid *et al.* [96], as shown in Figs. 2.4a and 2.5a. In terms of transferability to TIP4P/2005, the TIP4P/Ew optimized ion parameters (JCTIP4PEw) perform best, providing nearly identical results between the 2 water models. Differences between using either water model and to the experimental results of Schmid *et al.* [96] were found to be below ± 1 % for all ions. The SPC/E and TIP3P optimized ion parameters (JCSPCE and JCTIP3P) display an increase in ΔG_{solv} prediction for anions and a decrease for cations when

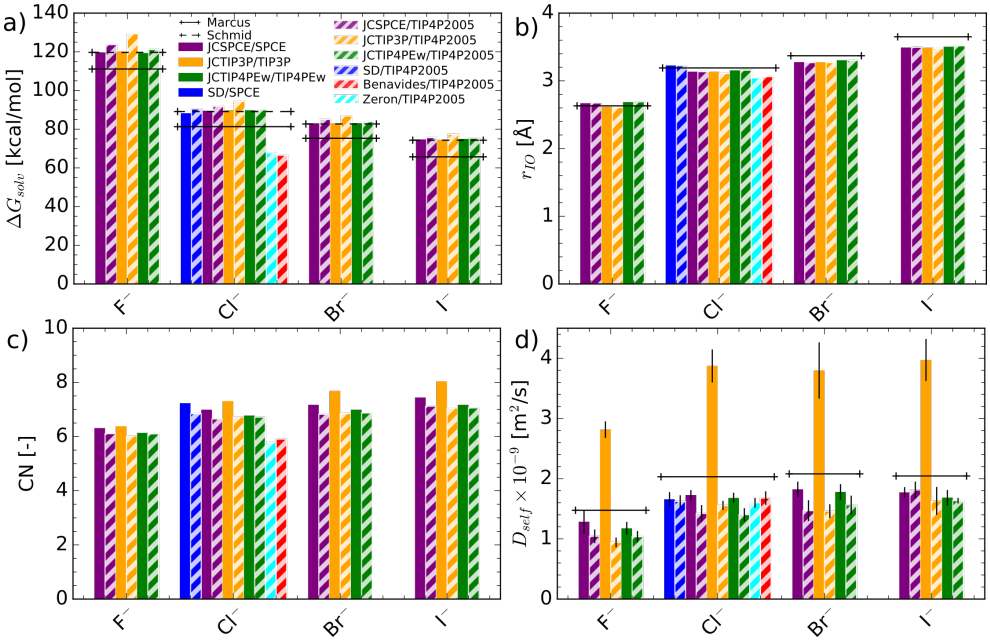

Figure 2.4: Transferability of monovalent anion parameters in terms of ΔG_{solv} (a), r_{IO} (b), CN (c) and $D_{i,\text{self}}$ (d). 95 % uncertainty is shown for $D_{i,\text{self}}$. Other uncertainties were negligible. Experimental results are either from Schmid [96] or Marcus [97].

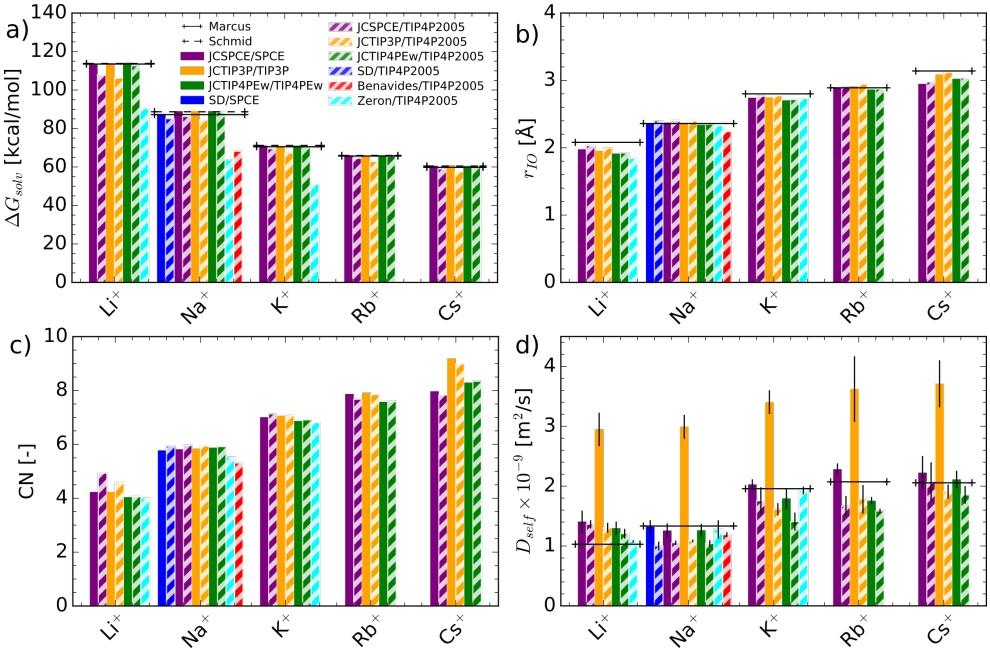

Figure 2.5: Transferability of monovalent cation parameters in terms of ΔG_{solv} (a), r_{IO} (b), CN (c) and $D_{i,\text{self}}$ (d). 95 % uncertainty is shown for $D_{i,\text{self}}$. Other uncertainties were negligible. Experimental results are either from Schmid [96] or Marcus [97].

in TIP4P/2005 water. In TIP4P/2005 water, the SPC/E optimized ions display errors below ± 5 % between predicted and experimental ΔG_{solv}, while for TIP3P optimized ions, errors of up to ± 8 % are obtained. Due to the consistent overprediction of anion ΔG_{solv} and underprediction of cation ΔG_{solv}, the errors in ion pair ΔG_{solv} obtained from the SPC/E and TIP3P optimized ions only range between ± 1 and ± 3 % for SPC/E and TIP3P optimized ions, respectively.

Benavides *et al.* [21] optimized NaCl ion parameters for a number of properties, including solubility and activity coefficients. While this model performs very well over a range of concentrations and temperatures (often not considered in other parametrization studies), ΔG_{solv} is significantly underpredicted as shown in Figs. 2.4a and 2.5a. In the original publication, the hydration energy was not reported, but instead the lattice energy was reported to be considerably underpredicted with 145 kcal/mol, compared to 188.6 kcal/mol obtained in experiments. This underprediction was argued to originate from the charge scaling of the ions from 1 to 0.85. And indeed, scaling ΔG_{solv} by $\epsilon_{\text{el}} = q^2/q^2_{\text{ECC}} = 1/0.85^2$, as was done for the lattice energy in [21], yields $\Delta G^{\text{Na}^+}_{\text{solv}} = 94.4$ kcal/mol, $\Delta G^{\text{Cl}^-}_{\text{solv}} = 92.0$ kcal/mol and $\Delta G^{\text{NaCl}}_{\text{solv}} = 186.4$ kcal/mol, which is close to experimental results [96, 97] (188.6 and 177.7 kcal/mol, respectively). The Zeron ions [22] suffer from the same charge scaling effect as the Benavides ions, underpredicting ΔG_{solv} without scaling, and obtaining errors of 10%, -1%, -1% and 5% with scaling for Li^+, Na^+, K^+ and Cl^-, respectively.

Concluding the discussion on the monovalent ions, the TIP4P/Ew optimized JC ions are found to perform best with the TIP4P/2005 water model in terms of hydration free energy without scaling. When considering the charge scaling, the Benavides and Zeron ions also perform reasonably well. We hypothesize that the TIP4P/Ew optimized ions perform best due to this model also being a 4 point model. In 4 point models, the ionic charge of the water oxygen atom is displaced by a length M ($M = 0.125$ Å in the case of TIP4P/Ew and $M = 0.1546$ Å in the case of TIP4P/2005). Consequently, when transferring ions from SPC/E and TIP3P water models to the TIP4P/2005 water model, the perceived distance r_{ij} in the Coulombic contribution towards the solvation energy increases by 0.1546 Å between cation and water oxygen, reducing $\Delta G^{\text{cation}}_{\text{solv}}$, while that between the anion and water oxygen decreases by 0.1546 Å, increasing $\Delta G^{\text{anion}}_{\text{solv}}$. When transferring ion parameters optimized for the TIP4P/Ew water model to TIP4P/2005, the change in perceived r_{ij} is only 0.0296 Å (0.1546 Å - 0.125 Å), with limited impact on ΔG_{solv}.

Divalent Ions

Fig. 2.6a shows the computed ΔG_{solv} for divalent cations. The values for the Mamatkulov ions depicted in the figure differ from those reported in the original publication [19] due to corrections applied to the data as detailed in Sec. 2.2.1. In short, they computed the single cation ΔG_{solv}, added the contribution of 2 Cl^- anions and used finite system size correction. We reversed these alterations to retrieve the raw single ion hydration energy.

In SPC/E water, nearly identical results are found for the Mamatkulov ions between the predicted and experimental values. In TIP4P/2005 water, a consistent

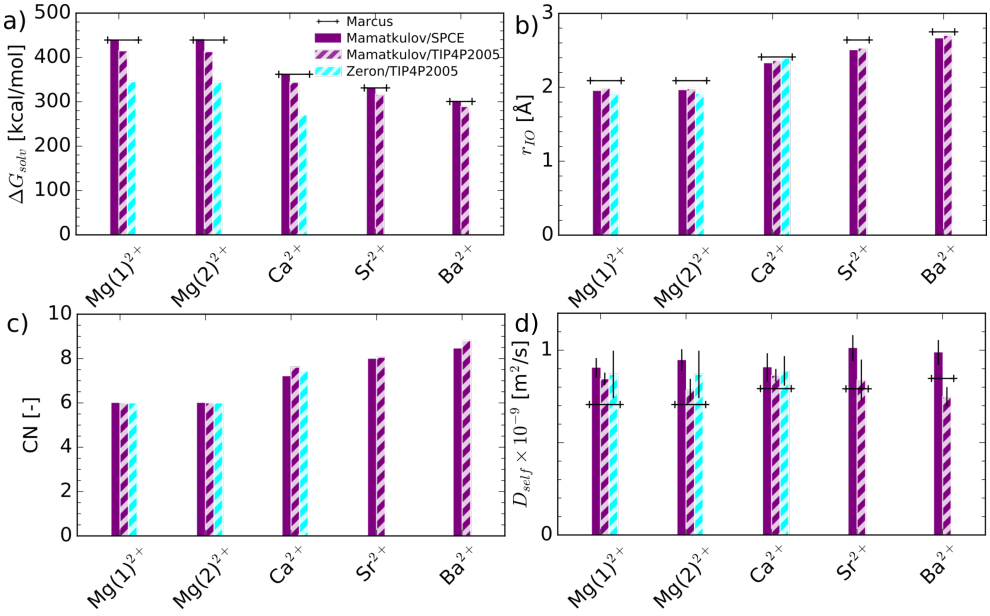

Figure 2.6: Transferability of divalent cation parameters in terms of ΔG_{solv} (a), r_{IO} (b), CN (c) and $D_{i,\text{self}}$ (d). Mg^{2+}(1) and Mg^{2+}(2) account for both parametrizations of Mamatkulov et al. [19]. 95 % uncertainty is shown for $D_{i,\text{self}}$. Other uncertainties were negligible. Experimental results are from Marcus [97].

underprediction in the cation ΔG_{solv} is found, ranging between -4 to -6 % compared to both, the results in SPC/E water and the experimental results. This undepredictionn can be found to be growing as the the hydration energy increases, -4 % for Ba^{2+} and Sr^{2+}, -5 % for Ca^{2+}, and -6 % for Mg^{2+}. This behavior is consistent with the results found for monovalent cations optimized for SPC/E water.

The Zeron ions [22] underpredict the solvation energy by -21 % in the case of Mg^{2+} and -25 % in the case of Ca^{2+}. For monovalent ions it was argued that this underprediction can be partially related to the charge scaling, multiplying ΔG_{solv} by $1/0.85^2$. Applying the same logic to the divalent ions, overpredictions of the experimental results of 8.8% and 3.4% were found respectively.

In conclusion, the Mamatkulov ions perform reasonably well without scaling, while the choice between Mamatkulov and Zeron ions for Mg^{2+} and Ca^{2+} would be based on the desired target properties.

Tri- and Quadrivalent Ions

The HFE obtained from the Li ion parameters [20] optimized for ΔG_{solv} (LiHFE) and r_{IO} (LiIOD) are given in Figs. 2.7a and 2.8a, respectively. From these figures, it appears that the parameters optimized to fit the experimental hydration energy, result in very good agreement between predicted and experimental ΔG_{solv} (± 1 %). On the other hand, the parameters optimized to reproduce the experimental r_{IO}, result in a consistent underprediction of ΔG_{solv} between -6 and -20 %. Despite this, the correct

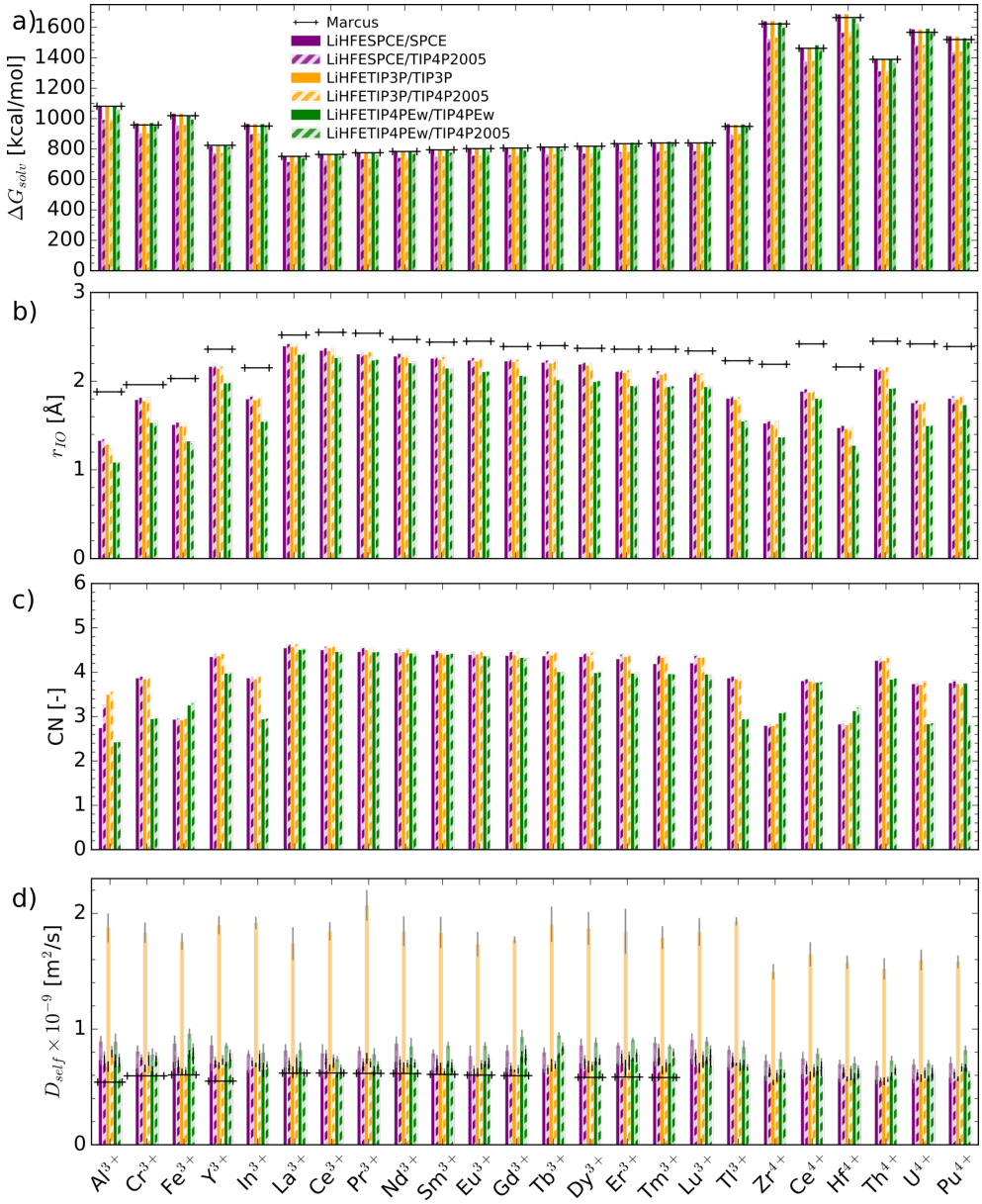

Figure 2.7: Transferability of tri- and quadrivalent cation parameters in terms of ΔG_{solv} (a), r_{IO} (b), CN (c) and $D_{i,\text{self}}$ (d). 95 % uncertainty is shown for $D_{i,\text{self}}$. Other uncertainties were negligible. Experimental results are obtained from Marcus [97].

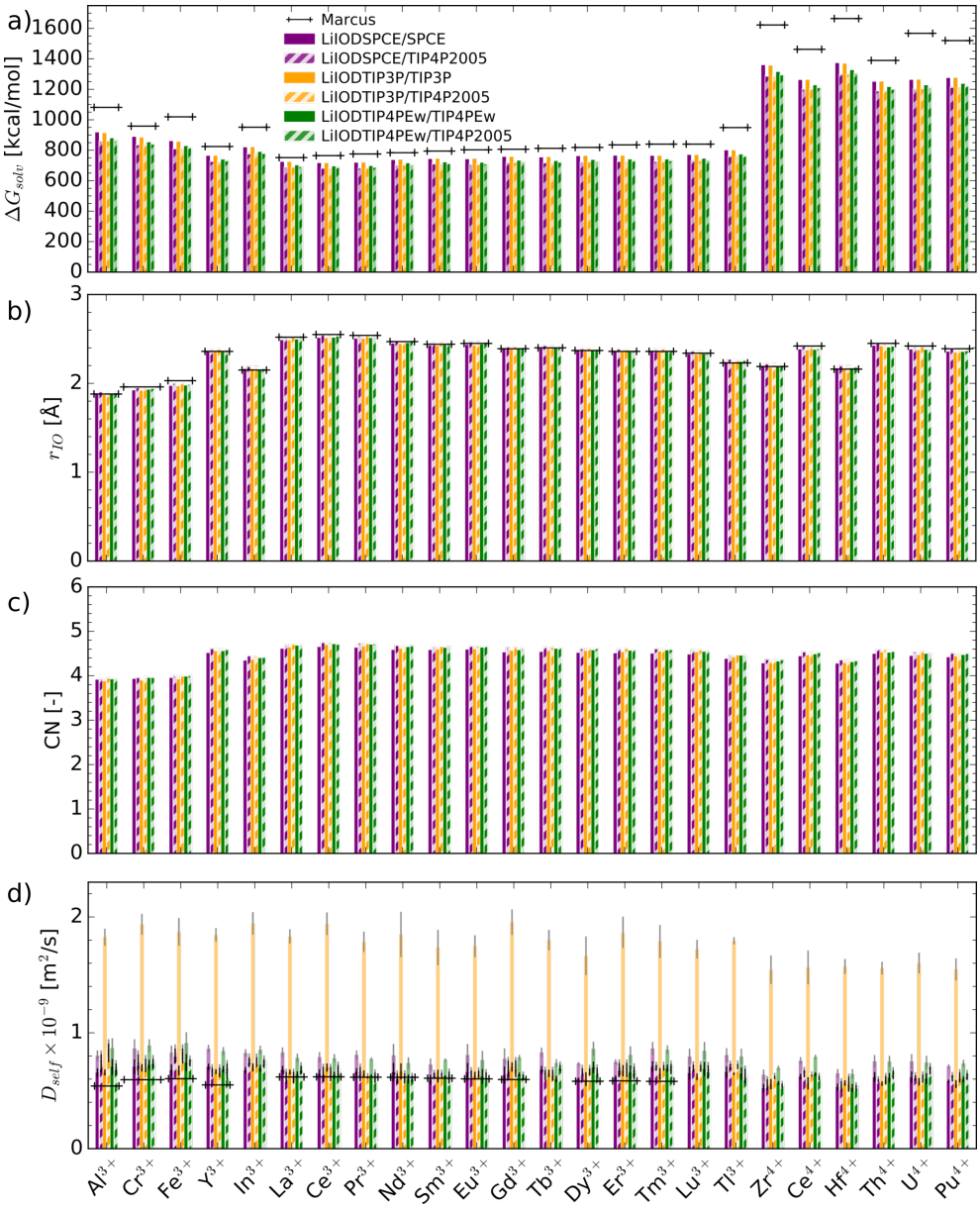

Figure 2.8: Transferability of tri- and quadrivalent cation parameters in terms of ΔG_{solv} (a), r_{IO} (b), CN (c) and $D_{i,\text{self}}$ (d). 95 % uncertainty is shown for $D_{i,\text{self}}$. Other uncertainties were negligible. Experimental results are obtained from Marcus [97].

ordering in terms of ΔG_{solv} emerges, for example $\Delta G_{solv}^{La^{3+}} < \Delta G_{solv}^{Ce^{3+}} < \cdots < \Delta G_{solv}^{Hf^{4+}}$. The only irregularities in terms of the order are between ions for which the experimental ΔG_{solv} are within 10 kcal/mol of each other.

In terms of transferability, the same conclusions as for the JC ions are drawn. The TIP4P/Ew ion parameters transfer best to the TIP4P/2005 water model, with nearly identical results (reduction of up to -2 % in ΔG_{solv}), and the TIP3P ion parameters have the worst transferability. Similarly as for monovalent and divalent cations, tri- and quadrivalent cations optimized for SPC/E or TIP3P water, consistently underpredict ΔG_{solv} when combined with TIP4P/2005. The LiHFE ions display a reduction in ΔG_{solv} between -5 to -8 %, while a reduction of -5 to -6 % is obtained for the LiIOD ions.

2.4.2. Ion-Oxygen Distance and Coordination Number

Monovalent Ions

The radii of first hydration shell for monovalent ions are provided in Figs. 2.4b and 2.5b. In these figures, it is observed that the SD ions combined with SPC/E water provide excellent agreement with the experimental results from Marcus [97] for r_{IO}. Overpredictions are found to be 0.3 % for Na^+ and 1.5 % for Cl^-. When using the same parameters with TIP4P/2005, the agreement remains very good, with errors of 2 % and 1 %, respectively. The respective CN of the first hydration shell are provided in Figs. 2.4c and 2.5c. For the SD ions we find that the CN for Na^+ increases from 5.77(1) to 5.94(1) when in TIP4P/2005 water, while for Cl^- it decreases from 7.23(9) to 6.84(3). These results are within experimental measurement uncertainties found in the literature [99, 100], which place the coordination number of Na^+ between 5 and 6 water molecules and of Cl^- at approximately 6 water molecules.

The JC ions provide good agreement with the experimental results for r_{IO} in SPC/E, TIP3P, TIP4P/Ew and TIP4P/2005 water, with errors up to $\pm$8 %. In terms of transferability of the parameters optimized for the SPC/E and TIP3P water models to the TIP4P/2005 water model, we found that the r_{IO} predictions for cations are consistently increased between 1 and 3 % for SPC/E optimized cations and between 1 % and 2 % for TIP3P optimized cations. For TIP4P/Ew optimized cation parameters on the other hand, almost identical r_{IO} are obtained with both the TIP4P/Ew and TIP4P/2005 water models. All anion parameters showed nearly identical results, with the maximum observed difference being 0.04 Å, considerably below the change in r_{ij} discussed above between 3-site and 4-site water models.

In terms of CN, larger differences between ion parameters and water models can be observed. For example for Cs^+, differences between JCSPCE/SPCE, JC-TIP3P/TIP3P and JCTIP4PEw/TIP4PEw combinations are already significant, ranging between CN=7.97(17) to CN=9.19(31). This large range also persists when combining the JC ion parameters with the TIP4P/2005 water model. For the JCSPCE Cs^+ ion in TIP4P/2005 water, CN = 7.83(7) is found, while for the JCTIP3P Cs^+ ion in TIP4P/2005 water, CN = 8.99(27) is found. For other JC ions, the range of predicted CN with SPC/E, TIP3P and TIP4P/2005 is smaller. Transferability to TIP4P/2005 water shows that the difference in predicted CN between the combinations JC<water model>/<water model>-JC<water model>/TIP4P2005, is smallest for the TIP4P/Ew

optimized ions.

The Benavides ions are found to underpredict the radii of the first hydration shell by -5 % and -3 % for Na^+ and Cl^- respectively, and the Zeron ions by -11.5 %, -1.2 %, -2.5 % and -4.7 % for Li^+, Na^+, K^+ and Cl^- ions, respectively. These values are in good agreement with those reported in their publications [21, 22] at different molalities. The respective CN are 5.31(2), 5.91(5), 4.00(0), 5.53(1) 6.81(8) and 5.79(4).

In conclusion, we recommend the TIP4P/Ew optimized ion parameters (JCTIP4PEw) and the Benavides and Zeron ion parameters when using TIP4P/2005 water in terms of r_{IO} and CN. Furthermore, the SD ions are found to provide remarkable agreement with experimental results when combined with the TIP4P/2005 model.

Divalent Ions

Figs. 2.6b and 2.6c show the r_{IO} and CN found from our simulations with divalent cations. It is observed that the Mamatkulov ion parameters underpredict the radii of the first hydration shell, by -3 % to -7 % when combined with the SPC/E water model, but only -2 % to -6 % when combined with the TIP4P/2005 water model. This increase in r_{IO} for cations is consistent with the results found for monovalent JCSPCE cations (see Fig. 2.5b). Consequently, the combination of Mamatkulov ion parameters with TIP4P/2005 water shows better agreement in terms of r_{IO} with experimental results than with SPC/E water. Along with the increase in r_{IO} when using TIP4P/2005 water, the CN also increases for some cations. For Ca^{2+}, Sr^{2+} and Ba^{2+}, the CN is increased from 7.21(2) to 7.61(3), from 7.99(1) to 8.06(1) and from 8.45(3) to 8.81(4), respectively, while the CN for Mg^{2+} is identical at 6 for both water models. These values are within the experimental ranges reported by Neilson and Enderby [99], 6.5-10 for Ca^{2+}, 8 for Sr^{2+} and 6 for Mg^{2+}.

The Zeron ions predict a r_{IO} of 1.92(0) Å for Mg^{2+} and 2.39(0) Å for Ca^{2+}, resulting in underpredictions of -8 % and -1 %, respectively. This is in agreement with the values reported in [22] of 1.92 Å and 2.38 Å at molalities of 5 mol/kg and 6 mol/kg respectively. The respective CNs are 6 and 7.44 respectively.

In conclusion, both ion parameter sets perform similarly well combined with the TIP4P/2005 water model in terms of r_{IO} and CN.

Tri- and Quadrivalent Ions

The r_{IO} for the LiHFE and LiIOD parameter sets combined with SPC/E, TIP3P, TIP4P/Ew and TIP4P/2005 water are provided in Figs. 2.7b and 2.8b. We find that parameters fitted by Li to predict r_{IO} (LiIOD) result in very good agreement between experimental and predicted r_{IO}. On the other hand, ion parameters optimized to reproduce ΔG_{solv} (LiHFE), show poor agreement in terms of IOD.

Comparing the RDFs obtained with the LiHFE and LiIOD parameters, it becomes clear that optimizing for ΔG_{solv} can provide, what appears to be, completely unrealistic predictions. This is shown in Fig. 2.9 for the Fe^{3+} ion. The results obtained with the LiIOD and LiHFE parameters show different first peak locations and subsequently also the location of the second peak is misaligned. Consequently, the water layering

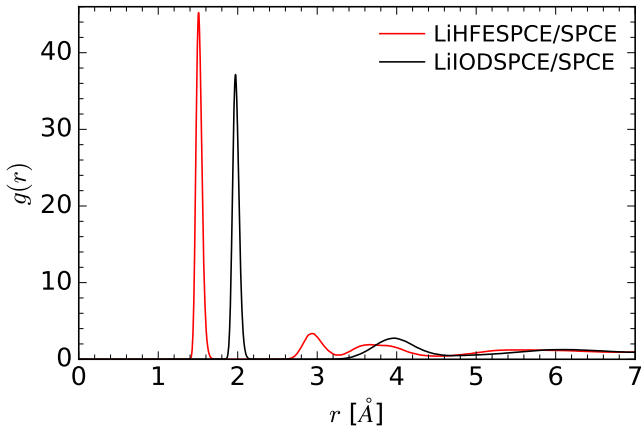

Figure 2.9: RDF for the LiHFE and LiIOD Fe^{3+} ion.

surrounding the Fe^{3+} ion is likely not predicted correctly when using the LiHFE parameters. This behavior is most pronounced for the smallest ions as can be observed in Figs. 2.7b,c and 2.8b,c for r_{IO} and CN. Figs. 2.13a,b and 2.14a,b in show how the misalignment in r_{IO} and CN strongly affects also the second hydration shell. Because of these results, we disregard the LiHFE parameters and only discuss in detail the transferability to TIP4P/2005 water of the LiIOD parameters in terms of r_{IO} and CN.

The r_{IO} and CN predicted when combining the LiIOD cations with TIP4P/2005 follow the same trend as observed for monovalent and divalent cations. For SPC/E and TIP3P optimized cations r_{IO} and CN are increased when combined with TIP4P/2005 water, while for TIP4P/Ew optimized cations nearly identical results are found. Comparing the r_{IO} obtained with TIP4P/2005 water with experimental results, errors of on average 1.4, 1.6 and 0.6 % are found for the LiIODSPCE, LiIODTIP3P and LiIODTIP4PEw ion parameters, respectively.

Concluding, ion parameters optimized for TIP4P/Ew water were found to transfer best to the TIP4P/2005 in terms of r_{IO} and CN.

2.4.3. Ion Self-Diffusion Coefficient

Very few parametrization studies optimize force fields to reproduce experimental ion self-diffusion coefficients. In fact, the self-diffusion coefficient of many ion parameters have not previously been reported, and those that have been reported may deviate substantially from experimental measurements. An exception are the studies from Benavides *et al.* [21] and Zeron *et al.* [22], who computed self-diffusion coefficients at various molalities and compared these to experimental results. Here, we compute the self-diffusion coefficients at infinite dilution, meaning that no concentration effects nor ion-ion interactions are considered, and standard atmospheric conditions, and compare them to experimental values from Marcus [97] in Figs. 2.4d-2.8d.

All ion models considered here overpredict the ion self-diffusion by a factor of more than 2 in combination with the TIP3P water model. It has been proposed [76] that this overprediction can be compensated by scaling the ion self-diffusion by $\eta_{\text{water model}}/\eta_{\text{water}}$ (0.321 mPa·s for TIP3P water, 0.89 mPa·s found experimentally for water at 298 K [101, 102]). Indeed, this scaling was found to provide better agreement with experimental results as shown in Figs. 2.10d-2.14d. However, we argue this scaling to be arbitrary. For example, scaling by $D_{\text{water, }self}/D_{\text{water model, }self}$ also provides better agreement with experimental results ($D_{\text{TIP3P},self} = 5.2 \times 10^{-9}$ m^2/s, $D_{\text{exp},self} = 2.3 \times 10^{-9}$ m^2/s [103]). Yet, both scalings are applied *a posteriori* and do not improve the actual ion diffusion in the simulation. Therefore, we consider the unscaled self-diffusion coefficients from Figs. 2.4d-2.8d for further analysis.

In general, we find that for all ion/water combinations the agreement with experiments is reasonable, except for those including TIP3P water. Starting with the SD ions in Figs. 2.4d and 2.5d, we find that the diffusion in the SPC/E water model is in good agreement with experiments. The simulated diffusion coefficient of Na^+ is extremely close to its experimental counterpart, with 1.32(11) $\times 10^{-9}$ m^2/s predicted from our simulations and 1.33 $\times 10^{-9}$ m^2/s obtained from experiments [97]. The diffusion of Cl^- is worse, underpredicting diffusion by -18 %. When using the SD cation or anion in combination with the TIP4P/2005 water model, it is found that the Cl^- diffusion does not change (within uncertainty), while the Na^+ diffusion is reduced to 1.00(7) $\times 10^{-9}$ m^2/s, corresponding to an underprediction of -8 % compared to experiments. The Benavides Na^+ ion in TIP4P/2005 water shows better agreement with the experimental value, predicting 1.19(4) $\times 10^{-9}$ m^2/s, and the predicted Cl^- self-diffusion is similar to that found with the SD Cl^- ion (1.68(11) $\times 10^{-9}$ m^2/s). These values yield underpredictions of -11 % and -17 %, respectively. The Zeron cations show the best agreement, with self-diffusivities within $\pm$4.5 % of the experimental values, while the Cl^- anion self-diffusivity is underpredicted by 21 %.

The predicted self-diffusion coefficients for the JC Na^+ ion are 1.26(12) $\times 10^{-9}$ m^2/s and 1.06(4) $\times 10^{-9}$ m^2/s for the SPC/E optimized ions in SPC/E and TIP4P/2005, respectively, and 1.26(11) $\times 10^{-9}$ m^2/s and 1.04(5) $\times 10^{-9}$ m^2/s for the TIP4P/Ew optimized ions in TIP4P/Ew and TIP4P/2005, respectively. Hence, combining the JC-SPCE or JCTIP4PEw Na^+ with TIP4P/2005, results in both cases, in a poorer agreement with experimental ion self-diffusion coefficients. The self-diffusion prediction of the JC Cl^- ion deteriorates from -15 % (optimized for and combined with SPC/E) and -16 % (optimized for and combined with TIP4P/Ew) to -28 and -31 % when combined with TIP4P/2005, respectively. This reduction in self-diffusion coefficient prediction in TIP4P/2005 is similarly observed for all other JC ions. The final diffusivities considering both the JCSPCE and JCTIP4PEw ions present errors of +17 to +32 % for Li^+, -20 to -28 % for Na^+, K^+ and Rb^+, -10 to +1 % for Cs^+, and ≈ -30 % for the anions. Thus, whereas the JCTIP4PEw parameters provide nearly identical predictions of ΔG_{solv}, r_{IO} and CN when combined with TIP4P/Ew or TIP4P/2005, the self-diffusion is consistently worse with the latter water model. This finding does not extend to the JCTIP3P parameters. These parameters showed a much too high diffusion when combined with TIP3P, while combining these ion parameters with TIP4P/2005 yielded self-diffusion coefficients of comparable performance to other

ion parameters combined with TIP4P/2005.

For divalent, trivalent and quadrivalent ions similar trends are observed in Figs. 2.6d, 2.8d and 2.8d. These results strongly suggest that the self-diffusion coefficients at infinite dilution are more sensitive to the water model than to small differences in the ion parameters. The sensitivity toward the ion parameters is expected to increase at increasing concentration. Nevertheless, it may prove challenging to derive ion parameters that exhibit realistic self-diffusion across a range of concentrations. At least based on water diffusion coefficients in aqueous solutions, research has suggested that classical MD simulations may be unable to recover the correct concentration dependence [48]. In light of these facts, selecting ion parameters based on their infinite dilution self-diffusion is trivial and by no means guarantees realistic diffusion at finite concentrations.

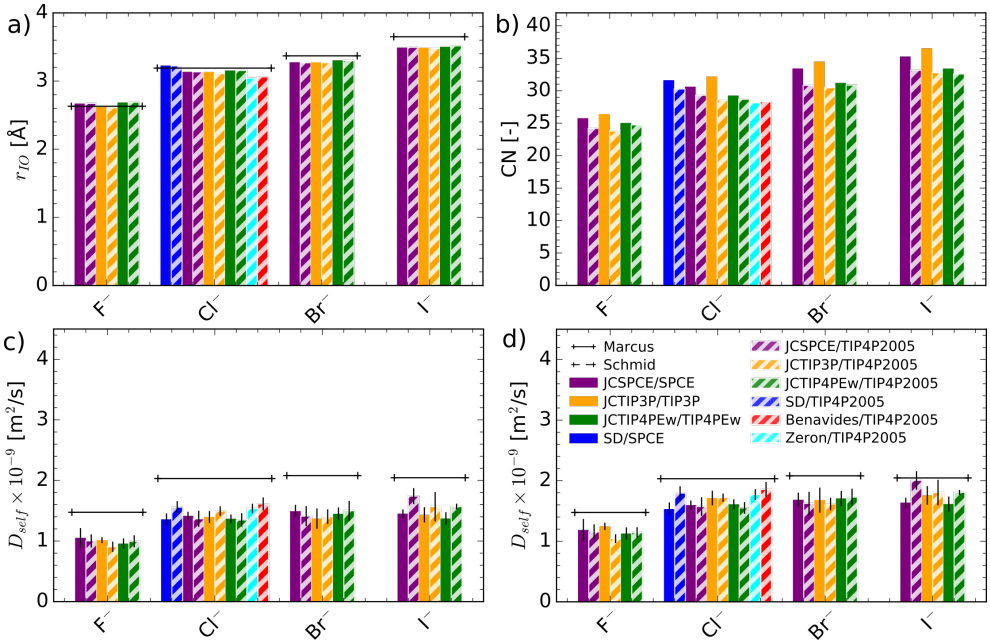

Figure 2.10: Radius (a) and coordination number (b). Scaled diffusion coefficients by $\eta_{\text{model}}/\eta_{\text{exp}}$ (c) and by $Di,\text{exp}/Di,\text{model}$ (b) for monovalent anions.

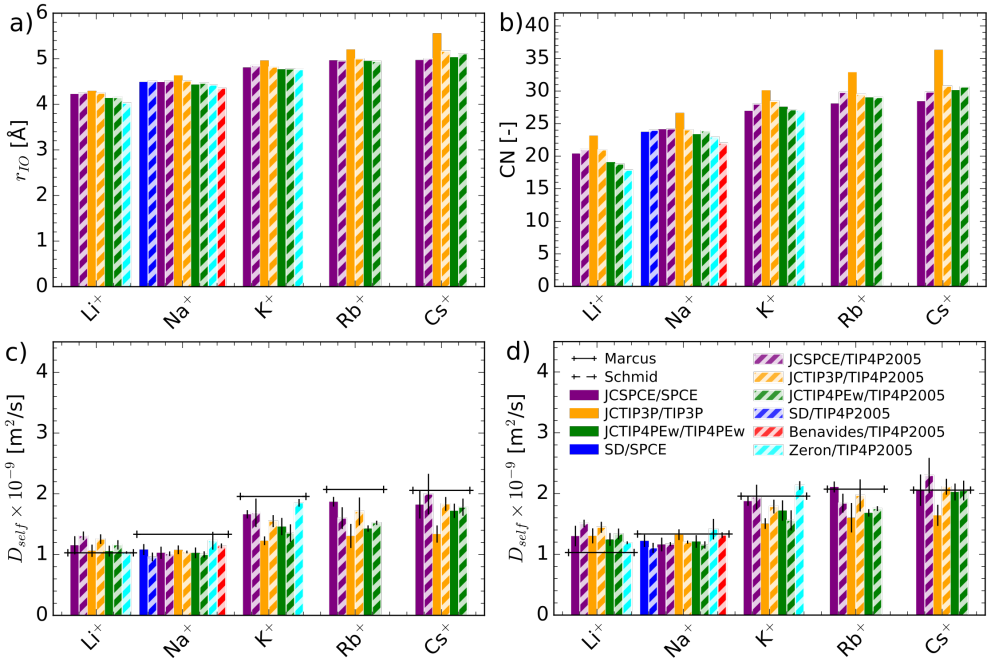

Figure 2.11: Radius (a) and coordination number (b). Scaled diffusion coefficients by $\eta_{\text{model}}/\eta_{\text{exp}}$ (c) and by $Di,\text{exp}/Di,\text{model}$ (b) for monovalent cations.

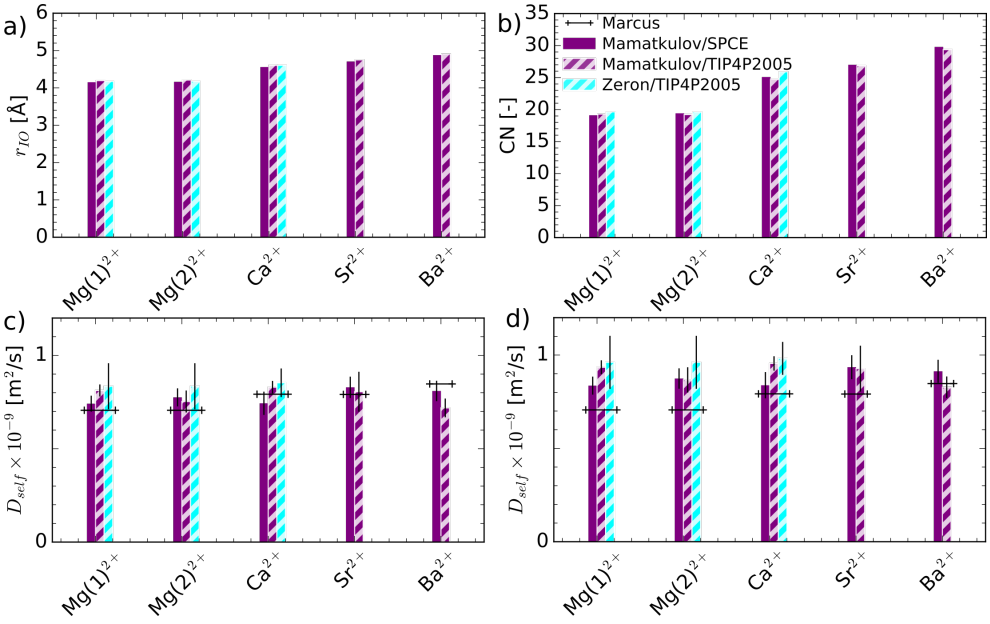

Figure 2.12: Radius (a) and coordination number (b). Scaled diffusion coefficients by $\eta_{\text{model}}/\eta_{\text{exp}}$ (c) and by $Di,\text{exp}/Di,\text{model}$ (b) for divalent cations.

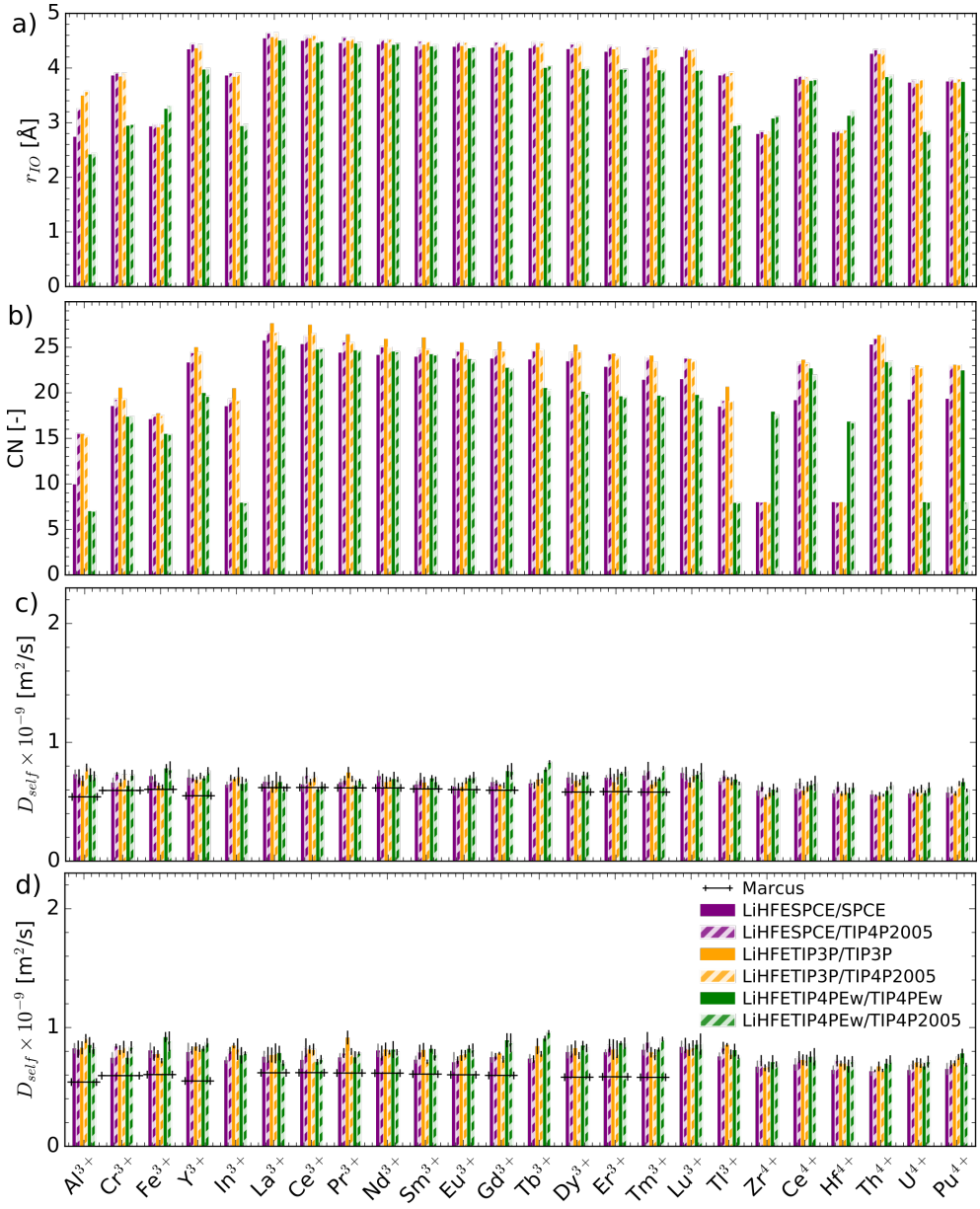

Figure 2.13: Radius (a) and coordination number (b). Scaled diffusion coefficients by $\eta_{\text{model}}/\eta_{\text{exp}}$ (c) and by $Di, \text{exp}/Di, \text{model}$ (b) for trivalent cations optimized for ΔG_{solv}.

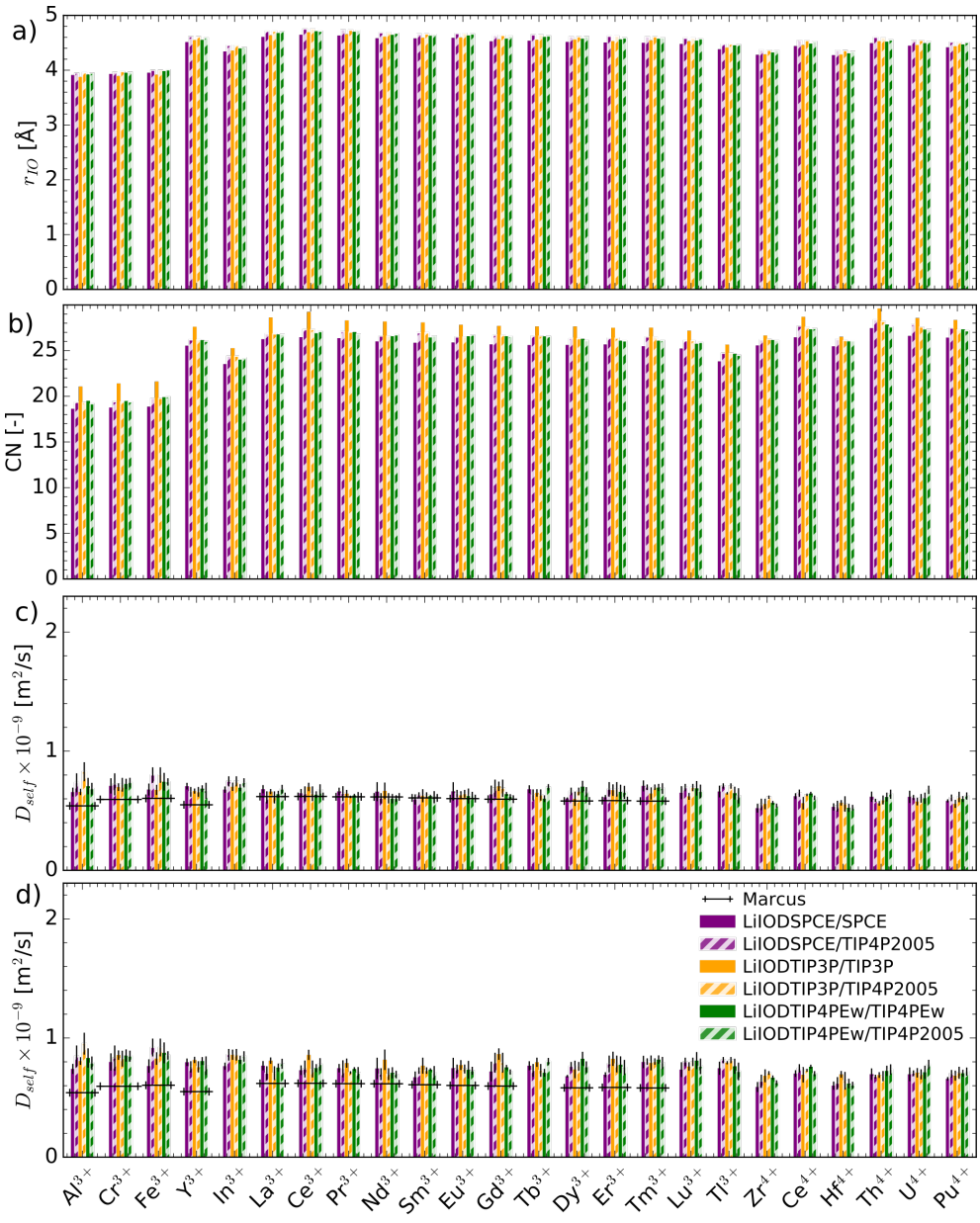

Figure 2.14: Radius (a) and coordination number (b). Scaled diffusion coefficients by $\eta_{\text{model}}/\eta_{\text{exp}}$ (c) and by $Di,\text{exp}/Di,\text{model}$ (b) for trivalent cations optimized for r_{IO}.

2.4.4. Density and Ion Pairing

For selected ion models, the effects of finite concentrations were investigated. Figs. 2.15 and 2.16 display the density and ion pairing of the electrolytes at increasing concentration for the JCTIP4PEw, Mamatkulov and Zeron ion parameters. The JC-TIP4PEw and Mamatkulov ions are found to provide reasonable agreement between experimental and simulated densities, while the Zeron ions provide excellent agreement.

In terms of ion pairing, which is evaluated by counting the number of Contact Ion Pairs (CIPs) between cations and anions, it is found that the JCTIP4PEw and Mamatkulov ions predict more pairing than the Zeron ions. This is most pronounced for LiCl in Fig. 2.15 and for $MgCl_2$ and $CaCl_2$ in Fig. 2.16. For NaCl and KCl, the JCTIP4PEw ions are found to only predict slightly higher ion pairing than the Zeron ions. While experimental data of ion pairing is scarce, the commonly observed ion precipitation or aggregation in MD simulation is often deemed nonphysical [21, 22, 52, 104–107]. Therefore, we believe that the Zeron ions display overall more realistic ion pairing at finite concentrations. The reduction in ion pairing for the Zeron ions is mainly attributed to the scaling of the charges, from 1 to 0.85, which considers the electronic screening of the medium as explained elsewhere [69, 70] . Using the scaled charges, it has also been possible to considerably improve predictions on the solubility limits of electrolytes [21].

In conclusion, scaling the charges as proposed by Leontyev *et al.* [69, 70], and used by Zeron *et al.* [22], appears to provide the best results in terms of density and ion pairing at finite concentrations.

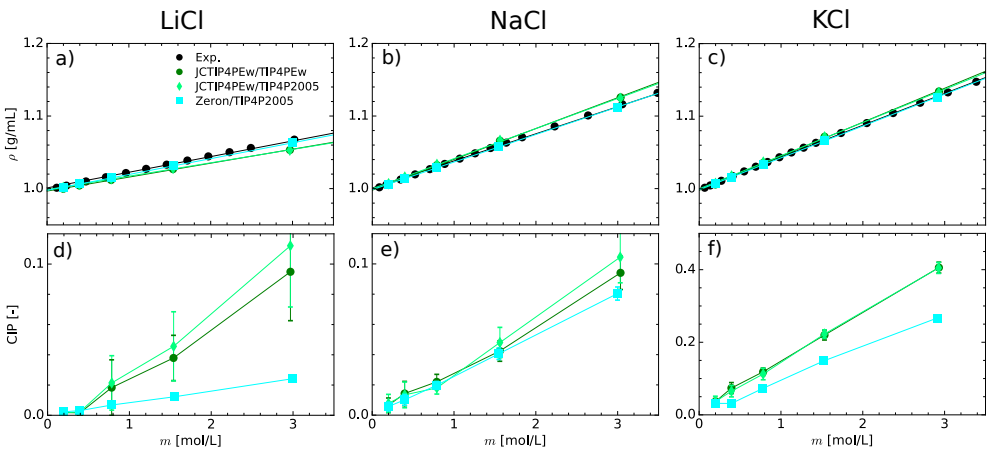

Figure 2.15: Density (ρ) (a, b and c) and fraction of Contact Ion Pairs (CIPs) (d, e and f) vs molarity of the JCTIP4PEw and Zeron LiCl (a and d), NaCl (b and e) and KCl (c and f) ion parameters. Experimental results are taken from Ref. [108]. The errorbars represent the uncertainty with a 95% confidence interval.

2.4.5. Chemical Potential and Mean Ionic Activity Coefficient

The chemical potential and mean ionic activity coefficients, named hereafter only activity coefficients, for the TIP4P/Ew optimized NaCl ions from Joung and Cheatham and the Benavides NaCl ions were computed at various molalities m. The standard chemical potentials $\mu_0^{Na^+} = 137.265$ kcal/mol and $\mu_0^{Cl^-} = -57.401$ kcal/mol needed to solve Eq. (2.21), were taken from the NIST-JANAF thermochemical tables [95].

The upper part of Fig. 2.17 shows the chemical potential against molality, which in the case of the Benavides NaCl is shifted by -44.1 kcal/mol to match the experimental data as reported in Ref. [21]. Our results are found to underpredict μ^{NaCl} when compared with previous results from Mester and Panagiotopoulos [78] and Benavides *et al.* [21] For the JCTIP4PEw/TIP4PEw NaCl combination, the underprediction was found to originate from a difference in ΔG_{solv} of ≈ 0.53 kcal/mol. In fact, shifting the JCTIP4PEw/TIP4PEw NaCl up by 0.53 kcal/mol would provide nearly identical results to those in Ref. [78]. The differences between our results and those from Mester and Panagiotopoulos [78] are attributed to the different methods employed to calculate ΔG_{solv}. We used thermodynamic integration, whereas they used the Bennett acceptance ratio method [110]. Benavides *et al.* [21] also used thermodynamic integration, and no shift is necessary to reproduce their results. However, as the molality increases, so does the difference between our and their results of μ. The dashed black lines denote the solid chemical potential obtained with the respective ion parameters, -93.6 kcal/mol and -47.8 kcal/mol, for the JCTIP4PEw and Benavides NaCl, respectively. The molality at which $\mu_{solid} = \mu_{solution}$ is known as the solubility limit. The solubility of the JCTIP4PEw NaCl in TIP4P/Ew and TIP4P/2005 water is found to be, respectively, 1.9 and 2 mol/kg without shift, and 1.4 and 1.5 mol/kg with

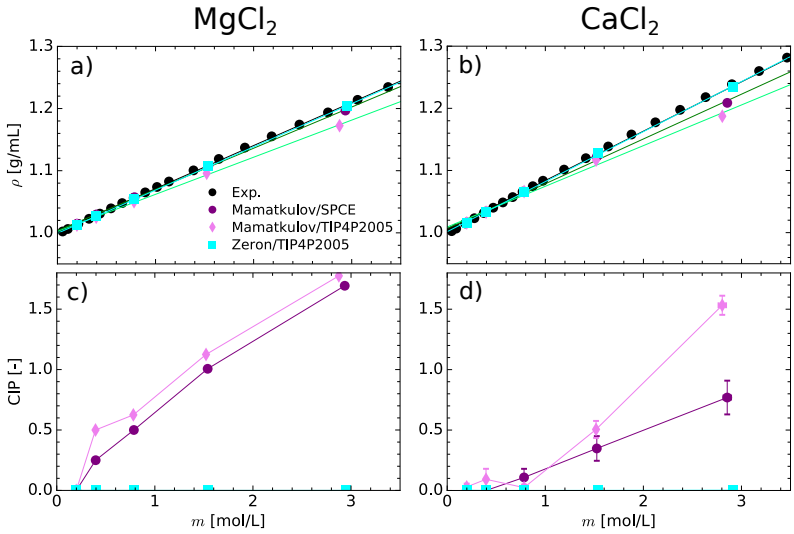

Figure 2.16: Density (ρ) (a and b) and fraction of Contact Ion Pairs (CIPs) (c and d) vs molarity of the Mamatkulov and Zeron $MgCl_2$ (a and c) and $CaCl_2$ (b and d) ion parameters. Experimental results are taken from Ref. [108]. The errorbars represent the uncertainty with a 95% confidence interval.

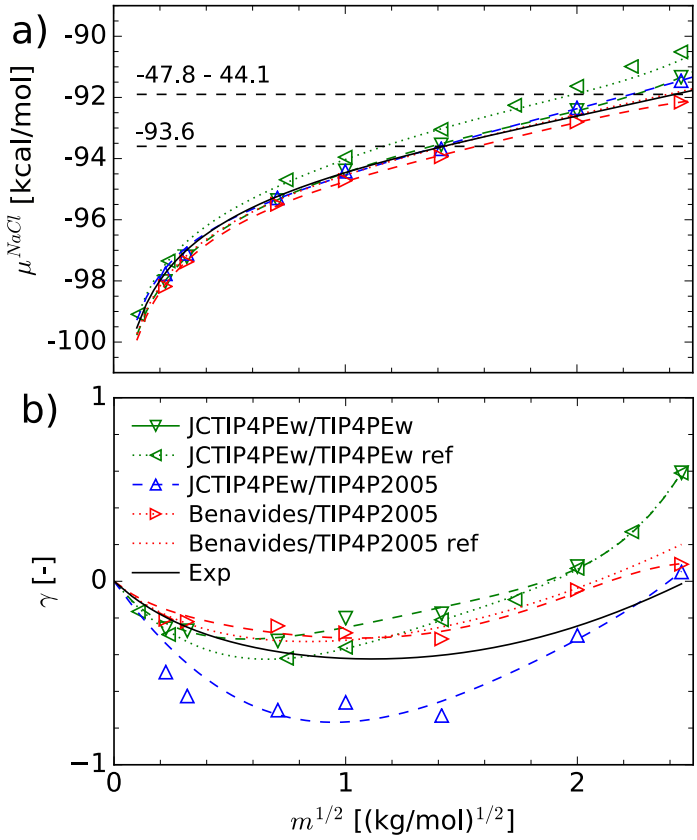

Figure 2.17: Chemical potential (a) and activity coefficients (b) against molality for selected NaCl ion parameters and water models. Experimental results were taken from Hamer and Wu[109]. Reference results were taken from Mester and Panagiotopoulos[78] (JCTIP4PEw/TIP4PEw ref) and Benavides *et al.* [21] (Benavides/TIP4P2005 ref).

shift. For the Benavides NaCl we extrapolate the solubility to be 6.75 mol/kg. These values are in reasonable agreement with those from Mester and Panagiotopoulos [78] and Benavides *et al.* [21] of 1.43 and 5.7 mol/kg, respectively.

The logarithm of the activity coefficients, $\ln\gamma$, shown in the lower part of Fig. 2.17, were obtained by fitting Eq. (2.15) with the chemical potentials obtained from the simulations. The values of the fitting parameters $\mu^{\dagger}$, A, B, b, C and D are given in Tab. 2.1. $\ln\gamma$ was found to be very sensitive to variations in μ and consequently ΔG_{solv}. As a result, the small differences in μ between our results and those previously reported lead to considerable differences in $\ln\gamma$. A constant shift however, as discussed above, has no influence on $\ln\gamma$. Regardless, the experimental trend can be reproduced fairly well, with all ion-water combinations investigated. Despite this, the JCTIP4PEw NaCl parameters are not transferable in terms of activity coefficient as indicated by the large difference between the JCTIP4PEw/TIP4PEw and

Table 2.1: Variable A and fitting parameters B, b, C and D for Eq. (2.15).

	A	B	b	C	D
JCTIP4PEw/TIP4PEw	0.710	2.217	0.142	-0.034	0.004
JCTIP4PEw/TIP4P2005	0.763	0.000	0.467	-0.039	0.002
Benavides/TIP4P2005	0.469	2.702	-0.029	0.023	-0.002

JCTIP4PEw/TIP4P2005 results. The best agreement with the experiments is found for the Benavides NaCl ions.

In conclusion, the Benavides parameters are recommended for the solubility and activity coefficients.

2.5. Conclusions

Transferability of various molecular simulation ion parameters that are frequently used in combination with TIP4P/2005 water was assessed using extensive MD simulations. A single ion was solvated in SPC/E, TIP3P, TIP4P/Ew and TIP4P/2005 water to study its hydration free energy, ion-oxygen distance, coordination number and self-diffusion coefficient. The results were compared to available experimental values and the transferability of ions optimized for other water models to TIP4P/2005 was assessed. Additionally, for selected ions, finite concentration effects were assessed.

The predictions obtained from combining ion parameters with the water model that they were originally optimized with, showed good agreement with experimental results in terms of ΔG_{solv}, r_{IO} and CN. No combination of ion parameters and water model was found to predict accurately the experimental self-diffusion coefficient. It should be noted, that no ion parameters were fitted to reproduce this quantity. While it would be possible to optimize force field parameters to reproduce the experimental ion self-diffusion values at infinite dilution, this would be an arbitrary choice and would likely not yield correct self-diffusion coefficient at any other ion concentration. Activity coefficients can serve as a measure to validate the performance of an ion at finite concentrations as has been shown here as well as by Benavides *et al.* [21].

In terms of transferability, ion parameters optimized for TIP4P/Ew were found to perform best when combined with the TIP4P/2005 water model. The predictions obtained with both water models were not only nearly identical, but also in both cases in very good agreement with experimental results. The SPC/E optimized ions were found to transfer reasonably well. A consistent reduction in the cation ΔG_{solv} and increase in the anion ΔG_{solv} were found. This in turn resulted in good ion pair ΔG_{solv} predictions. Similarly, a consistent increase in the cation r_{IO} was found in TIP4P/2005 water, using SPC/E optimized ion parameters. Finally, the TIP3P optimized ion parameters were found to transfer the worst, with the largest differences between both water models and to the experimental results when combined with the TIP4P/2005 water model.

For highly charged ions we found that parameters optimized to reproduce ΔG_{solv} could lead to unrealistic results in terms of r_{IO} and CN. When optimizing highly

charged ion parameters in terms of r_{IO} however, the prediction of HFE was considered to be better in terms of to the preserved ΔG_{solv} ordering of ions, $\Delta G^{\text{La}^{3+}} < \Delta G^{\text{Ce}^{3+}} < \cdots < \Delta G^{\text{Hf}^{4+}}$. Given this discovery for the highly charged metal ions, we suspect that an efficient calibration routine for ion parameters should start by reproducing the r_{IO}, followed by ΔG_{solv}. In fact, observing the optimization procedure of Joung and Cheatham [18], this is actually done by selecting σ to fit the lattice constant and energy, and adjusting ϵ to match ΔG_{solv}. We expect that whether one fits r_{IO} or lattice constant, should provide a similar result.

In conclusion, based on properties at infinite dilution, TIP4P/Ew optimized ions can safely be combined with TIP4P/2005, while for SPC/E optimized ions, at least the change in ΔG_{solv} should be considered when discussing results. We note that these findings may not extend to properties at finite concentrations as shown in Sec. 2.4.4 and Sec. 2.4.5, such that it is advisable to also validate the transferability at finite concentrations. For example, the TIP4P/Ew optimized NaCl parameters from Joung and Cheatham [18] perform very well in the TIP4P/2005 water model at finite concentrations in terms of density and ion pairing, while the LiCl parameters from the same authors perform well in terms of density, but poorly in terms of ion pairing. Ultimately, we encourage parametrization of more ions specifically for TIP4P/2005 in terms of various properties at infinite dilution and finite concentrations. Additionally, for finite concentrations, scaling the ion charges to consider the electronic screening of the medium appears to provide significant improvement in the results compared to unscaled charges.

3

Surface Roughness can Induce Ion-Specificity

This chapter is based on the paper:

M. F. Döpke, J. Lützenkirchen, O. A. Moultos, B. Siboulet, J. F. Dufrêche, J. T. Padding and R. Hartkamp, *Preferential adsorption in mixed electrolytes confined by charged amorphous silica*, J. Phys. Chem. C, **123**, 16711-16720 (2019).

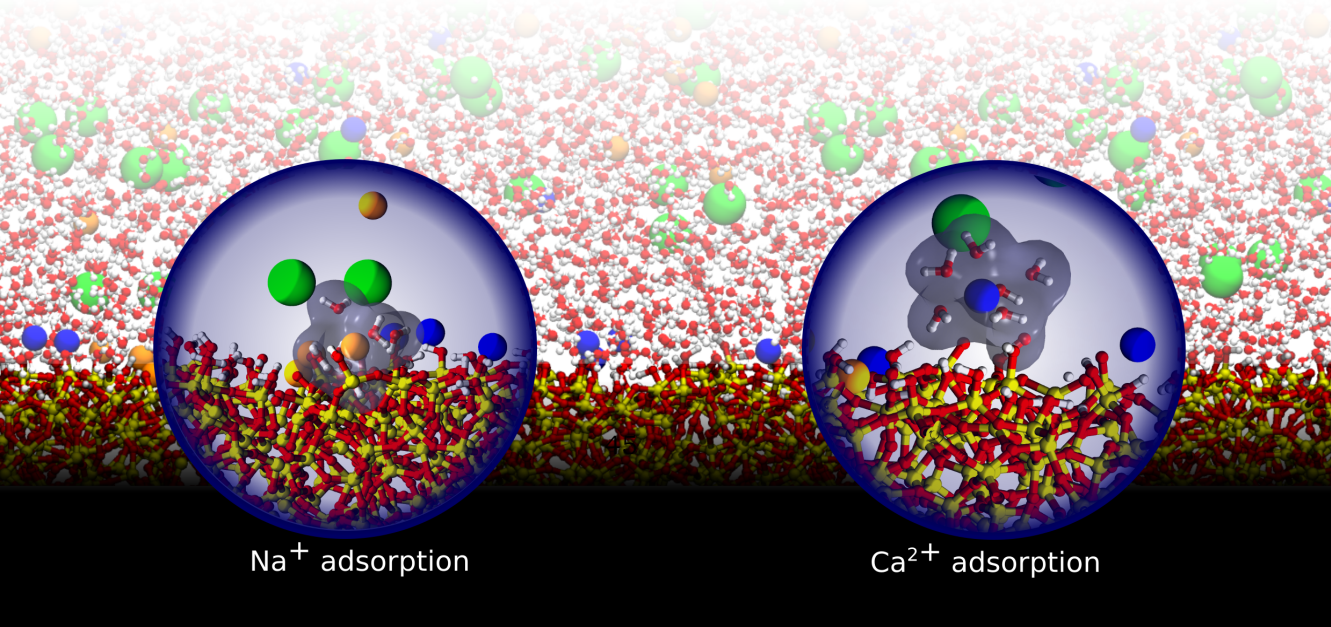

3.1. Introduction

Most fluids in nature are complex aqueous solutions containing multiple electrolytes, possibly in combination with other organic and inorganic compounds. Nanoscale properties of these mixtures at fluid-solid interfaces can be exploited for applications such as soil analysis, ion separation and water purification [111–113]. Silica surfaces are among the most widely studied, due to their omnipresence in nature, their bimodal chemical character [114], and their use in a wide range of applications [115–117], including catalysis [118] and ion sensing [59, 119].

Oxide surfaces in contact with aqueous solutions assume an electric charge as a result of protonation and deprotonation of ionizable groups [25]. The silica surface is negatively charged above the point of zero charge ($pH_{pzc} \approx 2-3$) [120], attracting cations whilst repelling anions, forming a so-called Electrical Double Layer (EDL). The exact distribution and movement of ions and solvent molecules in the EDL determine, for example, transport along the surface and charge storage at the surface. However, no single experimental technique can unambiguously measure the three-dimensional distribution, orientation and motion of molecules constituting the fluid. In theory, the full picture could be constructed by combining the partial information inferred from multiple techniques, but it is difficult to replicate identical environmental conditions and samples in different experimental setups. Moreover, various techniques (e.g., atomic force microscopy (AFM), titration and electrokinetic techniques) rely on fitting measurement data to EDL models (e.g., Gouy-Chapman-Stern-Grahame [2] shown in Fig. 3.1) to infer quantities that cannot be directly measured. Such models are based on *a priori* assumptions, such as that the solid surface is flat and homogeneous, fluid transport coefficients are constant in space, and the Stern and diffuse layers are distinct. These assumptions may be suitable only under certain idealized conditions, thus limiting the accuracy and interpretation of inferred quantities for most systems of interest [1].

A bottom-up approach, such as Molecular Dynamics (MD) simulation, can provide detailed insight into the molecular structure and dynamics at the nanoscale. Various EDL properties can be directly and locally calculated from the position and motion of atoms, without the need for an EDL model to infer information. As such, molecular simulations offer an appealing alternative approach to gain detailed insight into EDL properties. Furthermore, insight from MD simulations can aid in improving the models used to interpret experimental observations [1].

Numerous MD studies have expanded our knowledge of interfacial fluid phenomena on silica surfaces in recent years. For example, water structure and dynamics on crystalline silica was studied extensively by Argyris *et al.* [121, 122], and on amorphous silica, by Hassanali *et al.* [123, 124] and by Bourg and coworkers [125, 126]. With water-silica interfaces better understood, focus has shifted towards simple, single compound, electrolyte-silica interfaces [54, 113, 125, 127–135]. For example, Haria *et al.* [129, 130] found that charged amorphous silica nanopores show selectivity for ions to enter depending on the pore size and ionic and hydration radii. Ionic and hydration radii based adsorption selectivity on β-cristobalite was also observed by Ho *et al.* [132], who suggested that ion-surface and ion-water interactions dominate over ion-ion interactions for NaCl or CsCl systems. Recently, Hartkamp *et al.*

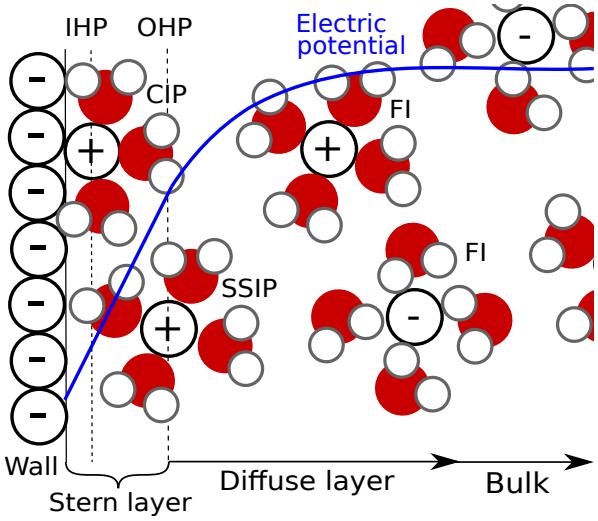

Figure 3.1: Gouy-Chapman-Stern-Grahame EDL model on smooth surfaces, with the Stern and diffuse layer, and the bulk region. The Stern layer is delimited by the Outer Helmholtz Plane (OHP), passing through the nuclei Solvent-Separated Ion Pairs (SSIP), whereas an Inner Helmholtz Plane (IHP) passes through Contact Ion Pairs (CIP).

[54] found that adsorption follows a reversed Hofmeister series, $Na^+ < K^+ < Cs^+$, with the smallest ion adsorbing closest to the surface, and the largest the furthest away. This effect was attributed to ionic radius, but may in fact better be seen as a function of the hydration radius. Later, using the McMillan–Mayer Potential of Mean Force (PMF), Hocine *et al.* [134] calculated the binding energy of Li^+ and Cs^+ on amorphous silica and found a much stronger binding energy for Li^+, and correspondingly a much longer adsorption residence time.

Although molecular simulations have contributed to an improved understanding of solid-electrolyte interfaces, many studies have suffered from drastic simplifications pertaining to the representation of the surface, the solvent or the electrolyte. With regard to the surface, many studies have considered smooth model surfaces [136, 137]. Furthermore, most MD studies make use of rigid surfaces, limiting mobility induced from vibration of surface atoms, which can influence adsorption properties as well as slip along a surface [138]. The working fluid in most MD simulation studies has been an aqueous solution of simple, monovalent electrolytes, such as NaCl or KCl, whereas most solutions in nature and industry contain a mix of electrolytes. Experimentally, it has been shown that adding even a small amount of different ions to an electrolyte solution can severely impact EDL properties [59, 139, 140]. This can happen for example if the added electrolytes show preferential adsorption, or if they severely affect the hydrogen bond network of the solvent at the interface. Especially the addition of multivalent ions to a predominantly monovalent solution can strongly reduce the efficiency of reverse electrodialysis [141] and can invert the direction of electrokinetic flow [140].

The first fully atomistic MD simulations of electrolyte mixtures on siliceous surfaces were carried out by Bourg and Sposito [113] in 2011, who investigated NaCl–$CaCl_2$ mixtures on a rigid smectite surface and found that Na^+ and Ca^{2+} ions can coexist in the Stern layer, with no clear preferential adsorption. In similar MD simulations on rigid mica surfaces however, preferential adsorption of K^+ over Rb^+ and Mg^{2+} was found [142]. Cavities in which K^+ ions could adsorb, were not accesible to Rb^+ and Mg^{2+} ions, which have larger hydration radii. To our knowledge, only one MD study has considered mixed electrolytes on amorphous silica. Prakash *et al.* [135] evaluated electroosmotic flow on a rigid amorphous silica surface at varying compositions of NaCl–$MgCl_2$ solutions, stating that Na^+ preferentially adsorbs over Mg^{2+}. This was motivated by the fact that Na^+ displayed a closer proximity to the surface and has a lower hydration energy than Mg^{2+}. However, the balance between adsorption energy and hydration energy was not considered. Furthermore, we argue that the closer proximity of Na^+ ions does not demonstrate preferential adsorption, but rather is a consequence of its smaller hydration radius. Conversely, a recent primitive model Monte Carlo study suggested that divalent ions adsorb preferentially over monovalent ions when discrete charges are present on a model surface [143]. A comprehensive study of ion adsorption with mixed electrolytes on realistic amorphous silica surfaces is lacking.

In this chapter, we provide one of the first studies of ion adsorption from mixed electrolytes confined by flexible charged amorphous silica. Adsorption of ions in single and mixed electrolytes is compared by analyzing the distribution of ions near a charged silica surface. Specifically, ions are classified based on their adsorption, forming a Contact Ion Pair (CIP) or Solvent-Separated Ion Pair (SSIP) with the surface (see Fig. 3.1), to asses the impact of adsorption type on the EDL structure. This classification is analogous to Inner- and Outer-Sphere Surface Complexes (ISSC and OSSC) used by, for example, Bourg and Sposito [113]. Furthermore, the strong influence of the surface roughness on the EDL structure is illustrated by computing for each ion the distance to the nearest surface atom. Finally, we provide selectivity maps for our system, and relate the observed selectivities to the structural characteristics of the surface, allowing us to devise a protrusion metric (PM) based on steric properties, which is successfully used to predict ion-specificity.

The remainder of this chapter is organized as follows: the simulation set-up is described in Sec. 3.2. The results are given in Sec. 3.3 discussing adsorption of ions in single (one compound) and mixed (multiple compounds) electrolytes. Conclusions are presented in Sec. 3.4.

3.2. Methods

3.2.1. Generating Amorphous Silica

A block of 5 nm × 5 nm × 5 nm amorphous silica was created by annealing (from 298 K to 4000 K) and quenching (from 4000 K to 298 K at a rate of 2.5 k/ps) a $\beta-$cristobalite in the NVT ensemble (density of 2.2 g/cm^3) with periodic boundary

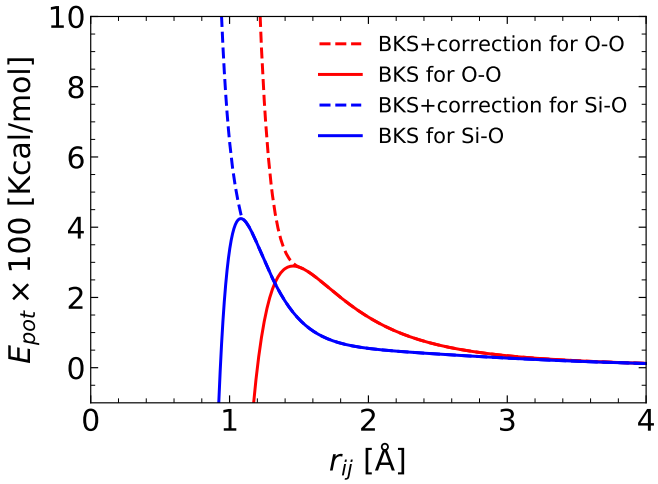

Figure 3.2: Potential energy of the BKS potential with and without LJ correction.

Table 3.1: Force field parameters for the BKS force field and its modification. Partial charges are assigned as follows: $q_O = -1$ e and $q_{Si} = +2$ e. Units of $C_{ij}^{(n)}$ are in KcalÅ^n/mol

	A_{ij} [Kcal/mol]	b_{ij} [Å]	c_{ij}	$C_{ij}^{(12)}$	$C_{ij}^{(6)}$
O-O	32026	2.76	175	281743	-2275.22
O-Si	415176	4.87	133.54	13776	1127.08

conditions using the modified BKS potential [24, 144, 145].

$$E_{pot} = \begin{cases} A_{ij}\exp\left(-b_{ij}r_{ij}\right) - \frac{c_{ij}}{r^6} + \frac{1}{4\pi\varepsilon_0}\sum_{ij}\frac{q_i q_j}{r_{ij}} & \text{for } r > r_{s,ij} \\ \frac{\exp\left(r - r_{s,ij}\right)}{10}\sum_{ij}\left[\frac{C_{ij}^{(12)}}{r_{ij}^{12}} - \frac{C_{ij}^{(6)}}{r_{ij}^{6}}\right] - & \\ A_{ij}\exp\left(-b_{ij}r_{s,ij}\right) + \frac{c_{ij}}{r_{s,ij}^6} - \frac{1}{4\pi\varepsilon_0}\sum_{ij}\frac{q_i q_j}{r_{s,ij}} & \text{for } r < r_{s,ij} \end{cases} \tag{3.1}$$

Essentially, a Lennard-Jones (LJ) potential is added in order to eliminate the nonphysical attractive forces that originate from the Buckingham potential when two atoms move too close to each other, modifying the potential energy curves as shown in Fig. 3.2. The attractive forces of the BKS potential are reversed to repulsive forces at distances below $r_{ij} = 1.09$ for O−O interactions and $r_{ij} = 1.50$ for O−Si interactions. The corresponding force field parameters are summarized in Tab. 3.1. The temperature was controlled with the Nosé-Hoover thermostat with a damping factor of 100 dt, and the simulation time step was set to 1 fs.

The obtained block of amorphous silica can be shown to be in line with experiments [146–148] and previous MD studies [24, 129, 149, 150] with over- and un-

Table 3.2: Occurrence of structures in our amorphous silica block.

Structures	Occurrence
SiO_3	00.11 %
SiO_4	99.85 %
SiO_5	00.04 %
OSi_1	00.11 %
OSi_2	99.82 %
OSi_3	00.07 %

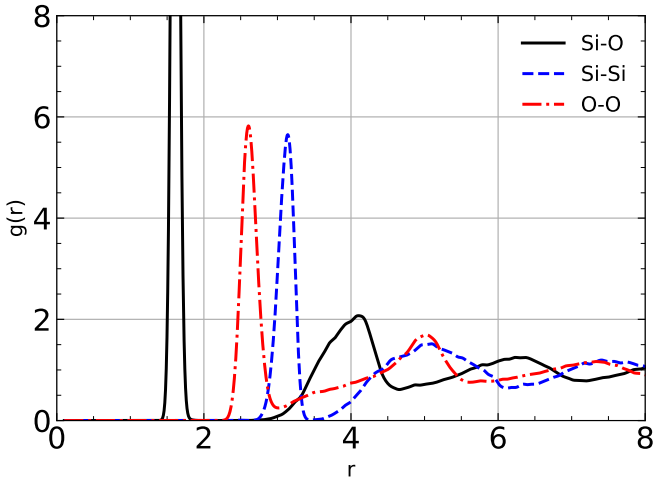

Figure 3.3: Silica RDFs for the amorphous silica block obtained in this study.

dercoordinated structures making up less than 0.2% as shown in Tab. 3.2 and the location of first and second peaks in the radial distribution functions (see Eq. (2.12) and Fig. 3.3) to be in agreement with known results (Tab. 3.3).

3.2.2. Creating a Channel

The channel configuration was generated by cutting the amorphous silica block and separating the two resulting slabs. Subsequently, undercoordinated silicon and uncoordinated oxygen atoms were removed. Undercoordinated oxygen atoms were protonated, resulting in a silanol (SiOH) density of 6.5 SiOH/nm^2. The silanol density was reduced to 5 SiOH/nm^2 (close to the experimental value [151]) by condensating silanols [152]). Condensation of vicinal silanol pairs was avoided to ensure that no strained two-membered siloxane rings were formed [153, 154]. The remaining surface groups consisted of 15% isolated, 50% vicinal and 35% geminal silanols, in line with other studies of amorphous silica [151] (see Fig. 3.4 for a representation of the silanol types). On either wall, 16 SiOH were deprotonated to impose a surface charge of -103 mC/m^2, corresponding to a pH of 7-8 (depending on electrolyte composition

Table 3.3: Location of first and second peaks in rdf for amorphous silica. Rdfs for own simulations following equation 2.12 are given in Fig. 3.3. [a] Ref. [146], [b] Ref. [148] and [c] Ref. [147].

	Simulation [Å]	Vollamyr *et al.* [24] [Å]	Experiments [Å]	
Si-O	1.61	1.595	1.608[b]	1.620[a]
	4.10	4.12		4.15
O-O	2.60	2.59	2.626[b]	2.65[a]
	5.02	5.01		4.95
Si-Si	3.14	3.16	3.077[c]	3.12[a]
	5.09	5.05		5.18

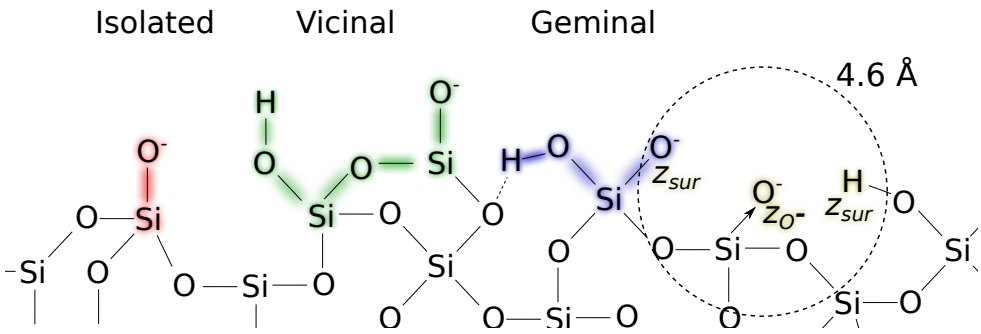

Figure 3.4: Silanol classification for isolated (red), vicinal (green), and geminal (blue) silanols. In yellow is shown how the protrusion metric (PM) is computed considering surface atoms within 4.6 Å of z_{O^-}.

and concentration) [25].

In between the resulting slabs, 3,485 water molecules were added in a dilute lattice, along with a variable number of ions (Cl^-, Na^+ and Ca^{2+}, listed in Tab. 3.4), with an excess of cations to balance the surface charge (see Fig. 3.5 for a depiction of the system). The fluid density was adjusted via a compression force equivalent to 1 bar by moving the walls towards each other for 10 ns [155]. The electrolyte compositions used in this study are provided in Tab. 3.4, with molarities in the center of the channel computed after adjusting the fluid density.

3.2.3. Computational Details

The channel simulations were performed in the NVT ensemble with periodic boundary conditions, removing inter-slab interactions across the z boundary [156], with a time step of 1 fs. The Nosé-Hoover thermostat was used to control the temperature with a damping factor of 100 dt. Long range electrostatic interactions were computed with the particle-particle particle-mesh (pppm) method with a relative precision of 10^{-4}. Cut-off distances of 12 Å and 8.5 Å were used for Lennard-Jones (LJ) and Coulombic interactions, respectively. The Lorentz-Berthelot mixing rule (see Eq. (1.7)) was used to parametrize LJ interactions between dissimilar particles. The Interface Force Field (IFF) parametrization from Emami *et al.* [149] was used for silica, TIP4P/2005 [16] for water, and Joung and Cheatham [18] and Mamatkulov *et al.* [19] for ions. The

Table 3.4: Electrolyte compositions used in this study with final densities and molarities at the centre of the channel in a 4 Å bin. The excess of counterions can be calculated from the difference between anions and cations forming a molecule.

Name	Number of ions			Density	Molarity [mol/L]	
	Cl^-	Na^+	Ca^{2+}	[g/mL]	NaCl	$CaCl_2$
0.1Na	6	38		1.001(4)	0.16(1)	
0.3Na	19	51		1.006(5)	0.35(1)	
0.6Na	38	70		1.019(4)	0.67(1)	
0.9Na	57	89		1.029(5)	0.91(2)	
0.15Ca	18		25	0.996(5)		0.10(1)
0.3Ca	38		35	1.011(5)		0.27(1)
0.3Na0.15Ca	38	34	18	1.014(5)	0.32(2)	0.14(1)
0.3Na0.3Ca	56	34	27	1.033(6)	0.40(2)	0.25(1)

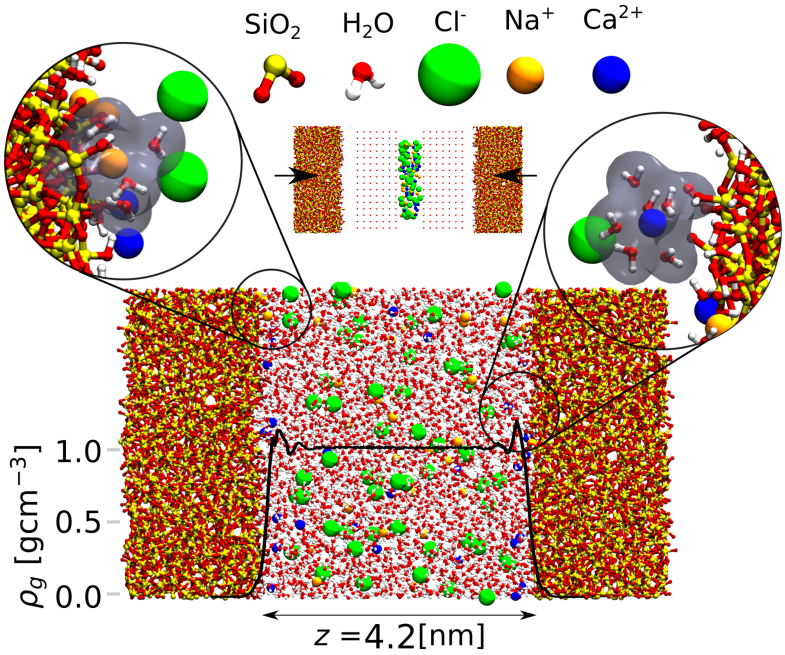

Figure 3.5: Channel configuration for simulations. Silica walls are separated roughly 4.2 nm with fluid in between at a density of ≈ 1 g/cm^3. The top shows the initial configuration with arrows indicating the movement of the walls due to the applied force equivalent to 1 bar to adjust the fluid density. The left inset shows Na^+ adsorption with part of the hydration shell penetrating into the wall. Right inset shows adsorption of a partially hydrated Ca^{2+} ion.

respective functional form is

$$E_{pot} = \sum_{ij,\text{nonbonded 1-2,1-4 incl and 1-3 exl}} \epsilon_{ij}\left[\left(\frac{\sigma_{ij}}{r_{ij}}\right)^{12} - 2\left(\frac{\sigma_{ij}}{r_{ij}}\right)^{6}\right] + \frac{1}{4\pi\varepsilon_0}\sum_{ij,\text{nonbonded 1-2,1-4 incl and 1-3 exl}} \frac{q_i q_j}{r_{ij}} + \sum_{ij,\text{bonded}} k_{r,ij}\left(r_{b,ij} - r_{b0,ij}\right)^2 + \sum_{ijk,\text{bonded}} k_{r,ijk}\left(\theta_{ijk} - \theta_{0,ijk}\right)^2 \tag{3.2}$$

with the force field parameters being described in Tab. 3.5. IFF has been shown to provide physically and chemically very consistent parameters compared to other force fields that are commonly used to model silica, such as clayFF [157–159]. Furthermore, flexible silica walls can easily be simulated with IFF due to the presence of bond and angle parameters. Despite IFF being parametrized together with TIP3P and SPC, TIP4P/2005 was chosen for water due to the fact that this model more accurately reproduces a range of physical and thermodynamic properties [40]. Oxygen-hydrogen (OH) bond lengths and HOH angles were constrained with the SHAKE algorithm [160]. All simulations in this study were performed with the LAMMPS simulation package [80].

Two independent simulations of 35 ns were performed for each system given in Tab. 3.4. The last 25 ns were used to gather statistics at 5 ps intervals. An additional simulation of 122 ns was performed for the 0.3Na0.3Ca system to study ion selectivity at the surface. Runs of 11 ns were alternated with runs of 10 ps with charges switched to $q_{Na} = -0.5$, $q_{Ca} = -0.5$ and $q_{Cl} = +1.116$. This modification in ionic charges was found to be sufficient to quickly desorb the adsorbed ions, such that a new independent configuration can be obtained. This process was repeated 11 times, gathering statistics throughout the last 1 ns of each 11 ns segment.

3.2.4. Uncertainty Quantification

For each individual simulation, the standard error was evaluated ensuring each sample was uncorrelated to the former sample. The correlation of the position of water molecules $\mathbf{r}_{O_w}$ between frames (at a time interval τ) was studied following the approach described by Allen and Tildesley [8]. The correlation function

$$c(\tau) = \frac{\langle \delta\mathbf{r}_{O_w}(t)\delta\mathbf{r}_{O_w}(t+\tau)\rangle}{\sigma_{\mathbf{r}_{O_w}(t)}\sigma_{\mathbf{r}_{O_w}(t+\tau)}} \tag{3.3}$$

with

$$\delta\mathbf{r}_{O_w} = \mathbf{r}_{O_w} - \langle\mathbf{r}_{O_w}\rangle \tag{3.4}$$

and

$$\sigma^2_{\mathbf{r}_{O_w}} = \langle\left(\mathbf{r}_{O_w}(t)\right)^2\rangle - \langle\mathbf{r}_{O_w}(t)\rangle^2 \tag{3.5}$$

was evaluated and block averaging was used yielding the same conclusion of uncorrelated results as shown in Fig. 3.6. The correlation function drops to nearly zero

Table 3.5: Force field parameters for channel simulations. Subscripts are as follows: w-water, b-bulk, d-dangling, dd-dangling dangling, s-silanol, ss-silanol silanol. * partial charge was adjusted from original force field to support doubly deprotonated geminals.

Ions	σ [Å]	ϵ/k_B [K]	q [e]
Na^+ [18]	2.1845	84.7616	+1
Ca^+ [19]	2.8331	140.6332	+2
Cl^- [18]	4.9178	5.8683	-1
TIP4P/2005 [16]	σ [Å]	ϵ/k_B [K]	q [e]
O	3.1589	93.19685	
H			+0.5564
M			-1.1128
IFF [149]	σ [Å]	ϵ/k_B [K]	q [e]
Sib	3.70	46.799	+1.1
Sid	3.70	46.799	+0.725
Sidd	3.70	46.799	+0.35*
Sis	3.70	46.799	+1.1
Siss	3.70	46.799	+1.1
Ob	3.09	27.174	-0.55
Od	3.09	61.392	-0.9
Os	3.09	61.392	-0.675
H			+0.4
IFF bonds [149]	k_r [Kcal/(mol Å^2)]		$r_{0,ij}$ [Å]
Si-O	285		1.68
IFF angles [149]	k_θ [Kcal/(mol rad^2)]		θ_0 [°]
O-Si-O	100		109.5
Si-O-Si	100		149.0
Si-O-H	50		115.0

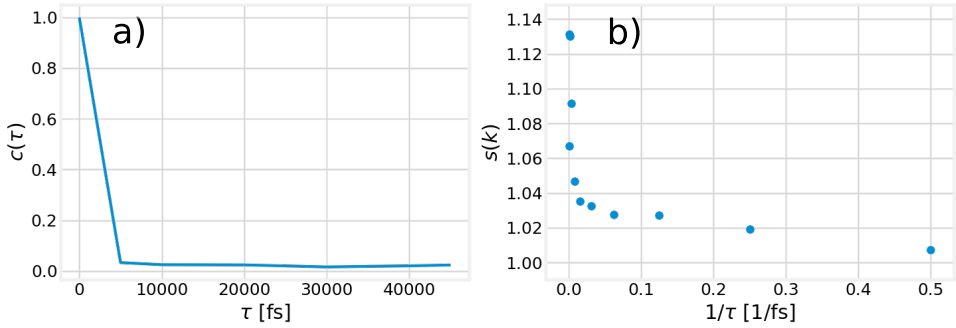

Figure 3.6: Correlation function (a) and inefficiency factor from block averaging (b) of water positions.

at the immediate next recorded time step, and reducing the size of the blocks does not increase the statistical inefficiency $s(k)$ significantly above 1. Hence each sample can be considered as fully independent.

The standard error for each individual simulation was defined as:

$$\mathrm{SE}_{\mathrm{individual}} = \frac{\sigma_{\mathrm{individual}}}{\sqrt{N_{\mathrm{frames}}}}, \tag{3.6}$$

with

$$\sigma^2_{\mathrm{individual}} = E(x^2) - E(x)^2. \tag{3.7}$$

The error $\mathrm{SE}_{\mathrm{multi}}$ between simulations and from symmetrizing was computed following

$$\mathrm{SE}_{\mathrm{multi}} = \frac{\sigma_{\mathrm{multi}}}{\sqrt{N_{\mathrm{simulations}}}} = \sqrt{\frac{1}{N_{\mathrm{simulations}}} \sum_{X=0}^{N_{\mathrm{simulations}}} (\mu_X - \mu)^2} \tag{3.8}$$

where μ_X represents the ensemble averages of each simulation and μ the average between simulations. The final uncertainty was obtained from the addition of Eqs. (3.6) and (3.8).

For the screening function the assumption $\Gamma(\chi = 0) = \sigma_0$ and $\Gamma(\chi = \infty) = 0$ was further made, such that Eq. (3.12) is integrated from both directions to avoid cumulative additions of the SE, yielding

$$SE_\Gamma(\chi) = \frac{\int_{\min(\chi)}^{\chi} \sum_i SE_{\rho_{n,i}}(\chi') z_i d\chi' + \int_{\chi}^{\min(\chi)} \sum_i SE_{\rho_{n,i}}(\chi') z_i d\chi'}{2}. \tag{3.9}$$

3.2.5. Symmetrizing of Results

The density profiles ρ_n vs z are symmetrized with respect to the centre of the channel and shifted by the average location of surface Oxygen atoms. Density profiles ρ_n vs

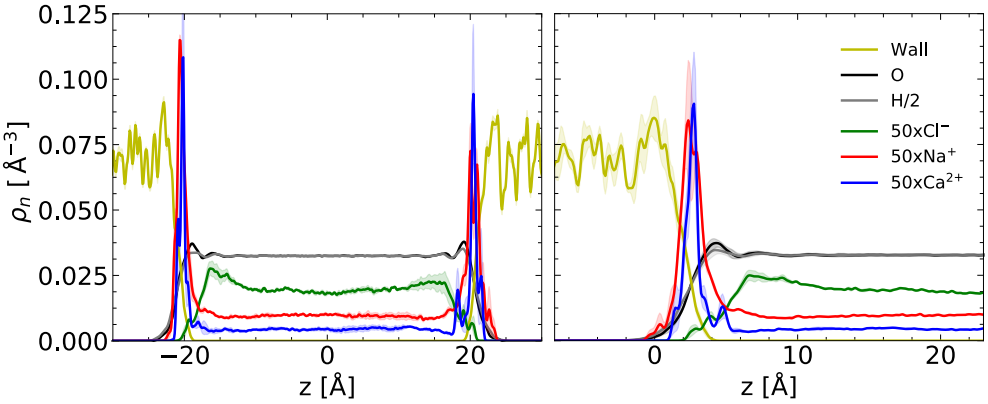

Figure 3.7: Unsymmetrized and symmetrized density profiles.

d do not require symmetrizing. The effect of symmetrization is shown in Fig. 3.7, where the new mean is given by

$$\rho_n = \frac{1}{2}(\rho_n(z<0) + \rho_n(z>0)) \tag{3.10}$$

and the uncertainty is obtained from

$$SE_{\rho_n} = \frac{1}{\sqrt{2}}\sqrt{\frac{1}{2}\left[(\rho_n(z<0) - \mu_{\rho_n}) + (\rho_n(z>0) - \mu_{\rho_n})\right]} + SE_{\rho_n(z<0)} + SE_{\rho_n(z>0)}. \tag{3.11}$$

3.3. Results

In this section, adsorption of ions in single and mixed electrolytes is evaluated. First, single electrolyte results are discussed, followed by a comparison with mixed systems. The section is concluded by evaluating ion-specificity of charged surface sites.

3.3.1. Single Electrolytes

Fig. 3.8a shows the symmetrized cation density (top) and anion density (bottom) near the charged silica surface as a function of z, the coordinate normal to the surface. A dense layer of Na^+ and Ca^{2+} is found near the surface, with most adsorbed ions forming CIPs (dashed lines). Ions forming CIPs plus those forming SSIPs make up the Stern layer, which here is found to have a thickness of approximately 8 Å, in line with experimental estimates, 6-10 Å [161]. CIPs are formed when water molecules in the first hydration shell of the ion are replaced by a surface atom (Si, O or H), and SSIPs are formed when this happens in the second hydration shell. The first and second hydration shells are commonly delimited by the first and second minima in the ion-water radial distribution function (rdf), see Fig. 3.9. The properties of the first hydration shell can be used to explain why Na^+ ions are found closer to the surface

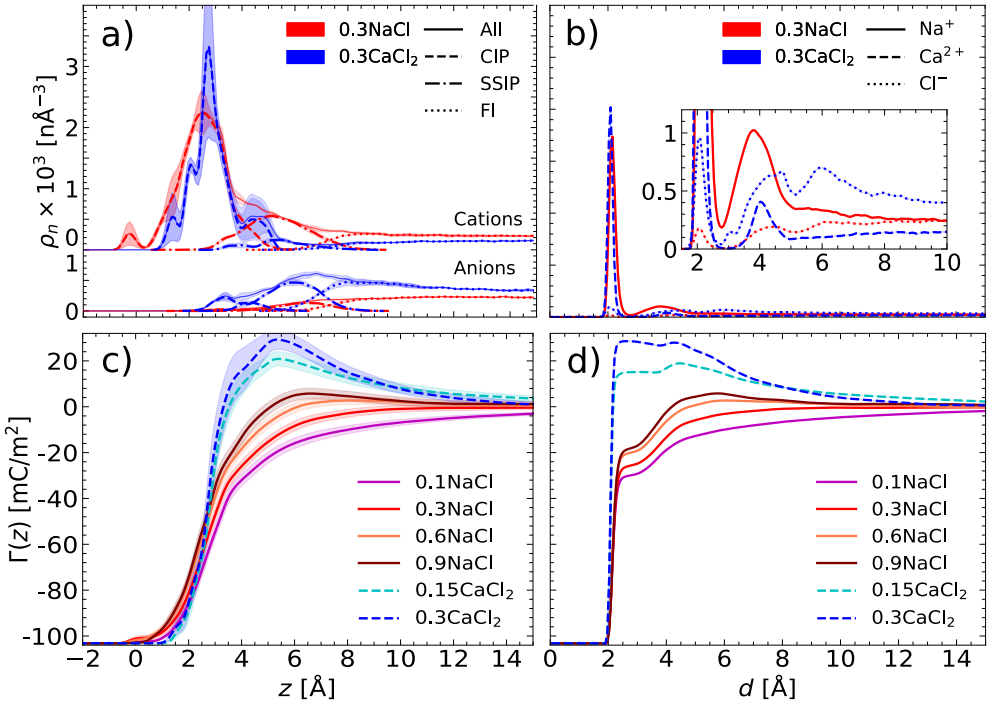

Figure 3.8: Number density profiles ((a) and (b)) and screening function ((c) and (d)) for single NaCl and $CaCl_2$ electrolytes as a function of z, normal to the surface ((a) and (c)), and d, distance to the nearest surface atom (Si, O or H) ((b) and (d)). The colors in subfigures (a) and (b) indicate the electrolyte solution; NaCl (red) or $CaCl_2$ (blue). The line type indicates the ion type; Na^+ (-), Ca^{2+} (- -), Cl^- (:). In subfigures (a) and (c), $z = 0$ is the average z-coordinate of all surface oxygen atoms. The shaded areas in all figures represent the uncertainty using 1 standard deviation (50 % confidence interval).

than Ca^{2+} ions. Let us consider the first maximum of the ion-water rdf to compute the ion hydration density ($H_2O/Å^2$). For TIP4P/2005, the maxima were found to be at 2.375 Å and 2.5 Å (see [53] and Fig. 3.9), giving a hydration density of 0.0846 $H_2O/Å^2$ and 0.102 $H_2O/Å^2$, with 6 and 8 water molecules in the first hydration shell, for Na^+ and Ca^{2+}, respectively. This indicates that Na^+ ions have a less tight hydration shell (e.g. fewer water molecules per hydration shell surface area) than Ca^{2+} ions. This allows water molecules to shift within the hydration shell of Na^+ ions, enabling these to move closer to the surface than Ca^{2+} ions [53]. Consequently, adsorbed Ca^{2+} ions display a larger change in coordination number, ΔCN, than adsorbed Na^+ ions, as discussed in more detail in Sec. 3.3.3.

The difference in distance from the surface for different ions is not accounted for in classical EDL theory. In theory, different ions would need to be assigned their own electrostatic planes [162], Inner Helmholtz Plane (IHP) and Outer Helmholtz Plane (OHP) (see Fig. 3.1), defined as passing through the centers of CIP and SSIP, respectively [163]. This however proves to be very elaborate for multicomponent systems. Furthermore, even a root-mean-squared (rms) surface roughness of 1.1 Å

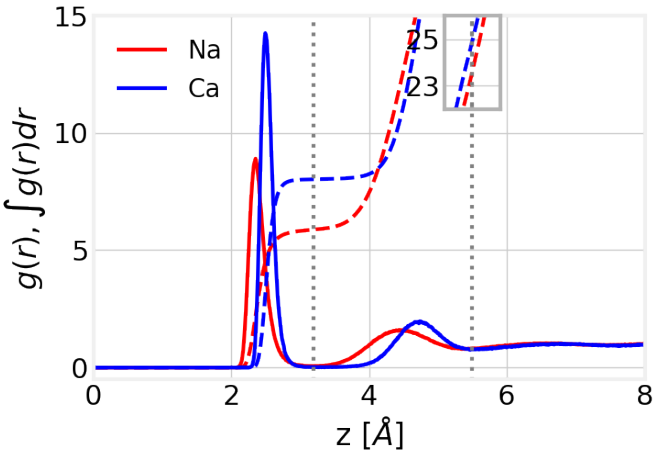

Figure 3.9: Rdf of ion-water for Na^+ and Ca^{2+} ions.

(experimentally reported values vary up to several nm [164]), obtained from the rms of the CIP z-position, can be shown to severely impact the suitability of EDL theory. In Fig. 3.8a, no distinct planes can be found for any of the ionic species. Instead, Fig. 3.8a shows overlapping regions in which CIP and SSIP co-exist. Density profiles as a function of z strongly depend on the surface roughness, causing the density profiles to be highly specific to the characteristics of the surface. This specificity is also responsible for the large error margins near the surface. Part of this specificity can be eliminated when considering the density as a function of the distance, d, to the nearest wall atom (Si, O or H). This measure provides an effective means to decouple the effect of surface roughness from ion specific properties such as adsorption state, which can more easily be identified in this way. Similarly, one could say that the density as a function of d closely resembles the density profile as it would occur on a perfectly smooth surface. Indeed the density profiles in Fig. 3.8b are found to closely resemble those found for smooth surfaces (see for example [165, 166]), and provide a clear distinction of atom layers corresponding to CIP and SSIP by the minima at $d \approx 3$ Å. Furthermore, this representation is in line with the classical definition of IHP and OHP for each ionic species, as passing through the centers of CIP and SSIP.

Different than in Fig. 3.8a, in Fig. 3.8b Na^+ ions and Ca^{2+} ions are found at similar distances from the surface. Additionally, the presence of Cl^- ions forming CIP is highlighted in this representation, in line with some experimental observations [167]. In the inset of Fig. 3.8b, a strict distinction of CIP and SSIP for Ca^{2+} ions is observed, whereas Na^+ ions are also found in an adsorption state that is neither strictly defined as CIP nor SSIP. This can be interpreted as Ca^{2+} ions having distinct preferred distances to form CIP and SSIP, suggesting a clear energy barrier between CIP and SSIP. On the other hand, Na^+ ions can also occupy adsorption states between CIP and SSIP, indicating a lower free energy barrier between these adsorption states.

Finally, the local excess of Cl^- ions immediately following the SSIP region in the $CaCl_2$ solution, indicates the occurrence of overscreening or Charge Inversion (CI), discussed in more detail below.

We define a screening function $\Gamma(\chi)$ to indicate the screening of the surface charge by the ions up to χ as the sum of bare surface charge σ_0 and the integral over the ion number density $\rho_{n,i}$ multiplied by the ion valency ν_i for ion type i and elementary charge e as [113]:

$$\Gamma(\chi) = \sigma_0 + \int_{\min(\chi)}^{\chi} \sum_i \rho_{n,i}(\chi')\nu_i e d\chi', \tag{3.12}$$

with χ being a placeholder for z or d. Note that $\Gamma(d)$ differs from a radial distribution function because only the distance to the nearest surface atom is considered for each ion. A surface is considered fully screened when the screening function approaches zero. Figs. 3.8c and (d) show Γ as a function of z (c) and d (d), obtained by applying equation 3.12 to the ion density profiles. As the ion concentration increases, the diffuse region becomes more compact, due to a shorter Debye length, such that fluid bulk properties are reached closer to the surface. This behavior has also been reported by others, based on streaming current measurements [140] and X-ray photoelectron spectroscopy or XPS [161]. For NaCl, the contributions of CIP ($d \leq 2.75$) and SSIP ($2.75 < d \leq 5.5$), both increase at increasing concentration, whilst for $CaCl_2$, only the CIP contribution increases. In fact, for NaCl we can find a linear trend of $0.03 \times \sigma_0$ increase in screening for each 0.3 M increase (see also Fig. 3.10). The screening function for the 0.9Na and both $CaCl_2$ systems exceeds zero, indicating overscreening or CI. This phenomenon occurs when an excess of counterions is attracted to the surface, changing the sign of Γ. For NaCl, CIP and SSIP appear to contribute equally to CI. On the other hand, for $CaCl_2$, CIP contribute in a greater extent to CI than SSIP.

Van der Heyden *et al.* [140] inferred the effective surface charge from streaming current measurements as $\sigma^* = \sigma_0 + \rho_{n_i,\text{Stern}}\nu_i e$, where the Stern layer is considered to be composed of immobile ions yielding $\sigma^* = \Gamma(d = d_{\text{Immobile}})$, with d_{Immobile} representing the distance from the surface up to where ions are considered immobile. The bare surface charge density of fused silica at pH $= 7.5$ was estimated as -150 mC/m^2, and the authors interpreted their measurements assuming no-slip Poiseuille flow and a Boltzmann charge distribution. Their result is included in Fig. 3.10, showing a sign reversal at 0.4 M $CaCl_2$. This method of determining CI only considers immobile ions, which are often considered to include the entire Stern layer, e.g. CIP and SSIP. Relative to the results of van der Heyden *et al.*, our MD results overpredict the occurrence of CI for $CaCl_2$. The effective surface charge estimated from electrokinetic experiments can deviate from what would be observed in MD, due to multiple factors: first, the simulation force field is not optimized for dynamic properties; second, the effective surface charge is inferred from streaming current measurements using multiple assumptions that may be inaccurate. Furthermore, the effect of fluidic transport on charge distribution is debated. Some authors [168, 169] have claimed that fluidic transport can alter the charge distribution, which would result in a non-linear elektrokinetic response. In contrast, our previous work [170] has shown linear

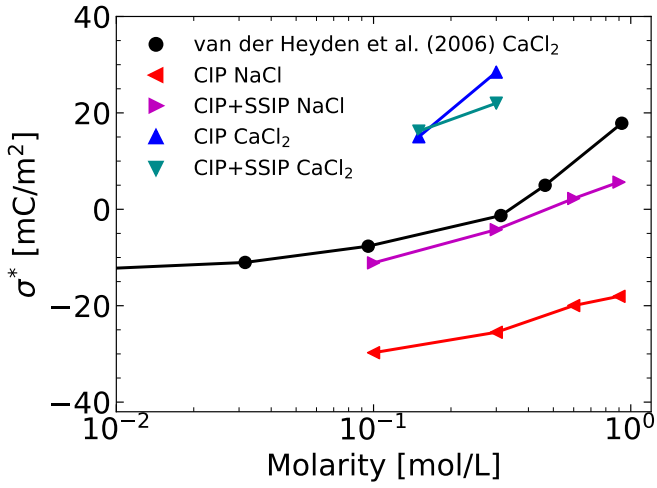

Figure 3.10: Effective surface charge σ^* for NaCl and $CaCl_2$ considering CIP and CIP plus SSIP. The lines are added as a guide for the eye.

elektrokinetic response in electroosmotic flow with electric fields up to 25×10^6 V/m (O(1-10^3) V/m is characteristic for electrokinetic experiments) [171, 172]. Consequently, the relationship between CI and electroosmotic flow reversal may not be unique.

In many numerical studies the formation of CI is underpredicted due to the use of uniformly charged model surfaces. These surfaces have been shown to predict less CIP formation, which is crucial for accurate predictions of CI [136, 143, 165, 173]. In fact, CI has been argued to be a discrete phenomenon which strongly depends on specific ion adsorption [143, 173]. For example, on a discretely charged wall, CI occurs locally when a higher valency ion or multiple monovalent ions adsorb to a single SiO^-. For monovalent ions this behavior has been observed in previous MD simulations [59], and is confirmed by our results.On the other hand, various numerical studies using discrete charges have overpredicted the occurrence of CI due to the force fields used [54, 128, 174, 175]. For example, the silica parametrization of clayFF [157, 158] contains neither bond nor angle parameters, requiring higher partial charges, which can lead to unphysically strong electrostatic interactions. Furthermore, we note that the Ca^{2+} parametrization used in this study has some known deficiencies [176], but no better parameters exist at the present time.

3.3.2. Mixed Electrolytes

By combining the ions from single 0.3Na with 0.15Ca or 0.3Ca systems in the mixed 0.3Na0.15Ca and 0.3Na0.3Ca systems (see Tab. 3.4), the total ionic concentration increases. This reduces the EDL thickness, in part due to a shorter Debye length. However, it is not obvious which ions would adsorb and how these distribute within the Stern layer. These matters will be investigated in the following.

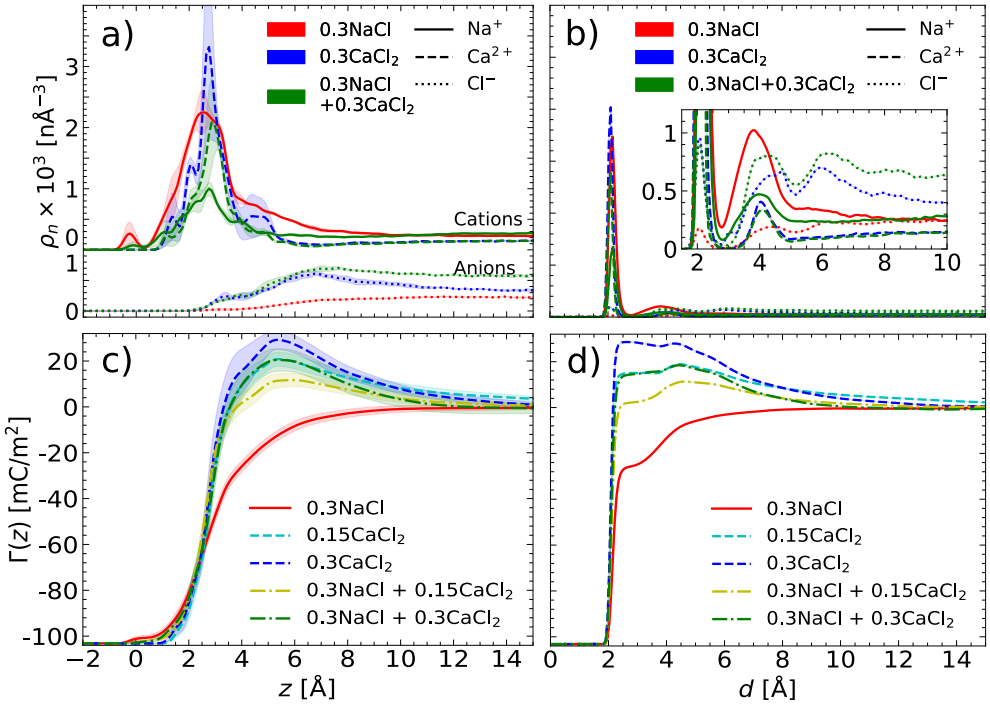

Figure 3.11: Number density profiles ((a) and (b)) and screening function ((c) and (d)) for single NaCl and $CaCl_2$ and mixed NaCl-$CaCl_2$ electrolytes as a function of z, normal to the surface ((a) and (c)), and d, distance to the nearest surface atom (Si, O or H) ((b) and (d)). In subfigures (a) and (b) the colors indicate the electrolyte solution; NaCl (red), $CaCl_2$ (blue) or NaCl + $CaCl_2$ (green). The line type indicates the ion type; Na^+ (-), Ca^{2+} (- -), Cl^- (:). In subfigures (a) and (c) $z = 0$ is the average location of all surface oxygen atoms. The shaded area in all figures represents the uncertainty using 1 standard deviation (50 % confidence interval).

Fig. 3.11 includes the density profiles and screening functions for the single 0.3Na, 0.3Ca, and the mixed 0.3Na0.3Ca systems. Fig. 3.11a shows how Na^+ adsorption (CIP+SSIP) in the mixture is reduced by more than 50 % compared to the single electrolyte solution, while Ca^{2+} adsorption is only reduced by 30 %. Stronger Coulombic attraction is expected for Ca^{2+} ions than for Na^+ ions, based on the higher partial charges of the former. Despite this, we find Na^+ ions adsorb closest to the surface. When the surface structure near a dangling oxygen provides a sterical hindrance to the hydrated ion, additional water molecules need to be expelled from, or shifted within, the first hydration shell of the ion. Since Na^+ ions have a less tight hydration shell than Ca^{2+} ions (see discussion above), these can shift water molecules around more easily than Ca^{2+} ions and hence adsorb with fewer water molecules being rejected from its hydration shell ions as shown in Fig. 3.13b. The results of this preferential adsorption are shown in the insets in Fig. 3.5. On the left, an adsorbed Na^+ ion is shown to penetrate the surface with part of its hydration shell, whilst on the right an adsorbed hydrated Ca^{2+} ion is shown to remain superficial. This preferential

adsorption behavior between Na^+ and Ca^{2+} leads to a reduction in CIP formation for Ca^{2+} in mixed compared to single electrolytes, as seen in Figs. 3.11a and (b). Consequently, also the CIP contribution towards surface screening is reduced from 129.3 mC/m^2 in the 0.3Ca system to 115.3 mC/m^2 in the 0.3Na0.3Ca system and from 123.9 mC/m^2 in the 0.15Ca system to 111.5 mC/m^2 in the 0.3Na0.15Ca system as shown in Fig. 3.11d. In terms of SSIP formation in Fig. 3.11b, a consistent reduction of Na^+ and Ca^{2+} ions is observed in the mixed systems compared to the single systems. Changes in Cl^- SSIP formation are not consistent across the mixed systems studied. Comparing the 0.15Ca to the 0.3Na0.15Ca system, an increase of Cl^- SSIP formation is found, while comparing the 0.3Ca to the 0.3Na0.3Ca system a decrease is observed. Nonetheless, the SSIP contribution is small compared to the CIP contribution towards the surface screening for the mixed and single $CaCl_2$ systems, resulting in a consistent reduction of overall surface screening and CI when adding monovalent ions to a divalent solution.

The above behavior of preferential adsorption and CI reduction is consistent with experiments which suggested reduction of multivalent ion adsorption upon addition of monovalent ions [140, 177–180]. For example, van der Heyden *et al.* [140] measured a reduction and even sign reversal of current in streaming current experiments for a multivalent ionic solution by addition of varying amounts of monovalent ions. This was interpreted as the result of competitive effects between ions in the Stern layer. In line with these experiments, we observe surface structure induced competitive effects in the formation CIP and SSIP.

3.3.3. Surface Induced Ion-Specificity

An additional simulation for the 0.3Na0.3Ca system was carried out as specified in the methods section (Sec. 3.2). Ions were repeatedly forced to desorb and subsequently equilibrated to adsorb, obtaining 11 uncorrelated sets of adsorbed ions. Averaging over these results, it was found that some dangling oxygens showed preferential adsorption of Ca^{2+} ions and others of Na^+ ions. Fig. 3.12 shows the preferential adsorption found for the left and right walls. The colorscale intensity goes from Ca^{2+} adsorbed in all 11 independent results (blue) to Na^+ adsorbed in all 11 independent results (red). The highest rates of preferential adsorption observed in our simulations were 64 % for Ca^{2+} (7/11) and 64 % for Na^+ (7/11). Roman numbers I-VI in Fig. 3.12 indicate regions that are specifically discussed below.

On the left channel wall in Fig. 3.12 it is seen that most dangling oxygens display a preference for Na^+ ions. On the right channel wall on the other hand, more preference for Ca^{2+} ions is seen. Single deprotonated silanols did not show consistent preferential adsorption. Clusters of 2 deprotonated silanols on the other hand, displayed preferential adsorption for Na^+ ions as shown in II-V and the cluster of 3 showed preferential adsorption of Ca^{2+} ions as shown in VI.

Upon visual inspection in VMD, it was found that dangling oxygens displaying preferential adsorption of Na^+ ions were frequently submerged into the surface. Furthermore, ions adsorbed to submerged dangling oxygens had a considerably reduced number of water molecules within the first hydration shell.Consequently, we argue

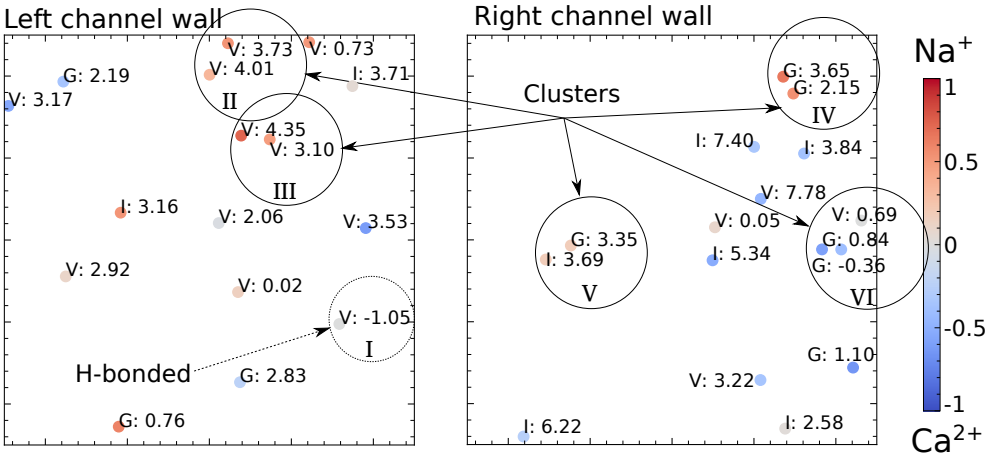

Figure 3.12: Preferential adsorption of Na^+ (red) and Ca^{2+} (blue) on dangling oxygens on the left and right surfaces of the channel. The letters indicate the type of silanol (i.e. Isolated, Vicinal and Geminal) and the number a protrusion metric times 100 given by equation 3.13. Regions I-VI are specifically discussed in the main text.

that steric hindrances to the ion hydration shell exist. This hypothesis was confirmed by introducing a protrusion metric (PM):

$$\mathrm{PM} = \frac{z_{\mathrm{sur}} - z_{O^-}}{z_{O^-}} \tag{3.13}$$

measuring the protrusion of dangling oxygens, as indicated in Fig. 3.4, as a function of their position z_{O^-} with respect to the average z-position of surrounding surface atoms $z_{sur} = 1/N \sum_k^N z$ within 4.6 Å. A high PM value indicates that a dangling oxygen protrudes from the surface whereas a low PM value indicates a submerged dangling oxygen. Attempts were made to include also the effect of silanol orientation, but failed to produce better results.

The PM is added to Fig. 3.12, showing that at low PM Na^+ is preferentially adsorbed and at high PM Ca^{2+} is preferentially adsorbed. Exceptions to this finding are indicated with roman numbers. Region I is found without any ion adsorbed due to hydrogen-bonds formed by these dangling oxygens with neighboring silanols. In cases II-VI on the other hand, multiple dangling oxygens were found next to each other forming clusters, with ions frequently adsorbed to several dangling oxygens simultaneously. Consequently, for these clusters a combined PM, would be indicative for ion-specificity. However, additional factors not included here, could play a role in the ion-specificity of clusters. Especially the following considerations are thought to be relevant: determination of which dangling oxygen is dominant, distance between dangling oxygens and electrostatic interactions. For example, clusters II, III, IV and V show similar average PM values, but clusters II, III and IV show strong preference for Na^+ ions while cluster V shows only a slight preference toward Na^+ ions. Furthermore, cluster VI displays preference for Ca^{2+} ions despite having a low combined PM

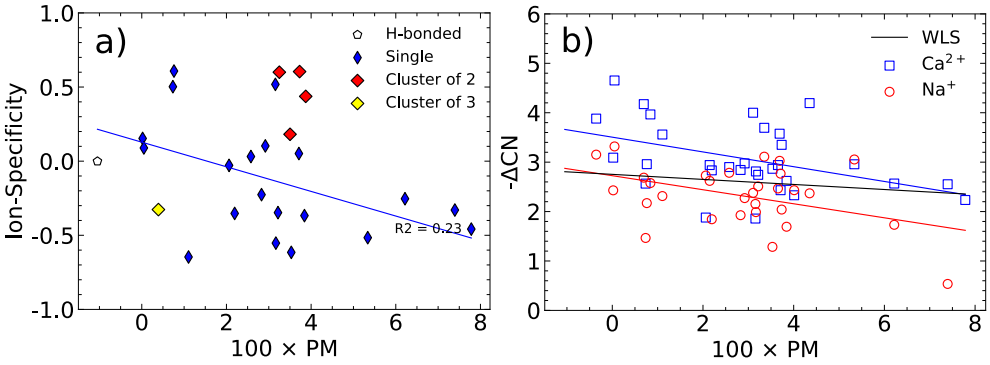

Figure 3.13: Ion-specificity (a) and reduction in coordination number (b) as a function of PM. Ion-specificity goes from Ca^{2+} preferential adsorption (-1) to Na^{+} preferential adsorption (1). Least squares regression are shown to highlight trends for single dangling oxygens (blue) in (a) and $-\Delta CN$ for Na^{+} (red) and Ca^{2+} (blue) ions in (b). Weighted Least Squares (WLS) in (b) shows the trend of $-\Delta CN$ for all ions combined, weighted by the ion-specificity.

value of 0.39/100. In conclusion, for deprotonated silanol clusters the ion-specificity cannot be explained using only geometric features.

Fig. 3.13 shows that the remaining dangling oxygens (excluding those within I-VI) follow the trend expected by the PM. In Fig. 3.13a, deprotonated silanols that have no other dangling oxygen nearby (henceforth named *single*) are displayed in blue and those forming clusters (II-VI in Fig. 3.12) in red and yellow. Clusters are shown separately because a different trend is expected for clusters of dangling oxygens as compared to single dangling oxygens due to the neglecting of electrostatic contributions by the PM. Preferential Na^{+} adsorption is observed at low PM and preferential Ca^{2+} adsorption at large PM. A least square regression for single dangling oxygens is shown in blue, showing a clear trend despite the large spread. At increasing PM, preferential adsorption shifts from Na^{+} to Ca^{2+}. For clusters of dangling oxygens, no solid conclusions can be drawn due to the fact that only 5 data points exist and the results are not consistent with the PM. For single dangling oxygens however a clear trend is observed despite the large spread. At increasing PM, preferential adsorption shifts from Na^{+} to Ca^{2+}.

We suggest the trend observed in Fig. 3.13a is related to the number of water molecules within the first hydration shell of adsorbed ions. In fact, in Fig. 3.13b it is observed that the number of water molecules expelled from the first hydration shell of adsorbed ions increases at reducing PM. We argue this to be due to steric hindrances to the first hydration shell of the ion by the structure surrounding a dangling oxygen. This hindrance can be overcome by either expelling additional water molecules from the first hydration shell, or shifting water molecules within the hydration shell. From Fig. 3.13b it is seen that consistently more water molecules are expelled from the first hydration shell of Ca^{2+} ions than from that of a Na^{+} ions. Since, Na^{+} ions have been found to have a less tight hydration shell, these preferentially adsorb at submerged dangling oxygens by shifting water molecules within their hydration shell.

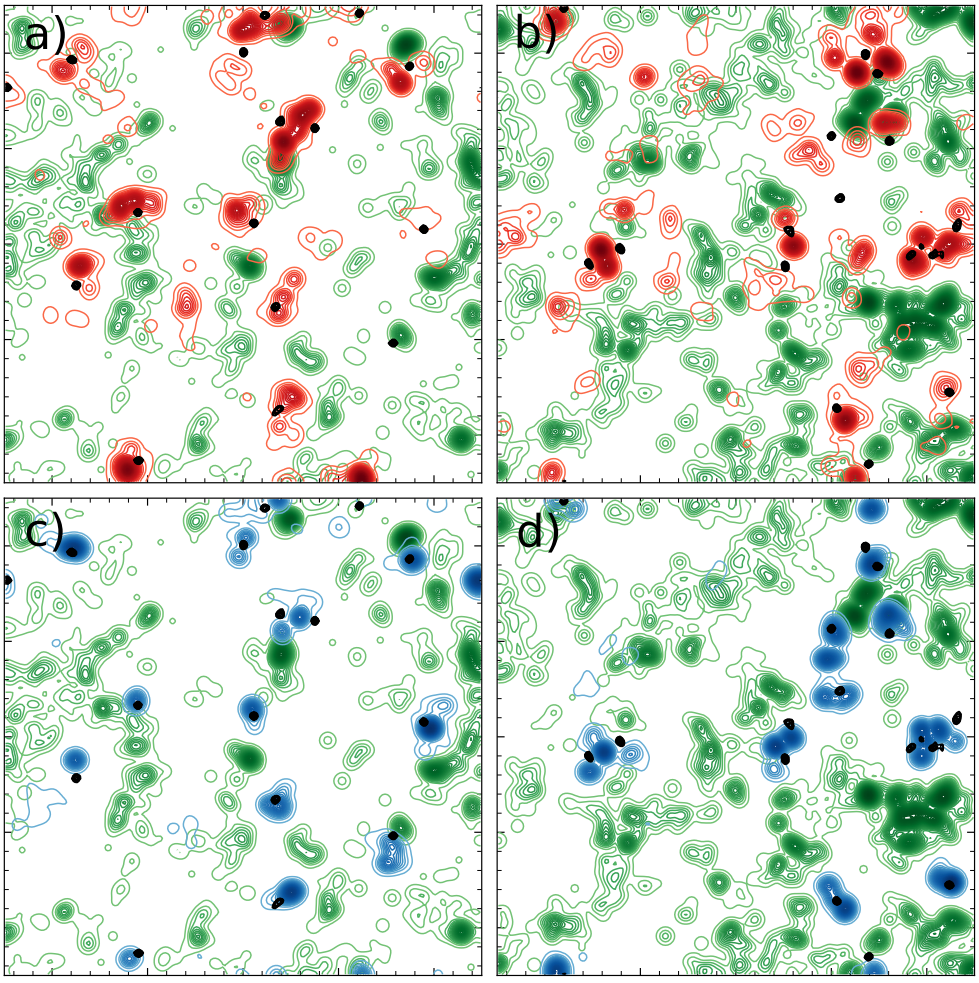

Figure 3.14: Average adsorption location of Na^+ (red in (a) and (b)) and Ca^{2+} (blue in (c) and (d)) on the left ((a) and (c)) and right ((b) and (d)) walls from single species 0.3Na and 0.3Ca systems. Average Cl^- adsorption location is given in green.

Additionally, it was found that the adsorption location of Na^+ ions and Ca^{2+} ions on the same dangling oxygen differs. Na^+ ions are frequently found next to a dangling oxygen, forming an additional bond with another surface atom or rotating around it, whilst Ca^{2+} ions are almost exclusively found on top of dangling oxygens (see Fig. 3.14). This difference in adsorption location can potentially have a large influence on Stern layer dynamics, as adsorbed Na^+ may contribute differently to electroosmotic or pressure driven flow than adsorbed Ca^{2+} ions. In conclusion, a combination of surface structure induced ion-specificity and electrostatic attraction, which vary locally over the surface, are ultimately responsible for selectivity.

3.4. Conclusions

We have presented a study of ion adsorption, comparing single and mixed electrolytes confined by charged amorphous silica. Ion layering in the Stern layer was evaluated by classifying ions as forming surface CIP and SSIP based on their distance to a given adsorption site. Taking this idea one step further, density profiles were computed for each ionic species as a function of distance to the nearest surface atom, thereby effectively eliminating surface specific roughness effects and obtaining density profiles in line with classical EDL theory. This approach can potentially be used together with EDL models such as the Gouy-Chapman-Stern-Grahame model to improve predictions of the surface or shear plane potentials.

Analyzing CIP formation per dangling oxygen, we found surface structure induced ion-specificity. Although Ca^{2+} ions undergo stronger Coulombic attraction to the negatively charged surface than Na^{+} ions, the microstructure of certain adsorption sites may exhibit preference toward Na^{+} adsorption by impeding Ca^{2+} ions, which have a tighter hydration shell, from adsorbing. Using this insight, we suggested a simple protrusion metric to predict ion-specificity of dangling oxygens. This metric was shown to work on single dangling oxygens, but failed when multiple dangling oxygens were found close to each other forming clusters. Additional analysis is needed to expand the understanding of the underlying mechanism of this ion-specificity and test the applicability of the protrusion metric with other electrolytes and oxide surfaces. We expect this metric to be especially successful in mixed electrolytes containing counterions of the same valency but dissimilar hydration properties.

In conclusion, surface roughness as well as placement of deprotonated silanols have a severe impact on preferential adsorption, related to sterical hindrances for ion hydration shells. This finding can be used to microengineer surfaces with selectivities for specific ions for purposes ranging from water desalination to osmotic power harvesting. Furthermore, insight into the relation between surface structure and preferential adsorption can help understand experimental results.

4

Bridging the Gap between MD Simulations and Experiments

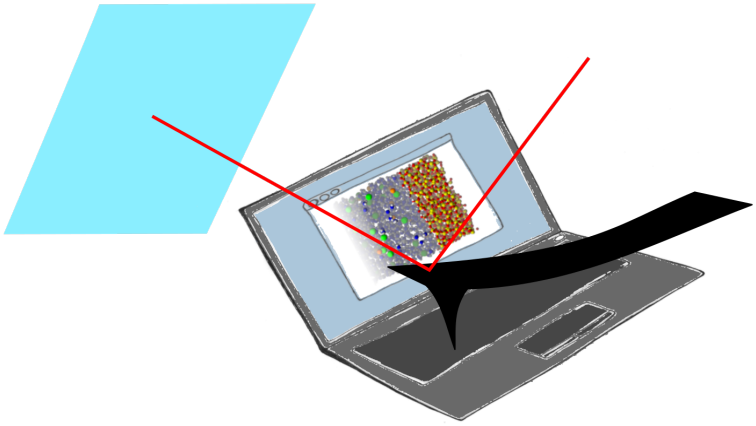

This chapter is based on the paper:

M. F. Döpke and R. Hartkamp, *The importance of specifically adsorbed ions for electrokinetic phenomena: Bridging the gap between experiments and MD simulations*, J. Chem. Phys, **154**, 094701 (2021).

4.1. Introduction

An oxide in contact with an aqueous solution adopts a bare surface charge density that is balanced by ions forming a Stern and diffuse layer near the solid-liquid interface. This so-called Electric Double Layer (EDL) plays an important role in geology [181], materials science [182], biology [183] and electrochemistry [184]. It controls for example the capacitance in batteries, colloidal stability [3], dissolution of materials, and can be used for ion sensing [59]. Detailed understanding of the EDL and its dependence on the solid material, solution composition and pH is thus invaluable. However, no single experimental technique can measure its entire structure and dynamics. Instead, partial pieces of the puzzle can be gleaned from a variety of different techniques. Potentiometric titration [25] can be used to measure the bare surface charge density, while the effective surface charge density can be inferred through force measurements [185] or electrokinetics [140]. Electrokinetic techniques can also provide information about the mobility of ions within the EDL, and spectroscopic techniques [186–188] can be used to infer information about the interfacial ion and water distribution and orientation. Ideally, a comprehensive picture of the EDL for a given solid-liquid interface could be constructed by combining multiple techniques in a single device to exclude the possibility of differences in material sample or experimental conditions. Although some techniques have indeed been integrated together [189, 190], this is a very difficult task and not all techniques can be carried out under the same conditions and set-ups. For instance, force measurements require access to the substrate, while some electrokinetic techniques require closed channels.

Another fundamental challenge of acquiring detailed understanding of the EDL from a combination of experimental techniques is their dependence on models to interpret measurements [191, 192]. Consequently, an inferred charge, potential or other EDL property is inherently biased by the assumptions and parameters used in the model, with the accuracy of models depending also on the experimental conditions. For example, the Helmholtz-Smoluchowski theory is known to become inaccurate for small colloidal particles and at low ion concentrations, where the effects of surface conductance compared to the bulk conductance are large [6, 193]. On the other hand, the widely used Gouy-Chapman model is known to break down under conditions of strong electrostatic coupling. The consequences of modeling inaccuracies show for example from discrepancies between ζ-potentials obtained via multiple approaches [27, 28, 194].

The standard approaches that are used to interpret experiments are especially put to the test when dealing with high ion concentrations and multivalent electrolytes. An interesting phenomenon that can occur under such conditions is the reversal of the sign of the diffuse layer charge. This reversal is known as charge inversion. Experimentally, the diffuse layer charge can be inferred through for example electrokinetic techniques [140], force measurements [185] or non-linear optics [195, 196], but the results between these methods differ from each other. In electrokinetics for instance, an assumption on the ion density profiles in the diffuse layer is required, while in force measurements the tip itself may influence this very profile, and in non-linear optics the interpretation and relation between the measured quantities and EDL structure remains challenging. Even between different electrokinetic tech-

niques, such as Streaming Currents (SC), streaming potentials, electro-acoustics or ElectroOsmotic Flow (EOF), results may differ [27, 28, 194]. To better understand charge inversion, and more generally the EDL structure and dynamics under these conditions, a high-resolution model-free approach is needed.

Having access to all atomic positions, velocities, forces and energies, Molecular Dynamics (MD) simulations have the unique potential to provide a high-resolution and model-free comprehensive three-dimensional picture of the EDL structure and dynamics [1]. However, this requires confidence that the description of atomic interactions, which is the key required input to the simulations, does in fact produce the correct behavior. MD studies of solid-liquid interfaces have shown a diverse picture, with ion adsorption varying largely between studies [23, 54, 127–131, 134, 135, 170, 175, 197]. For example, Lorenz *et al.* [128] predicted charge inversion in silica nanochannels with a bare surface charge density of -144 mC/m^2 filled with 200 mmol/L $CaCl_2$, while Biriukov *et al.* [197] predicted no charge inversion under similar conditions. In fact, many MD simulation studies predict charge inversion at bulk ion concentrations much lower than inferred from experiments [23, 127, 128]. One important cause of the deviations between ion adsorption in different MD simulation studies and their deviation from experiments is the fact that the Lennard-Jones cross interactions required to describe solid-liquid interactions are typically not part of the force field optimization. With a few exceptions [198], these are rather estimated based on common combination rules. Rigorous optimization of these parameters would require unambiguous and detailed target data on the interfacial distribution and adsorption of ions onto the surface, which is not directly measurable. Another cause of the deviations is the use of full charges. These do not take into account the dielectric screening of the medium, and frequently result in an over-prediction of ion-adsorption [198, 199] and ion-pairing [22, 70]. In an attempt to account for this screening, the Electronic Continuum Correction (ECC) theory states that the charges should be scaled by a factor between 0.75 and 0.85 [70]. While strictly speaking this charge scaling is only valid in homogeneous systems with a constant dielectric [200], its use in interfacial systems with a variable dielectric has shown very promising improvements in the solid-liquid interactions [197, 199].

In this study, we propose a scaling of the Lennard-Jones cross interactions as a free variable combined with the use of ECC to achieve good agreement between nonequilibrium MD simulations and electrokinetic experiments. Specifically, we tune the solid-ion Lennard-Jones cross interactions to match the concentration at which $\zeta = 0$ for both, electrokinetic experiments and electrokinetic simulations. At this concentration, the measured properties (i.e., electrical current or flow velocity) tend to zero, resulting in $\zeta = 0$ via the Helmholtz-Smoluchowski theory regardless of fluid properties such as viscosity. Thereby, providing a concentration which is least susceptible to interpretation. We examine the proposed approach in a fused silica slit pore filled with a $CaCl_2$ electrolyte at pH 7.5. The reason we choose this system is twofold: first, experimental SC data are available [140], including a concentration at which $\zeta = 0$, and second it is a relevant system for natural processes and industrial applications [201]. We find that the number of specifically adsorbed ions is the key property to determine the experimental concentration at which $\zeta = 0$. Once the sim-

ulations are tuned and validated, we provide detailed insight into the EDL structure and dynamics, which can be used for future improvements of surface complexation and continuum models.

The remainder of the chapter is organized as follows: The theoretical framework and MD simulation set-up are presented in Sec. 4.2. The results are discussed in Sec. 4.3. Finally the conclusions are provided in Sec. 4.4.

4.2. Methods

4.2.1. Theoretical Framework

Here we lay out the most common theoretical framework to calculate the ζ-potential through either SC or EOF experiments shown in Fig. 4.1 and described in more detail in [6].

Streaming Current Experiments

A typical SC experiment is displayed in the bottom part of Fig. 4.1. A pressure gradient $\Delta p_x/L$ is applied, resulting in a planar Poiseuille flow profile $u_x(z)$ (parabolic flow profile). A charge density imbalance $\rho_e(z)$ in the diffuse layer of the EDL causes a measurable electric current I_{str}. If the bare surface is negatively charged, an excess of cations is expected in the mobile part of the EDL, resulting in a positive I_{str}. In the event of charge inversion however, the immobile part of the EDL overcompensates the bare surface charge density, resulting in an excess of mobile anions in the EDL, reversing the sign of I_{str}.

In order to determine the ζ-potential, let us relate I_{str} to $\rho_e(z)$ and $u_x(z)$ in a duct of width w, height $2h$ ($-h$ to h) and length L via

$$I_{\text{str}} = 2w \int_0^h \rho_e(z) u_x(z) dz, \tag{4.1}$$

with $\rho_e(z)$ being described by the Poisson equation

$$\varepsilon_0 \varepsilon_r \frac{d^2\psi(z)}{dz^2} = -\rho_e(z) \tag{4.2}$$

assuming a constant dielectric permittivity ε_r, and $u_x(z)$ being given by the planar Poiseuille flow solution

$$u_x(z) = \frac{\Delta p_x}{2\eta L}\left(h^2 - z^2\right) \tag{4.3}$$

assuming a constant viscosity η. ε_0 and ψ are the vacuum permittivity and electrostatic potential, respectively. Inserting Eqs. (4.2) and (4.3) into (4.1), twice integrating by parts, applying boundary conditions $\psi(z_{\text{no-slip}}) = \zeta$ and $\psi(z_{\text{bulk}}) = 0$, and rearranging for ζ yields[1] [202]

$$\zeta = -\frac{\eta}{\varepsilon_0 \varepsilon_r 2wh} \frac{L}{\Delta p_x} I_{\text{str}}. \tag{4.4}$$

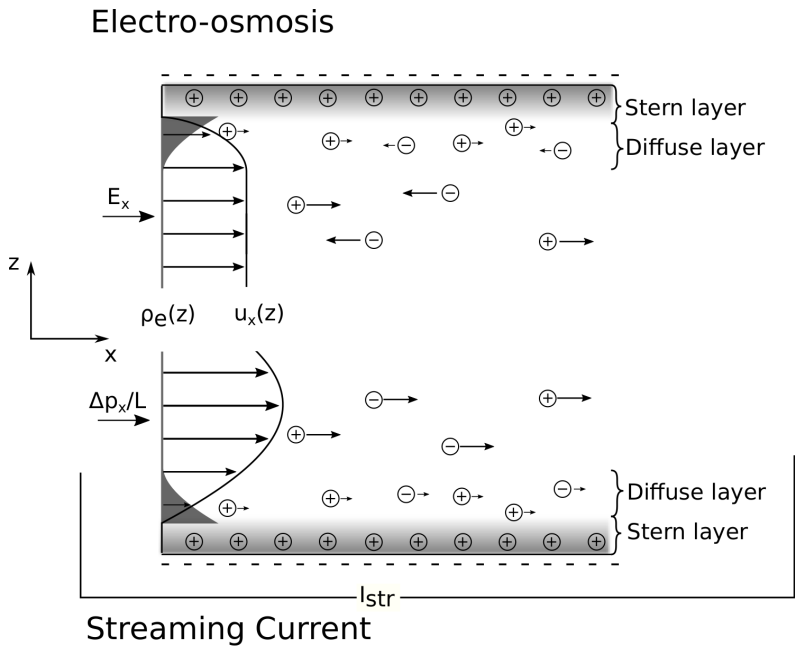

Figure 4.1: Schematic of an ElectroOsmotic Flow (EOF) experiment (top) and a Streaming Current (SC) experiment (bottom).

[1]Insert Eq. (4.2) into Eq. (4.1) and integrate twice by parts:

$$\begin{aligned} I_{\text{str}} &= -\varepsilon_0\varepsilon_r 2w\int_0^h \frac{d^2\psi(z)}{dz^2}u(z)dz \\ &= -\varepsilon_0\varepsilon_r 2w\left(\left[u(z)\frac{d\psi(z)}{dz}\right]_0^h - \int_0^h \frac{d\psi(z)}{dz}\frac{du(z)}{dz}dz\right) \\ &= -\varepsilon_0\varepsilon_r 2w\left(\left[u(z)\frac{d\psi(z)}{dz} - \frac{du(z)}{dz}\psi(z)\right]_0^h + \int_0^h \psi(z)\frac{d^2u(z)}{dz^2}dz\right). \end{aligned}$$

Insert Eq. (4.3) and its derivatives $\frac{du(z)}{dz} = -\frac{\Delta pz}{\eta L}$ and $\frac{d^2u(z)}{dz^2} = -\frac{\Delta p}{\eta L}$ into (4.1), resolve the boundary conditions $\psi(z_{\text{no-slip}}) = \zeta$ and $\psi(z_{\text{bulk}}) = 0$, and consider $\int_0^h \psi(z)dz$ to be very small in a wide channel

$$\begin{aligned} I_{\text{str}} &= -\varepsilon_0\varepsilon_r 2w\left(\left[\frac{\Delta p}{2\eta L}\left(h^2 - z^2\right)\frac{d\psi(z)}{dz} + \frac{\Delta pz}{\eta L}\psi(z)\right]_0^h - \frac{\Delta p}{\eta L}\underbrace{\int_0^h \psi(z)dz}_{\approx 0}\right) \\ &= -\varepsilon_0\varepsilon_r 2w\left[\left(\frac{\Delta p}{2\eta L}\left(h^2 - h^2\right)\frac{d\psi(h)}{dz} + \frac{\Delta pz}{\eta L}\cancel{\psi(h)}\right)^{\zeta} - \left(\frac{\Delta p}{2\eta L}\left(h^2 - 0^2\right)\cancel{\frac{d\psi(0)}{dz}}^{0} + \frac{\Delta p0}{\eta L}\psi(0)\right)\right] \\ &= -\varepsilon_0\varepsilon_r 2wh\frac{\Delta p}{\eta L}\zeta \end{aligned}$$

Electroosmotic Flow Experiments

The top part of Fig. 4.1 displays a typical EOF experiment. An external electric field E_x is applied parallel to the walls, accelerating cations in the direction of the electric field and anions in the opposite direction. Water molecules are dragged along due to viscous forces. The competing effects of cations and anions on the overall flow is balanced in the electroneutral ($\rho_e(z) = 0$) bulk region of the channel. This neutrality does not apply near the surface, where an excess of mobile cations or mobile anions accelerates the fluid along or against the electric field, respectively. This results in a plug flow $u_x(z)$, as shown in the top of Fig. 4.1, governed by the 1D Navier-Stokes momentum equation

$$\eta \frac{d^2 u_x(z)}{dz^2} = -\rho_e(z) E_x \tag{4.5}$$

with boundary conditions $u_x(z_{\text{no-slip}}) = 0$ and $u_x(z_{\text{bulk}}) = u_{x,\text{bulk}}$. Combining this relation with the 1D Poisson equation given in Eq. (4.2), with the boundary conditions $\psi(z_{\text{no-slip}}) = \zeta$ and $\psi(z_{\text{bulk}}) = 0$, an expression for the velocity profile is obtained

$$u_x(z) = \frac{\varepsilon_0 \varepsilon_r E_x}{\eta} \left(\psi(z) - \zeta\right). \tag{4.6}$$

For the velocity in the bulk, this equation reduces to the Helmholtz-Smoluchowski equation

$$\zeta = -\frac{\eta u_{x,\text{bulk}}}{\varepsilon_0 \varepsilon_r E_x}, \tag{4.7}$$

relating the measurable bulk velocity $u_{x,\text{bulk}}$ to the ζ-potential.

Similarity Between SC and EOF Experiments

Considering that SC and EOF experiments are both performed within the linear response regime, the no-slip plane (separation between Stern layer and diffuse layer in Fig. 4.1) and adsorption of ions is independent of flow. Consequently, $\rho_e(z)$, $\psi(z)$ and the ζ-potential should also be identical in both, SC and EOF experiments. Despite this, results have deviated between electrokinetic techniques [27, 28, 194]. One exception being the combinations of concentration and pH at which $\zeta = 0$, which are rather uniformly predicted. When observing Eqs. (4.4) and (4.7) this is also not surprising, since when $I_{\text{str}} \to 0$ or $u_{x,\text{bulk}} \to 0$ the dependence of $\zeta \to 0$ on properties such as the viscosity, dielectric or duct size and shape vanishes. Therefore, the fact that differences arise between finite ζ-potential values predicted from these methods is thought to be for example due to the use of a planar Poiseuille flow solution (Eq. (4.3)). Other possible sources of error are the assumption of constant dielectric permittivity or viscosity, measurement noise, the use of differing theoretical models, differences in the treatments of the individual substrates, and contaminants. Furthermore, some authors have also suggested that the surface properties may be affected by the flow [168, 203].

4.2.2. Molecular Dynamics Simulations

We perform non-equilibrium MD simulations of $CaCl_2$ electrolytes in an amorphous silica slit pore. The amorphous silica and channel are generated following the ap-

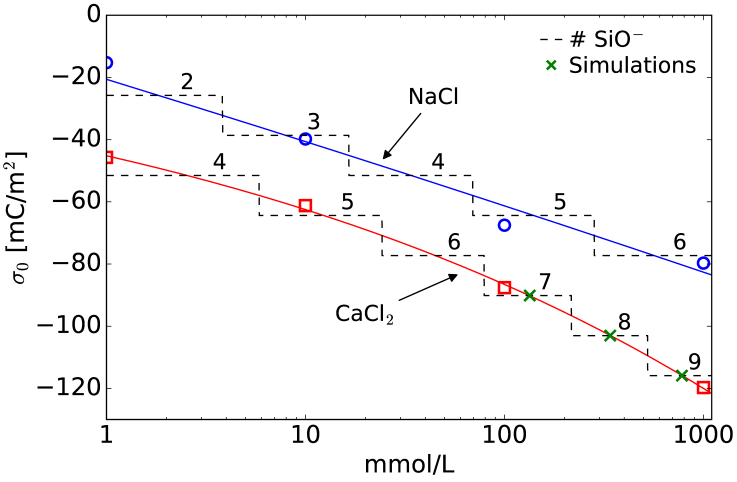

Figure 4.2: Experimental results of bare surface charge density σ_0 against bulk ion concentration c_0 from surface charge titration experiments on ground quartz [204] (1, 10 and 100 mM) and amorphous silica [205] (1000 mM) at constant pH of 7.5. NaCl is provided as a reference. The full lines are a power law fit of the experimental data points and the dashed lines represent the number of SiO^- per surface that would correspond to the respective bare surface charge density with our system.

proach described in Sec. 3.2 of Ch. 3. In short, a block of amorphous silica is prepared by annealing and quenching a β-cristobalite. The block is subsequently cut in the middle, creating 2 opposing surfaces with dangling oxygens. The dangling oxygens are protonated and the silanol (SiOH) density is adjusted to approx 5 SiOH/nm^2 by bridging some of the nearby SiOH groups. Finally, TIP4P/2005 water molecules [16] and Madrid-2019 ions [22] are added between the slabs and the surface charge density is adjusted by deprotonating a given number of silanol sites corresponding to a pH of approximately 7.5.

As seen from potentiometric titration data [204, 205] in Fig. 4.2, maintaining a constant surface charge density across a bulk ion concentration range or when comparing different ionic compounds does not represent the experimentally relevant scenario in which pH is kept constant. Yet, such a constant surface charge is standard practice in MD simulation studies. Alternatively, in order to indirectly account for a constant pH, we vary the bare surface charge density σ_0 together with the bulk ion concentration c_0. Since the surface charge density of amorphous silica is governed by discretely deprotonated SiOH (SiO^-) groups, not every bare surface charge density is possible in our system with either wall having a surface area of approximately 12 nm^2. The black dashed line in Fig. 4.2 displays the possible bare surface charge densities in our system by deprotonating a discrete number of SiOH on each surface. The green crosses mark the simulation conditions that are studied here. Within the simulation, the net charge of each SiO^- group is scaled down by a factor 0.85 in order to be consistent with the charge scaling of the Madrid-2019 force field. We

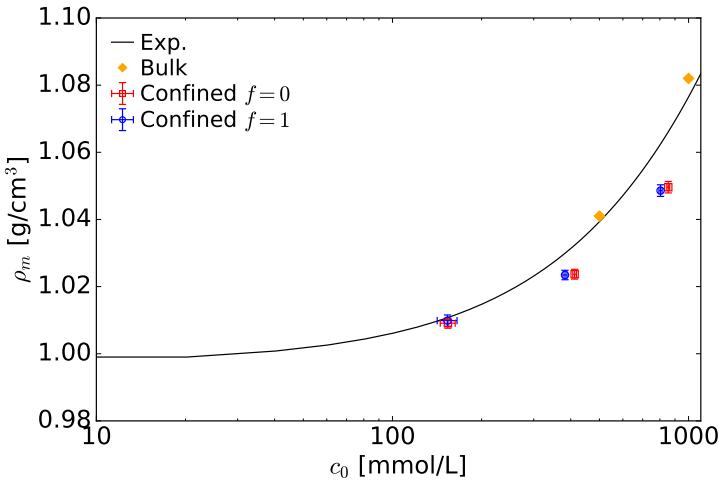

Figure 4.3: Final density and molarity of the studied systems compared to non-confined bulk simulations [22] and experimental results [207, 208].

remark that this is a purely computational consideration and full charges are used during post processing with the exception of streaming velocities which are scaled up by a factor of 1/0.85. This scaling of the streaming velocity is necessary since the scaling down of ionic charges by 0.85 is equivalent to an ion with the nominal charge experiencing a reduced electric field $E_{x,\text{eff}} = 0.85E_x$ [197].

The density of the fluid is adjusted by pushing the walls towards each other with a force equivalent to 1 bar nominal pressure for 20 ns. The resulting bulk densities and concentrations calculated from a subsection in the center of the channel are shown in Fig. 4.3. Subsequently, the position of the walls is fixed in space and an electric field of $E_x = 0.2$ V/nm is applied to the fluid. Such a large electric field is necessary in MD simulations to increase the signal to noise ratio (Fig. 4.4a) shows that the resulting flow is still within the linear response regime) [54, 166, 170, 206]. Note that simulating EOF is preferred over SC for our purpose since the relation between the streaming current and the ζ-potential depends on the channel height (Eq. (4.4)), which is not uniquely defined for atomistic surfaces with a finite roughness. This ambiguity affects MD simulations of SC much more than experiments because of the typically much smaller channel heights in MD simulations. On the other hand, EOF simulations are unaffected by this ambiguity.

The temperature is maintained by connecting the walls to a thermal heat bath at 298 K via a Nosé-Hoover thermostat. This is shown to yield a fluid temperature of around 295 K in Fig. 4.4b). Simulations with an externally applied electric field are equilibrated for 20 ns followed by production runs of 100 ns at a time step of 2 fs. Two independent simulations with different amorphous surfaces and starting conditions are performed for all configurations. All simulations are performed with LAMMPS [80] using a cut off of 12 Å and the particle-particle particle-mesh long-

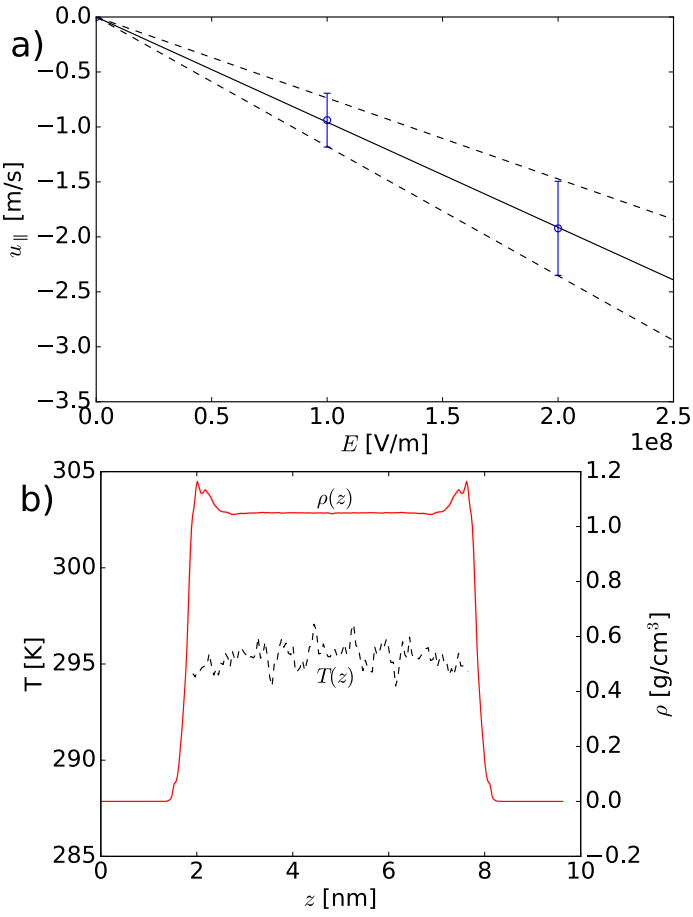

Figure 4.4: a) Linear response regime of the EOF. b) Temperature of the fluid when an electric field of 0.2 V/nm is applied. The mass density profile is provided as a reference. The coordinate z is with respect to the box dimensions.

Table 4.1: Channel system configurations. c_0 is the bulk $CaCl_2$ concentration, A_s the surface area, $2h$ the channel height (approximate separation between the surfaces), and # denotes the number of SiO^- per surface, H_2O molecules, Ca^{2+} ions and Cl^- ions.

c_0 [mmol/L]	A_s [nm^2]	$2h$ [nm]	# SiO^-	# H_2O	# Ca^{2+}	# Cl^-
150	12	14	7	5733	22	30
380	12	6	8	2457	24	32
800	12	6	9	2457	44	70

range electrostatic solver [209] with a precision of 1e-4. OH bonds of water and silanols, and HOH angles of water are constrained using the SHAKE algorithm [160] with a precision of 1e-4. Periodic boundary conditions are used in x and y. In z, a vacuum of 3 times the box length is introduced beyond to remove dipole inter-slab interactions [156]. The final systems are described in Tab. 4.1. The channel heights $2h$ are chosen in order to avoid EDL overlap.

Cross interactions within each force field (IFF and Madrid-2019 including TIP4P/2005) are applied as recommended by the respective authors. Between the force fields however, this leaves open the question of what combination rule to use. Between TIP4P/2005 and IFF we use the Lorentz Berthelot [210] (LB) combination rule (see Eq. (1.7)). However, since the Madrid-2019 $Ca^{2+}-O_{water}$ and $Cl^{-}-O_{water}$ Lennard-Jones cross interactions are specifically defined, we investigate various Lennard-Jones cross interactions between the Madrid-2019 ions and IFF oxygen atoms following the scaling

$$A_{X-O_{IFF}} = A^{LB}_{X-O_{IFF}} \left[\left(\frac{A_{X-O_{water}}}{A^{LB}_{X-O_{water}}} - 1 \right) f + 1 \right] \tag{4.8}$$

with $A \in \{\sigma, \epsilon\}$ and $X \in \left\{Ca^{2+}, Cl^{-}\right\}$. The scaling is applied simultaneously to σ and ϵ and to both Ca^{2+} and Cl^{-} ions.

4.3. Results

In this section we show first the impact of scaling the solid-liquid interactions on the ion distribution within the EDL, followed by a comparison with experiments and discussion relating the EDL structure to the observed EOF. Finally, the mobility within the EDL is assessed. The uncertainty quantification and symmetrizing of results is performed as detailed in Sec. 3.2.

4.3.1. Scaling Solid-Liquid Interactions

The bare surface charge density of amorphous silica at a given pH and concentration is screened by ions. We distinguish for each ion between 4 different adsorption types, namely: Inner-Sphere Surface-Complexes (ISSC), Outer-Sphere Surface-Complexes (OSSC), ions within the diffuse layer and free ions, as shown in Fig. 4.5a. ISSC and OSSC are ions for which a surface atom (Si, O, H) is part of their first or second hydration shell, respectively. Ions within the diffuse layer are defined as having their first 2 hydration shells intact, but remaining within 12 Å of the surface (defined as the distance between nuclei of ions and nuclei of the nearest surface atom) [23]. Note that the 12 Å length is chosen rather arbitrarily to represent the real diffuse layer approximately. Free ions are those which are further than 12 Å from the surface. Varying the scaling parameter f in Eq. (4.8) we can control the number of Ca^{2+} ions forming ISSC. Fig. 4.5b, shows an increase in ISSC formation with a change from $f = 0$ to $f = 1$. As a direct consequence, the formation of OSSC and the number of Ca^{2+} ions in the diffuse layer are reduced. On the other hand, in Fig. 4.5c for Cl^{-}, the number of ions forming ISSC, OSSC and number of ions within the diffuse

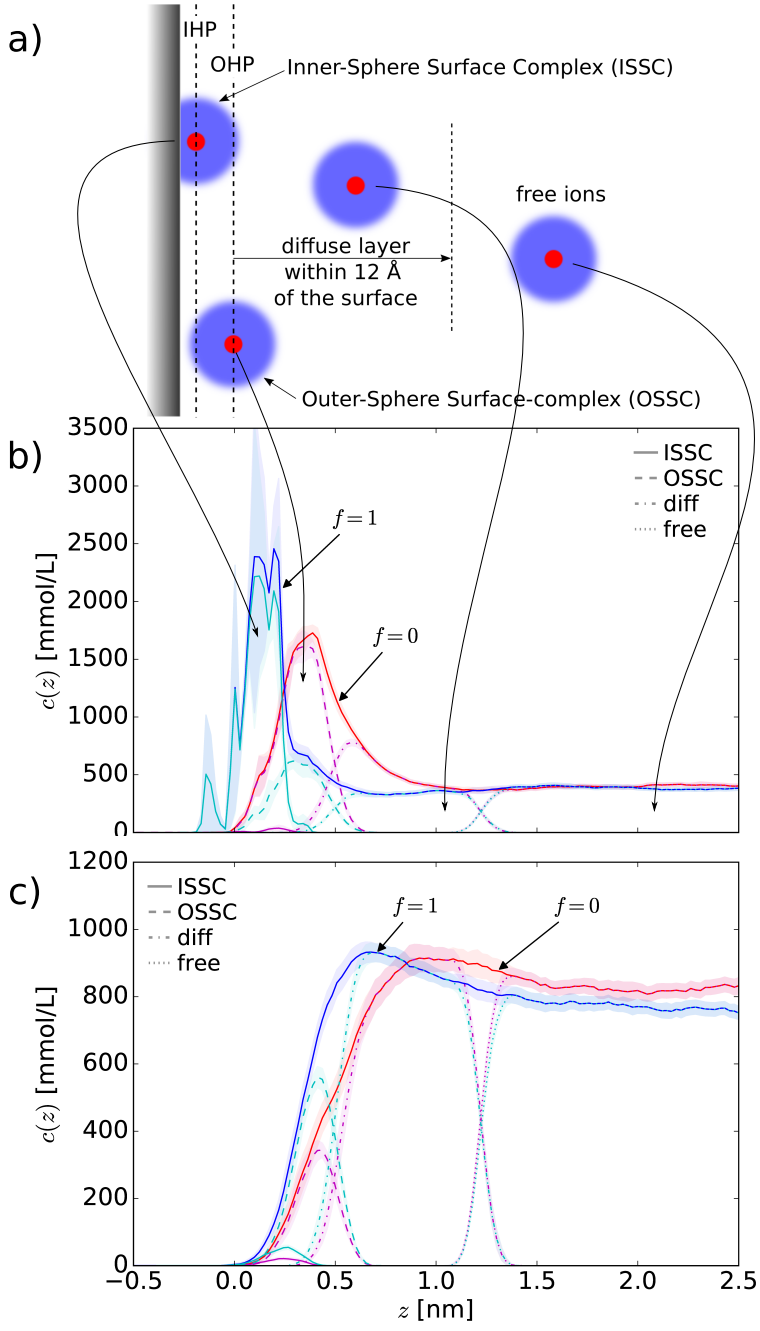

Figure 4.5: (a) Classification of adsorption type of ions into Inner-Sphere Surface-Complexes (ISSC), Outer-Sphere Surface-Complexes (ISSC), those within the diffuse layer, and free ions which form part of the bulk. IHP and OHP are the Inner- and Outer- Helmholtz Planes which are commonly defined as passing through the nuclei of ions forming ISSC and OSSC respectively. (b) Ca^{2+} and (c) Cl^{-} concentration profiles $c(z)$ normal to the surface at a bulk $CaCl_2$ concentration c_0 of approximately 380 mmol/L. $z = 0$ corresponds to the average hydrogen location at the surface. The confidence intervals are 68 %.

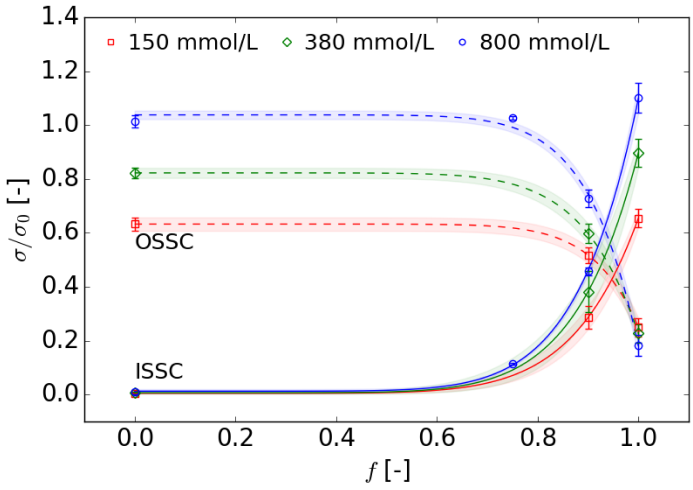

Figure 4.6: Relative charge contribution of ions (Ca^{2+} and Cl^-) forming ISSC and OSSC (σ_{ISSC}/σ_0 and σ_{OSSC}/σ_0) as a function of the scaling parameter f for bulk $CaCl_2$ concentrations of 150, 380 and 800 mmol/L. The confidence intervals are 68 %.

layer are found to increase with increasing f. We attribute this to the increased ion-ion correlations resulting from the increase of Ca^{2+} ions forming ISSC, rather than being a direct consequence of the scaled Cl^--surface interactions. Although direct Cl^- adsorption in the form of ISSC may be unexpected, their existence has been suggested from X-ray experiments [167].

In Fig. 4.6 we quantify the effect of f on ISSC and OSSC formation. We run additional simulations at $f = 0.75$ (800 mmol/L only) and $f = 0.9$ and fit the relative charge contribution of ions forming ISSC and OSSC with a power function $\sigma/\sigma_0 \approx af^b + c$. Between $f = 0$ and $f \approx 0.5$ no change in ISSC and OSSC formation is appreciable. Between $f \approx 0.5$ and $f \approx 0.8$ the ISSC contribution increases slightly for all concentrations considered, from 0 % up to 16 %. The OSSC contribution in return is reduced by 5 to 7 %. From $f \approx 0.8$ to $f = 1$ a steep increase in σ_{ISSC}/σ_0 and steep decrease σ_{OSSC}/σ_0 are observed. At 800 mmol/L the ISSC contribution even overscreens the surface charge, meaning $\sigma_{ISSC}/\sigma_0 > 1$. Here σ_0 denotes the bare surface charge density and σ_{ISSC} and σ_{OSSC} denote the charge density contribution from ions forming ISSC and OSSC respectively.

4.3.2. Comparing With Experiments and Previous MD Results

The Zeta-Potential

We have thus far established that varying f affects the number of ions forming ISSC and OSSC. Next, we will determine what value of f yields good agreement with experimental data for the silica-electrolyte systems studied here. From previous MD studies [113, 170], we know that ions forming ISSC may be considered as virtually

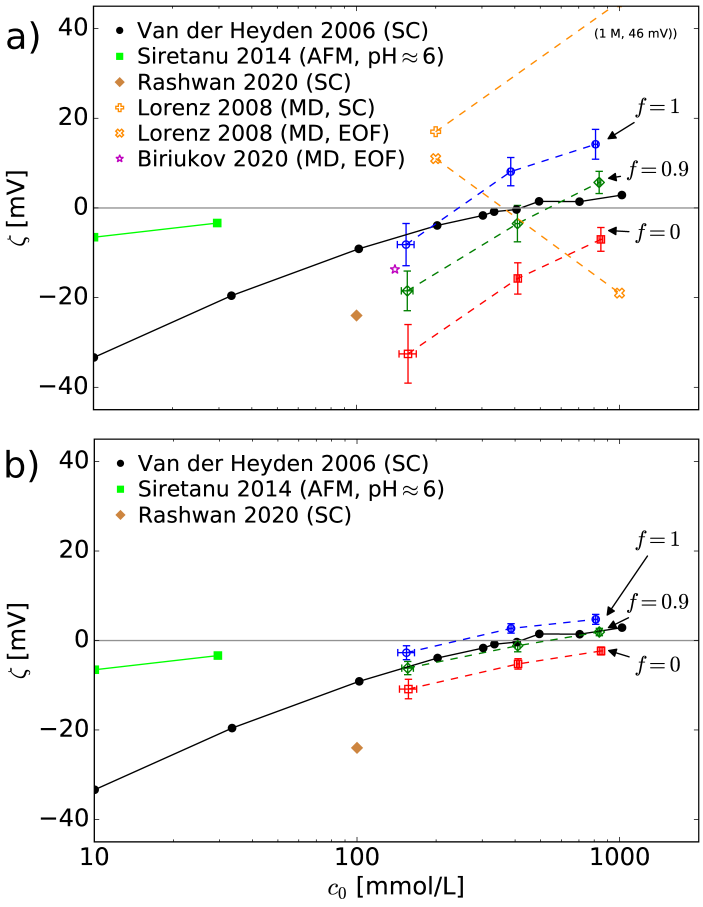

Figure 4.7: ζ-potential vs $CaCl_2$ bulk concentration c_0 at pH 7.5. Full lines and symbols denote experiments, and dashed lines and open symbols denote simulations. (a) The TIP4P/2005 water model viscosity and dielectric are used in the Helmholtz-Smoluchowski equation (Eq. (4.7)) for our results ($f = (0, 0.9, 1)$). (b) The ζ-potential from our work is divided by 3. Confidence intervals are 68 %.

immobile. The scaling factor f therefore controls via the adsorption also the mobility within the EDL. We postulate that an f exists at which the right amount of immobile adsorbed ions are found to reproduce the experimental ζ-potential measurements.

In Fig. 4.7a we compare the ζ-potential at various concentrations between our EOF simulations, the SC experiments of van der Heyden *et al.* [140] and Rashwan *et al.* [211] the Atomic Force Microscopy (AFM) experiments from Siretnau *et al.* [185] and previous MD results from EOF and SC simulations from Lorenz *et al.* [128] and EOF simulations from Biriukov *et al.* [197]. Compared to the results from Lorenz *et al.* [128], our results for the different f-values and the simulation data from Biriukov *et al.* [197] are in reasonable agreement with the experimental results from

van der Heyden *et al.* [140] and Rashwan *et al.* [211]. Notably, there is a considerable difference between ζ-potentials found in van der Heyden *et al.* [140] and Rashwan *et al.* [211] at 100 mmol/L. Comparable differences are found between values obtained from different electrokinetic techniques. For example, Szymczyk *et al.* [27] found that ζ-potentials from EOF and streaming potential experiments for a NaCl solution in a ceramic channel are increasingly dissimilar at an increasing ion concentration and constant pH, up to $\zeta_{EOF}/\zeta_{SP} \approx 2$ at 10 mmol/L of NaCl. On the other hand, the concentration and pH combination at which $\zeta = 0$, was shown to vary little between EOF and streaming potential experiments, for both for NaCl and $CaCl_2$ solutions. These findings have two important implications. First, the concentration of $\zeta = 0$ can be obtained without relying on extensive knowledge or assumptions about the nanoconfined fluid properties and the relation between ζ-potential and fluid transport. This makes this concentration uniquely suitable to tune the MD cross interaction scaling factor f, as we will do in the following. Second, the consistent isoelectric point between the EOF and streaming potential experiments rules out significant differences in surface sample or environmental conditions, suggesting that the differences between the finite ζ-potential values mainly originate from inaccuracies in the linear relationship between the ζ-potential and the measured quantities (i.e. Eqs. (4.4) and (4.7)) and in the fluid coefficients used in these models. As such, finite ζ-potential values, and thus the slope of the curves in Fig. 4.7a, are less suitable as a means to validate MD results against experimental data. In an analogy to the isoelectric point, which is the pH at which $\zeta = 0$ for a fixed concentration, we will call the concentration at at which $\zeta = 0$ for a fixed pH the Isoelectric Concentration (IEC).

We were able to reproduce the IEC (≈ 400 mmol/L for a $CaCl_2$ electrolyte in a fused silica slit pore [140]) in our simulations almost perfectly by setting $f = 0.9$. With $f = 0$ (thus the standard LB mixing rule) the IEC is overpredicted, while with $f = 1$ it is underpredicted. Furthermore, in Fig. 4.7b we show that by scaling the ζ-potential to a third of its value, also good agreement in the slope between the SC experiments of van der Heyden *et al.* [140] and our EOF simulations can be achieved. This is equivalent to reducing the viscosity in confinement to a third of its bulk value. Such a reduction is unexpected, but has been reported in MD simulations depending on the method of determining the viscosity [212]. However, this is difficult to believe as the flow velocity can be shown to be independent of channel width [206], and an enhancement of viscosity near the surfaces is generally expected and predicted (i.e., visco-electric and electroviscous effects) [54, 165, 213–215]. In a similar fashion, a local increase of the dielectric permittivity can also explain the disagreement. A misrepresentation of the concentration-dependent ion diffusion coefficients may be yet another factor affecting the slope. For example, the Madrid-2019 Ca^{2+} diffusion at infinite dilution has been found to be overpredicted by 12 % while at 500 mmol/L it was underpredicted by 20 %. From similar simulations the Cl^- diffusion was found to be underpredicted by 21 % at infinite dilution and 40 % at 500 mmol/L [11, 22, 97, 207, 208]. This may pervert the transfer of velocity from ions to water molecules through viscous forces. As a result, we argue the difference in slope to be due to modeling errors, either of the force field itself, differences between the

experimental and simulation conditions, or differences arising from the models used in EOF and SC experiments and simulations (Eqs. (4.7) and (4.4)).

In conclusion, only the isoelectric point and concentration can be used to compare results between various electrokinetic techniques and between simulations and experiments unambiguously. Here $f = 0.9$ is shown to yield the correct IEC in our simulations and will therefore be used in the remainder of this chapter. We do however not exclude, that f may in fact be concentration or pH dependent.

From Zeta-potential to Effective Surface Charge

Similar to the ζ-potential, which is defined as the electrochemical potential at the no-slip plane ($\zeta = \psi(z_{\text{no-slip}})$), the effective surface charge density σ^* is defined as the charge density at the no-slip plane $\Gamma(z_{\text{no-slip}})$. The effective surface charge density is calculated in various experimental studies using electrokinetic techniques or force measurements, making it a potentially suitable means for comparison. From an experimental point of view, the effective surface charge density σ^* and the ζ-potential can be directly related via the Grahame equation [2, 216]

$$\sigma^* = \sqrt{8 c_0 \varepsilon_0 \varepsilon_r k_B T} \sinh\left(\frac{\nu_i e \zeta}{2 k_B T}\right), \tag{4.9}$$

with k_B being the Boltzmann constant, T the temperature, e the elementary charge and ν_i the ion valency of ion i (2 for Ca^{2+} and 1 for Cl^-). This relation suggests that the events of charge inversion and ζ-potential inversion are directly related. However, this hinges on several assumptions. First of all the charge density distribution is assumed to follow a Boltzmann distribution [217], neglecting ion-ion correlations and considering ions as point charges. Consequently, it is only valid at small concentrations and can also not reproduce phenomena such as crowding and charge inversion. Furthermore, the derivation of the Grahame equation only applies to symmetric electrolytes. Despite these limitations, the Grahame equation is also frequently used at high concentrations and for asymmetric electrolytes. We note that the effect of using asymmetric electrolytes and treating these as symmetric in the Grahame equation is in fact very small as shown in Fig. 4.8 by comparing the Grahame equation against a variation for asymmetric electrolytes [218].

A more precise way of determining σ^* is by extracting it directly from the screening function $\sigma^* = \Gamma(z_{\text{no-slip}})$ given by Eq. (4.10) [23, 54, 113].

$$\Gamma(z) = \sigma_0 + \int_0^z \rho_e(z')dz'. \tag{4.10}$$

However, this is only possible when $\rho_e(z)$ and $z_{\text{no-slip}}$ are known. In MD simulations, $\rho_e(z)$ can be determined (Fig. 4.9a), but no rigorous method exists to determine the no-slip plane ($z_{\text{no-slip}}$). One could for example try to determine this plane from ion mobilities or flow profiles (Fig. 4.10b). However, the flow profiles near amorphous silica have undulations and even regions of local flow reversal. In some cases, also multiple no-slip planes could be defined.

Perhaps the most rigorous method to determine $z_{\text{no-slip}}$ is to compute the intersection between the electrostatic potential $\psi(z)$ and the ζ-potential (Fig. 4.10a).

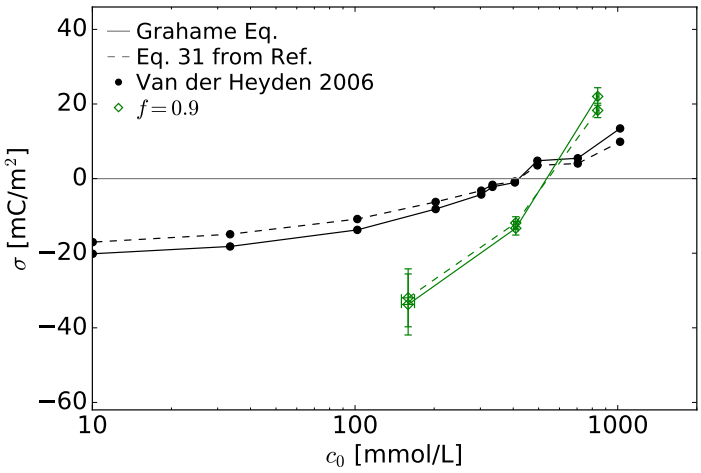

Figure 4.8: Effective surface charge σ^* at various concentrations obtained via the Grahame equation (Eq. (4.9)) and Eq. 31 from [218].

Where the ζ-potential is obtained from the Helmholtz-Smoluchowski equation and $\psi(z)$ from the Poisson equation with boundary conditions $d\psi(z_{\text{wall}})/dz = -\sigma_0/\varepsilon_0\varepsilon_r$ and $\psi(z_{\text{bulk}}) = 0$. Note that in the calculation of $\psi(z)$ full charges are used, while the ζ-potential is determined considering a streaming velocity that is scaled up by 1/0.85. The resulting $z_{\text{no-slip}}$ are added as + symbols in Figs. 4.9b and 4.10a. While $z_{\text{no-slip}} \approx 0.2$ nm is nearly the same for all 3 concentrations, it is not really a plane of zero velocity (Fig. 4.10b). Furthermore, the resulting $\Gamma(z_{\text{no-slip}})$ is considerably lower than $\sigma^*_{\text{Grahame}}$ as shown in Fig. 4.11a.

Alternatively, we could use the common assumption that the no-slip plane is within 1 Å of the Outer-Helmholtz Plane (OHP) [219], which is defined as passing through the nuclei of ions forming OSSC (see Fig. 4.5a). On an amorphous surface, this opens up room for interpretation of the meaning and location of the OHP. From Fig. 4.9b the location of the OHP could be understood as coinciding with the maximum in the OSSC density, the intersection between the OSSC and diffuse layer densities, or the end of the OSSC region, resulting in $z_{\text{no-slip}} \approx 0.3$, $z_{\text{no-slip}} \approx 0.5$ and $z_{\text{no-slip}} \approx 0.6$ nm, respectively, contributing to a very ambiguous definition of $z_{\text{no-slip}}$. In fact, the existence of a single no-slip plane is under most circumstances, as for our system, illusory.

Instead of dwelling on a physical location for the OHP, we calculate the charge contribution associated with the OHP directly from the number of ions forming ISSC and OSSC. Fig. 4.11a shows that this definition also yields reasonable agreement with the Grahame equation and the experimental data. Furthermore, reasonable agreement is found across the MD studies, with the exception of our previous work in Ch. 3 [23]. However, Fig. 4.11b displays that the relative charge contribution of ISSC and OSSC differ considerably between different MD studies. We predict $\sigma_{\text{ISSC}}/\sigma_0$

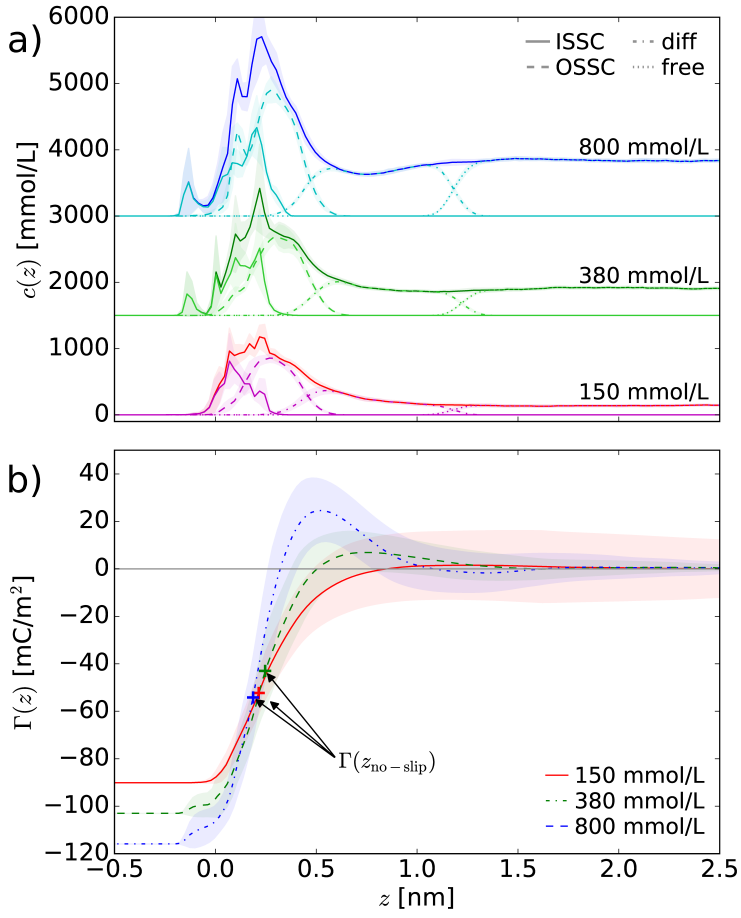

Figure 4.9: (a) Ca^{2+} concentration profile dividing ions into ISSC, OSSC, those within the diffuse layer and free ions. (b) Screening function $\Gamma(z)$ from Eq. (4.10) and markers indicating the Γ value at the no-slip plane $z_{\text{no-slip}}$. The confidence intervals are 68 %.

between 25 and 45 % and $\sigma_{\text{OSSC}}/\sigma_0$ between 50 and 75 % for our concentration range, while Lorenz *et al.* [127] for example predict $\sigma_{\text{ISSC}}/\sigma_0$ between 65 and 90 % and $\sigma_{\text{OSSC}}/\sigma_0$ between 25 and 40 %. Döpke *et al.* [23] even predict overscreening from the ISSC contribution alone ($\sigma_{\text{ISSC}}/\sigma_0 > 1$), while the ions forming OSSC had no net contribution due to a balance between Ca^{2+} and Cl^- ions forming OSSC. These differences clearly showcase that different MD simulation force fields do not yield consistent amounts of ion adsorption without specifically tuning the force field for this property as we have essentially done in this study.

Based on our simulations corresponding to $f = 0.9$ we conclude that for realistic amorphous silica in contact with an aqueous solution of 100 to 800 mmol/L $CaCl_2$

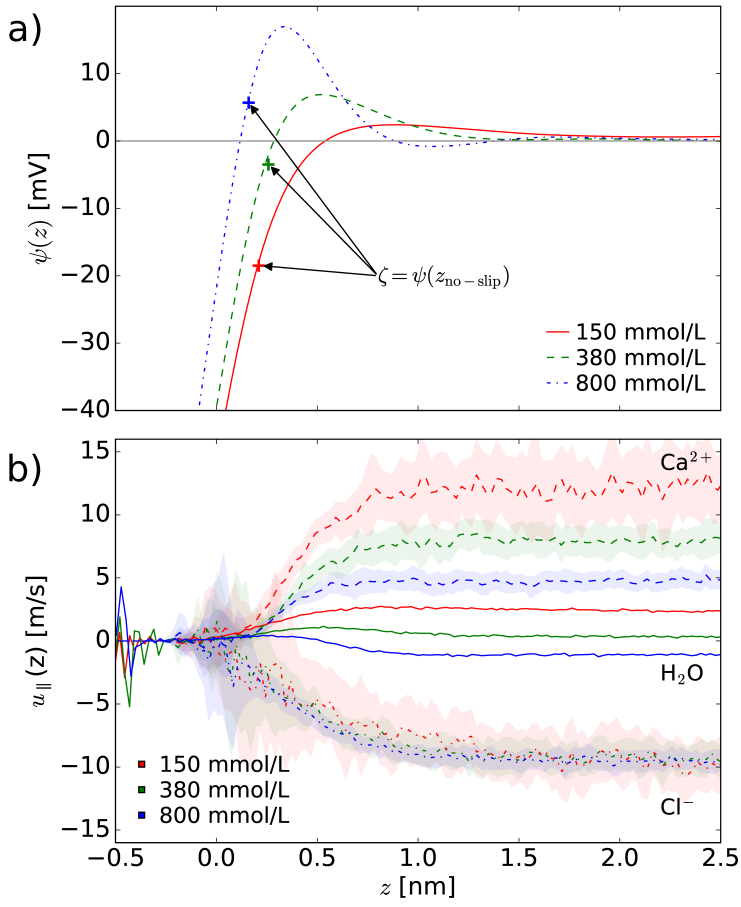

Figure 4.10: (a) Electrochemical potential ψ (lines) from the Poisson equation (Eq. (4.2)) and ζ-potential (markers) from EOF simulations using the Helmholtz-Smoluchowski (Eq. (4.7)). (b) Scaled velocity profiles (factor 1/0.85) of Ca^{2+}, Cl^- and H_2O for $E_x = 0.2$ V/nm. The confidence intervals are 68 %.

at pH 7.5, approximately 25 to 45 % of the ions adsorb specifically, in other words forming ISSC (see Fig. 4.11b). The respective ion surface densities are given in Fig. 4.12.

4.3.3. Mobility of Ions Within the EDL

Until now we have only briefly discussed dynamics when defining $z_{\text{no-slip}}$ and in relation to the slope of the ζ-potential-concentration curve. Here we discuss the dynamics within the EDL in more detail since this is essential to parametrize a relation between measured transport and the EDL structure.

Combining our EOF simulations with kinetic theory [220, 221] we obtain the av-

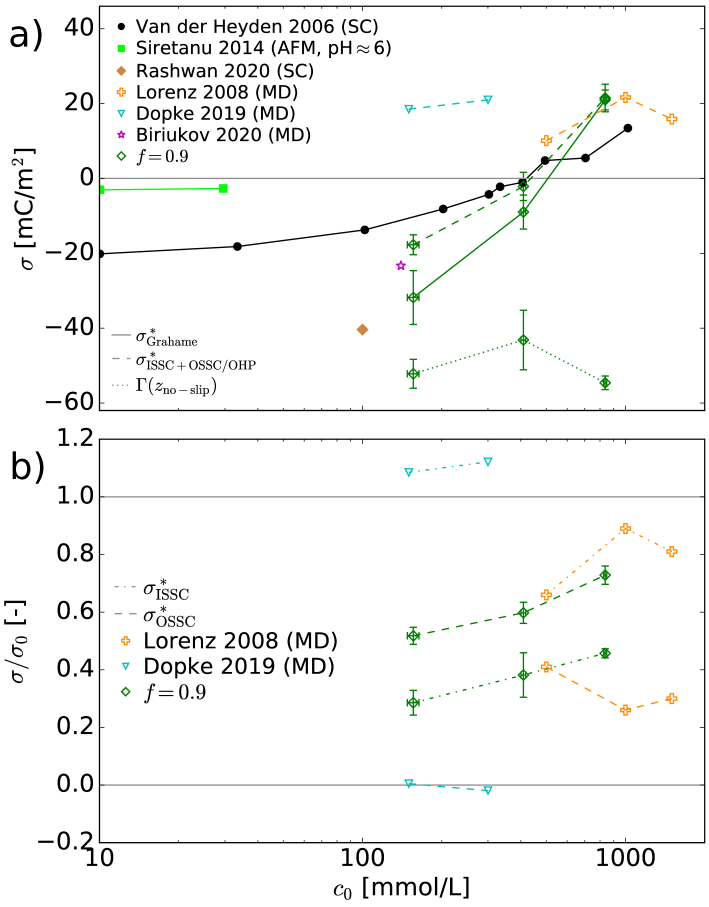

Figure 4.11: (a) Differing definitions of the effective surface charge density $\sigma^*_{\text{Grahame}}$, $\Gamma(z_{\text{no-slip}})$ and $\sigma^*_{\text{ISSC+OSSC}} \approx \sigma^*_{\text{OHP}}$ from experiments and MD simulations at varying concentrations. (b) The relative charge contributions of σ^*_{ISSC} and σ^*_{OSSC} for various MD studies. The confidence intervals are 68 %.

erage ion transport diffusion coefficient D_k^{X} per ion $\text{X} \in \left\{\text{Ca}^{2+}, \text{Cl}^-\right\}$ and adsorption type $k \in \{\text{ISSC}, \text{OSSC}, \text{diff}, \text{free}\}$ following

$$D_k^{\text{X}} = \frac{\int \rho_{n,k}^{\text{X}}(z) D_k^{\text{X}}(z) dz}{\int \rho_{n,k}^{\text{X}}(z) dz}. \tag{4.11}$$

Here $\rho_{n,k}^{\text{X}}(z)$ is the number density profile and $D_k^{\text{X}}(z)$ the ion transport diffusion profile given by

$$D_k^{\text{X}}(z) = \frac{\mu_{q,k}^{\text{X}}(z) k_B T}{\nu e}, \tag{4.12}$$

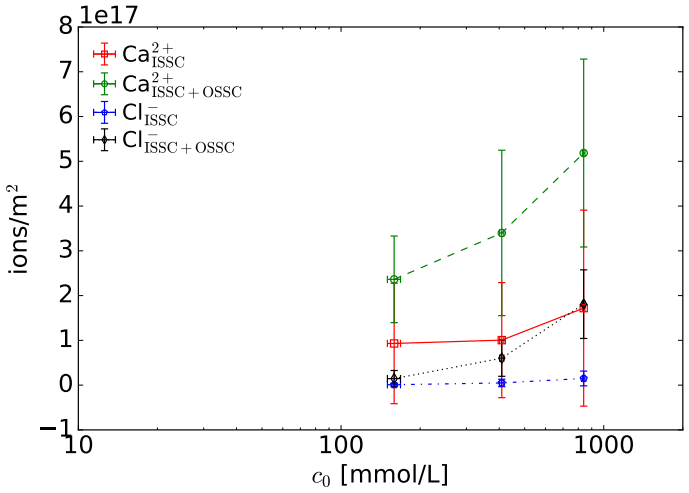

Figure 4.12: Ion surface density based on ion adsorption type.

with

$$\mu^{X}_{q,k}(z) = \frac{u^{X}_{x,k}(z) - u^{water}_{x}(z)}{E_x}. \tag{4.13}$$

Note that the streaming velocities $u^{X}_{x,k}(z)$ and $u^{water}_{x}(z)$ are scaled by 1/0.85 to compensate for the scaled charges [197]. The resulting ion transport diffusion coefficients D^{X}_{k} are provided in Fig. 4.13.

In agreement with previous MD studies [11, 22, 113, 170], the dynamic Stern layer theory [222–226] and the viscoelectric model [213, 214], D^{X}_{k} reduces with proximity to the surface and increasing concentration. The free ion transport diffusion coefficient D^{X}_{free} found here is in reasonable agreement with previously reported values for this force field of 6.3e-10 and 12.3e-10 m^2/s for Ca^{2+} and Cl^{-} respectively at 500 mmol/L and 8.9(8)e-10 and 16.0(8)e-10 m^2/s respectively at infinite dilution [11, 22]. In the diffuse layer, D^{X}_{diff} is between 70 and 85 % of D^{X}_{free}. For ions forming OSSC the diffusion is further reduced to between 40 and 60 % of D^{X}_{free}. For ions forming ISSC, we find $D^{Ca^{2+}}_{ISSC}/D^{Ca^{2+}}_{free} < 0.002$ and $D^{Cl^{-}}_{ISSC}/D^{Cl^{-}}_{free} < 0.02 - 0.06$. We attribute the difference in diffusion between Ca^{2+} and Cl^{-} ions forming ISSC to the difference in adsorption sites. While Ca^{2+} ions adsorb specifically on negatively charged O^{-} sites, we expect Cl^{-} ions to adsorb specifically on either SiOH or surface Si atoms, which have their charges fully compensated by neighboring wall atoms. Consequently, the energy required to remove an adsorbed Ca^{2+} ion is greater than that required to remove an adsorbed Cl^{-} ion.

In conclusion, for realistic amorphous silica in contact with an aqueous solution between 100 and 800 mmol/L $CaCl_2$ at pH 7.5, the diffuse layer clearly possesses a reduced mobility, questioning the use of bulk transport properties throughout the

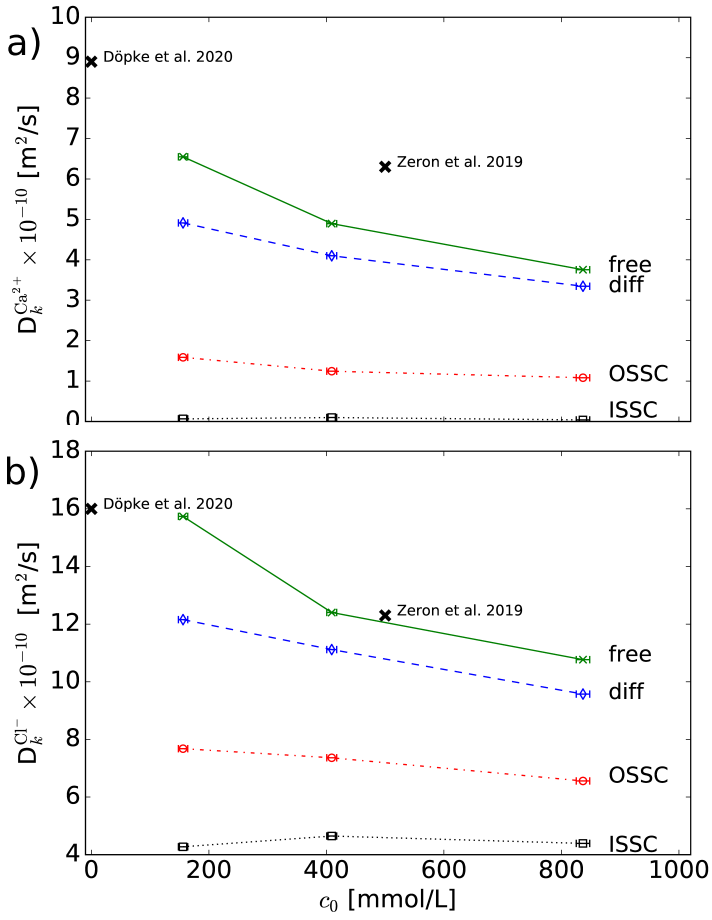

Figure 4.13: Transport diffusion coefficients D_k^X based on ion adsorption types $k \in \{\text{ISSC}, \text{OSSC}, \text{diff}, \text{free}\}$ when $f = 0.9$. (a) for X = Ca^{2+}. (b) X = Cl^-. The confidence intervals for the concentration are 68 %. The confidence intervals for D_k^X are omitted since these exceed the axis limits of the shown figure.

diffuse layer as is done in most continuum models (Gouy-Chapman and Basic Stern Model for example). Furthermore, Ca^{2+} ions forming ISSC can be considered as virtually immobile. However, the same assumption is not valid for Cl^- ions forming ISSC nor for Ca^{2+} and Cl^- ions forming OSSC. However, the usual assumption of an immobile Stern layer (containing ISSC and OSSC) may yield seemingly correct results if the reduced mobility in the diffuse layer is compensated by a finite mobility of ions within the Stern layer.

4.4. Conclusion

We have shown that the experimentally measured concentration at which the ζ-potential equals zero in a silica slit pore filled with a $CaCl_2$ electrolyte at pH 7.5 can be reproduced in EOF MD simulations. This concentration which we called isoelectric concentration (IEC), was argued to be least susceptible to modeling errors, thus providing a suitable experimental reference point to benchmark non-equilibrium MD simulations. We demonstrated that it cannot be taken for granted that MD force fields automatically reproduce correct and consistent EDL properties. For example, previous MD studies have shown inconsistent amounts of ion adsorption, with most of them predicting an abundance of ISSC formation and thus underpredicting the experimental IEC [23, 127, 128]. We believe that to a great extent this is caused by the fact that ion-surface interactions are typically not optimized or validated, but rather computed from standard mixing rules. Our data shows that ion adsorption is extremely sensitive to the ion-surface interaction and we presented an approach in which this interaction was tuned to obtain the right amount of specifically adsorbed ions necessary to reproduce the IEC.

The slope of the ζ-potential against concentration between 100 and 800 mmol/L varies between different experiments and simulations. Based on the rather consistent isoelectric point and concentration, we argue that the differences in slope are not caused by differences in surface sample, but rather by modeling errors. We discussed various possible modeling errors that could bias the information obtained from experiments or simulations. One reason could be that the fluid transport properties in simulations and experiments differ. For example, different channel widths can lead to differences in the viscosity. Also, the force field used is known to slightly underpredict the experimental viscosity of water. Another concern may be the fact that electrostatic screening is not considered by non-polarizable force fields. The scaled charges of the Madrid-2019 ions account for the electrostatic screening in bulk water simulations, but the effect and validity of scaled charges in confinement still needs to be evaluated in more detail [200].

The diffusion coefficients of ions forming ISSC, OSSC, those within the diffuse layer and free ions were calculated to assess the validity of the common assumption of an immobile Stern layer and the use of bulk transport values in diffuse layer. It was found that for Cl^- ions no clear immobile layer can be found, while for Ca^{2+} ions the ISSC layer is virtually immobile. This difference is attributed to the adsorption sites of Ca^{2+} and Cl^-. In spite of ions forming OSSC frequently being classified as immobile, we found these do have a diffusion coefficient ranging from 40 to 60 % of D^X_{free}. Finally, the ions within the diffuse layer, which are commonly classified as fully mobile were found to present a reduced diffusion as low as 70 % of D^X_{free}. These findings clearly oppose the traditional interpretation of immobile Stern layer and bulk like diffuse layer. However, the deficit in the diffuse layer may be compensated by the finite diffusion in the Stern layer.

The findings in this study have wide reaching implications in improving the understanding and interpretation of experiments in which the results depend on the EDL structure and dynamics. For example, empirical surface complexation models pro-

vide estimates of properties within the Stern layer and thereby boundary conditions for a continuum model spanning the diffuse and bulk regions. Most of these models require the specification of the Stern layer capacitance. With the right distribution of ions within the Stern layer given by detailed MD simulations, this capacitance can now be calculated accurately.

Finally, our results can be used to supplement experimental findings where direct measurement or unambiguous interpretation is not possible. Albeit the simulations presented here are at relatively high concentrations, the scaling parameter derived here is thought to be also valid at lower concentrations. One way of verifying this could be to use the isoelectric point when comparing experiments and simulations. This is the pH at which $\zeta = 0$ when the concentration is kept constant. Consequently, resulting in a similar reduction of errors as for the IEC. In fact, one may be able to find an infinite number of such isoelectric points for a given interface by varying the concentration and/or pH, thus potentially providing an infinite number of unambiguous comparison conditions.

5

Surface Protolysis and the Electrical Double Layer

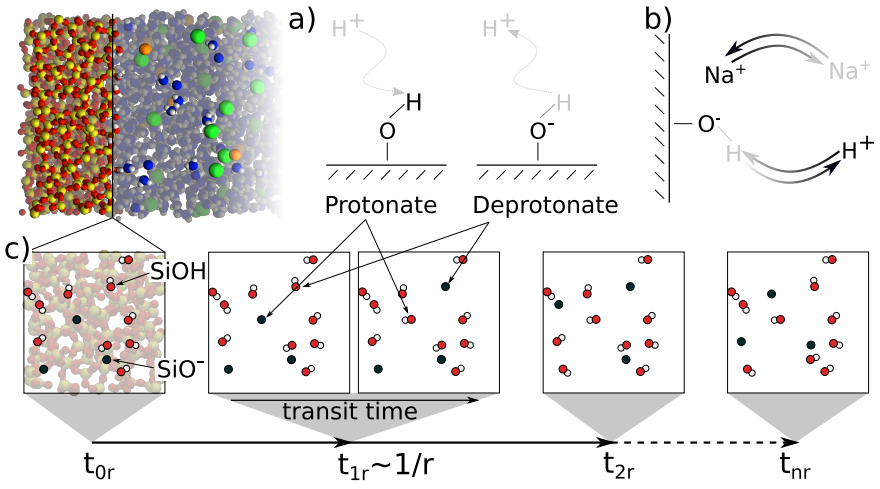

This chapter is based on the paper:

M. F. Döpke, F. W. van der Meij, B. Coasne and R. Hartkamp, *Surface Protolysis and Its Kinetics Impact the Electrical Double Layer*, Phys. Rev. Lett., **128** 056001 (2022).

5.1. Introduction

Solid-liquid interfaces, which are omnipresent in nature, are central to many scientific fields such as colloid and materials science, phase separation and catalysis, and electrochemistry and energy harvesting. A detailed understanding of such interfaces is of paramount importance to design novel energy devices (e.g., batteries, osmotic power membranes) and innovative health or environment applications (e.g., drug delivery capsules, medium depollution or remediation). Solid-liquid interfaces are characterized by two parallel layers of equal charge and opposite polarity known as the electrical double layer (EDL) [3]. The electric charge distribution across these layers is usually described via mean-field models, which disregard the microscopic intricacies of the interfacial structure and chemistry. Beyond such pioneering approaches, researchers have proposed ways to effectively account for molecular details including ion-specific effects, microscopic correlations, and surface charge localization. In contrast, despite its acknowledged interplay with the EDL, surface reactivity is not included in available frameworks. In particular, proton exchange at oxide-electrolyte interfaces, which directly influences hydrogen hopping and diffusion and, hence, surface conductivity [30, 31], is usually disregarded in modeling endeavors as it is implicitly assumed that surface charge distributions evolve too slowly to affect the interfacial fluid structure and dynamics.

Experimentally, proton exchange rates can only be measured from the interface transient response to an applied perturbation such as with pressure-jump techniques [227]. However, with most methods, only lower bounds or orders of magnitude can be estimated for such reaction rates. For instance, in atomic force microscopy experiments on silica with tip speeds as fast as 0.5 μm/s, charge regulation due to the EDL overlap between the surface and tip is so fast that no hysteresis is observed in force-distance curves [228]. This suggests that surface chemistry adapts within milliseconds – a value consistent with flow experiments on mineral surfaces probing the electronic response induced by composition changes [168, 203, 229]. Dissolution experiments also provide lower bounds for protolysis rates. To form a $Si(OH)_4$ molecule from a SiO_4 tetrahedron in SiO_2, multiple hydrolysis ($MOM + H_2O \rightleftharpoons MOH + MOH$) and protolysis ($MOH \rightleftharpoons MO^- + H^+$) reactions occur [230] (with protolysis being very fast and nearly activation-less compared to hydrolysis [231]). Dissolution rates of 10^{-7} mol/m^2/s for silica under neutral pH, thus serve as a lower bound for surface protolysis rates [232, 233]. Despite such estimates, exact equilibrium protolysis rates and their influence on the EDL cannot be experimentally probed.

Theoretically, while first-principles calculations provide insights into reaction mechanisms, energy barriers and adsorption energies, the small system sizes in these approaches [O(10-100 atoms)] are insufficient to study the fluid response [234–238]. On the other hand, classical molecular dynamics (MD) simulations [$O(10^3 - 10^5)$ atoms] probe the fluid response, but they generally do not account for chemical reactions. Only recently, the computational power has increased to allow atomistic MD simulations to probe chemical reactions and fluid responses. In this context, the reactive force field ReaxFF [239] is an important landmark but parameters for protolysis are not available. In contrast, the dissociative force field MGFF [240, 241] allows reproducing OH bond dissociation or formation involved in proton reactions. Using

this force field, when set in contact with water, protolysis rates up to 2×10^5 mol/m^2/s were found for hydroxylated silica surfaces containing strained sites (Si(OH)Si and $SiOH_2$ defects), while smaller rates between 900 and 1750 mol/m^2/s were assessed when only considering silanol sites (SiOH) [32, 33]. The OH bond lifetime was found to be broadly distributed from fs to ns with an average of the order of ps. Despite its ability to model silanol dissociation, the MGFF force field is unsuitable to study the impact of reaction kinetics on the EDL as ion parameters are not available.

In this chapter, we first develop a novel framework to include surface reactions in classical MD simulations at no additional computational cost. This is achieved by adding every t_r time in the MD simulation a stochastic deprotonation and protonation step between two randomly picked, independent surface sites (one protonated, one deprotonated). Using this effective yet robust strategy, we then investigate the impact of proton exchange and its kinetics on the EDL formed in a prototypical silica-electrolyte system. We find that both the ion distribution and dynamics within the EDL are strongly impacted by proton exchange with significant effects on the system's electrokinetic response. By analyzing the molecular mechanisms of ion diffusion within the EDL, we unravel that ion adsorption times become much shorter when surface protolysis is taken into account while the water structure and dynamics are only indirectly impacted through the electrostatic coupling with ions.

5.2. Methods

5.2.1. Molecular Simulations

An amorphous silica channel was created by annealing (to 4000 K) and quenching (to 298 K at a rate of 2.5 K/ps) a $\beta-$cristobalite and functionalizing the surface following the approach described in Sec. 3.2 of Ch. 3. The obtained silanol density is 4.7 SiOH/nm^2 with 20% isolated, 58% vicinal and 22% geminals. From this point on, the Interface Force Field (IFF) is used for the silica. In between the slabs 2,457 SPC/E water molecules [12] and 28 Joung and Cheatham (JC) NaCl ions [18] were added. Cross interactions within each force field (IFF, SPC/E and JC ions) are applied as recommended by the respective authors. Between the force fields, the Lorentz-Berthelot mixing rule is used (see Eq. (1.7)). The pH of the solution was set to 8 by deprotonating 8 silanols per wall (16 total), based on titration results – surface charge of -103 mC/m^2 at 0.7 mol/L of NaCl [25]. The excess charge is balanced by adding an equal amount of excess Na^+ ions. The fluid density was adjusted by pushing the walls towards each other for 20 ns with an equivalent force to 1 atm, yielding a channel height of $H \approx 6$ nm, a fluid density near 1 g/cm^3 and an electrolyte concentration between 0.66 and 0.74 mol/L as shown in Fig. 5.1.

Protonation or deprotonation reactions of the form $MOH \rightleftharpoons MO^- + H^+$ were implemented in our MD simulations by adjusting the partial charges and Lennard-Jones parameters of a MO^- group to a MOH group and *vice versa*. As shown in Fig. 5.2a, without explicitly forming or breaking OH bonds, this strategy mimics equilibrium situations in which no net adsorption or desorption takes place – protonation and deprotonation events always occur simultaneously. In doing so, direct proton exchange between MOH and MO^- sites avoids dealing with free protons and/or water

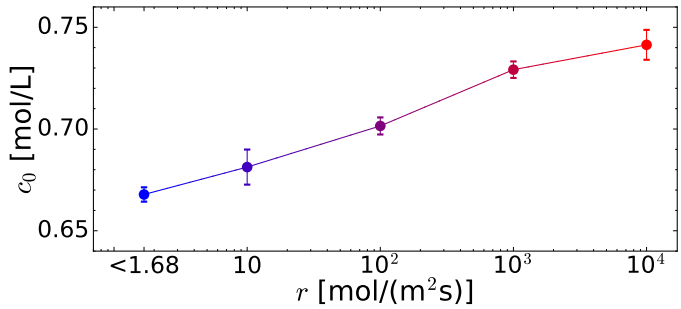

Figure 5.1: Ion concentration c_0 in the center of the channel as a function of the protolysis reaction rate r.

ionization reactions and guarantees a constant overall surface charge. In principle, protonation and deprotonation could be decoupled from each other using a canceling background charge. However, the use of concomitant protonation and deprotonation allows for imposing a rigorous thermodynamic ensemble with well defined constant parameters (surface charge, number of particles, temperature, and overall charge neutrality). As shown in Fig. 5.2c, various reaction rates r can be considered by performing protonation and deprotonation at different time intervals $t_r \sim 1/r$ (see Tab. 5.1, upon decreasing t_r, the simulation time step was decreased to ensure numerical stability). This implementation does not account for mutual coupling between fluid structure and surface chemistry. In reality, the probability to protonate or deprotonate a site depends on its environment at a given time. In principle, these probabilities can be calculated using for example reactive force fields such as those cited above. However, calculating an instantaneous energy landscape on-the-fly leads to prohibitive computational costs and statistical challenges. Moreover, including explicit water ionization reactions and water ions (10^{-6} mol/L for H^+/H_3O^+ and 10^{-8} mol/L for OH^- in bulk at neutral pH) is out of reach (even for large MD systems like here, the number of water ions is too small to ensure statistical significance). To circumvent such issues, we use here an effective approach by stochastically selecting the surface groups to react at a given time. With such a coarse-grained description, we neglect (i) mechanisms occurring on a time shorter than the chemistry timescale (1-10 fs), (ii) possible electric screening of surface sites by lingering protons (H^+) or hydroniums (H_3O^+) and (iii) the fact that protonation and deprotonation occur independently. These simplifications may result in overpredicting the impact of surface reactions but we expect such coarse-graining to be relevant as we only probe molecular events occurring in the EDL at longer times. Finally, to guarantee numerical stability, the parameter change between MOH and MO^- groups – which allows mimicking concomitant protonation and deprotonation – is linearly adjusted over 1 ps.

In total, 4 different types of MD simulations, and 3 independent runs, were performed for each reaction rate specified in Tab. 5.1 (12 simulations per reaction rate, 60 simulations in total).

Table 5.1: Summary of protolysis reaction rates and respective simulation conditions. The desorption rate constant is calculated with a total silanol density (SiOH + SiO^-) of 4.7 SiOH/nm^2. The fraction of occupation (SiOH) is 0.86. The adsorption rate constant cannot be determined since no H^+ concentration is present explicitly. Note that $K = k_{ads}/k_{des}$ and $r = k_{ads}\rho_{H^+}\rho_{SiO^-} = k_{des}\rho_{SiOH}$.

r [mol/(m^2s)]	k_{des} [1/s]	time between events [ps]	characteristic re-protonation time [ps]	dt [fs]
< 1.68	2.5×10^5	-	-	2
10^1	1.5×10^6	13430.	107440.	2
10^2	1.5×10^7	1343.0	10744.0	2
10^3	1.5×10^8	134.30	1074.40	1
10^4	1.5×10^9	13.430	107.440	0.5

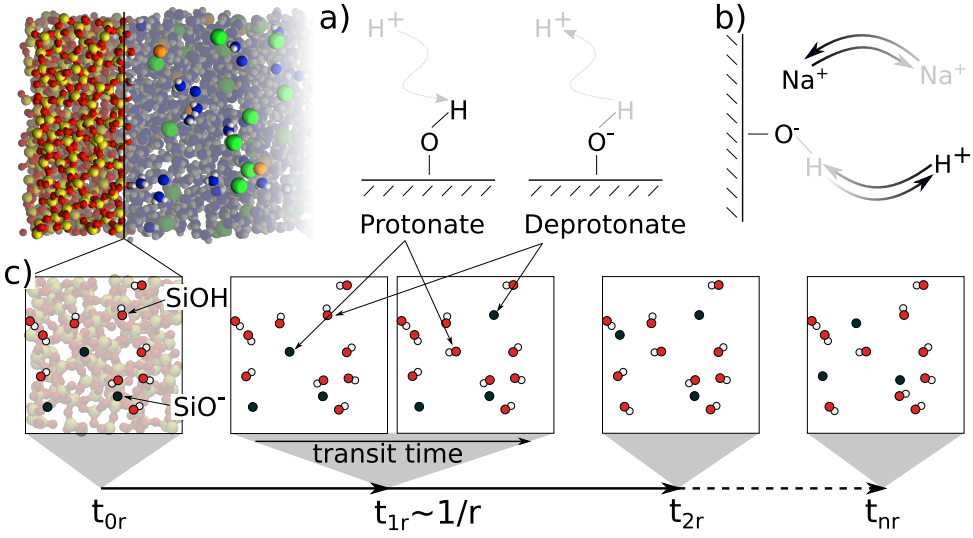

Figure 5.2: a) Schematic view of protonation/deprotonation reactions at a solid-liquid interface. Black font indicates that interatomic interactions are turned on, while grey font indicates that these are turned off. b) Protolysis reactions impact ion adsorption by allowing an ion to adsorb after site deprotonation (black) or forcing it to desorb after site protonation (grey). c) Flow diagram of simulation protocol with time $t_r \sim 1/r$ between protolysis reactions. Protonation/deprotonation events take place over a transit time to ensure numerical stability.

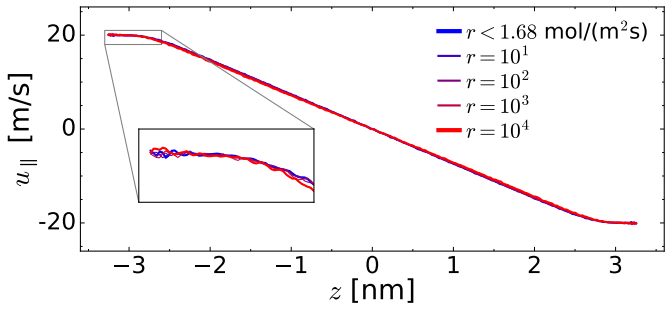

Figure 5.3: Shear velocity profiles.

1 Equilibrium: No further modification of the simulation protocol was made. Ion and water density and diffusion profiles, screening function and water molecule orientations were extracted from these simulations (See Figs. 5.9, 5.10a,b, 5.11a,b and 5.5).

2 Shearing walls: The silica walls on either end of the channel were sheared at a rate of ± 20 m/s. The resultant force on the fluid particles and fluid velocity profiles (see Fig. 5.3) were used to calculate the viscosity profile (Fig. 5.11c) following

$$\eta(z) = \frac{F_\parallel}{A}\left(\frac{\mathrm{d}u_\parallel}{\mathrm{d}z}\right)^{-1}, \tag{5.1}$$

where $F_\parallel$ denotes the tangential force exerted on the fluid and A the surface area.

3 Poiseuille flow: An external acceleration of $a = 2.16$ m/s^2 was applied to all fluid particles, equivalent to a nominal pressure difference of 75 atm over 3.5 nm channel length following

$$a = -\frac{\nabla p}{\rho}. \tag{5.2}$$

The resulting flow profiles are given in Fig. 5.13b.

4 Electro-osmosis: An electric field of 0.2 V/nm was applied to the fluid, accelerating cations in the direction of the electric field and anions in the opposite direction (see Fig. 5.4). Water molecules are dragged along due to viscous forces (see Figs. 5.13b and 5.4).

The external forces driving the non-equilibrium MD simulations – wall velocity/pressure difference/electric field – are chosen in line with previous MD studies and can be shown to still be within the linear response regime [26, 130, 165].

All simulations were performed using the LAMMPS simulation package [80]. The temperature was controlled connecting either the entire system, in the case of equilibrium MD (1), or only the walls, in the case of non-equilibrium MD (2-4), to an external heat bath of 298 K through the Nosé-Hoover thermostat. For electro-osmosis this approach has been shown in Ch. 4 to yield a fluid temperature around 295 K

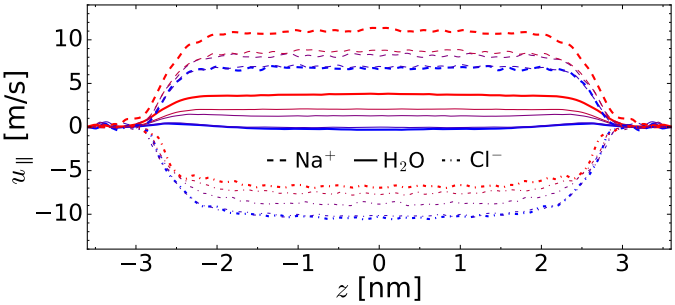

Figure 5.4: Electroosmotic flow profiles. The color coding is the same as in Fig. 5.3.

(Fig. 4.4b). The thermostat damping factor was set to 100 dt. Boundary conditions were implemented as periodic with a vacuum equal to 3 times the box length in the z direction to remove dipole inter-slab interactions [156]. Cut-off distances were set to 12 Å for both Lennard-Jones and Coulomb interactions, and the long-range electrostatic interactions were resolved with the particle-particle particle-mesh method with a relative precision of 10^{-4}. The time steps were adjusted to the rates as specified in Tab. 5.1. All simulations were equilibrated for 20 ns, followed by 80 ns production during which statistics were gathered every 400 ps.

Additionally to the just described simulations of a slit pore, bulk liquid simulations of 40 ns containing only water (2,140 water molecules) and ions (between 0 and 40 NaCl ions) were performed to provide a reference point for bulk properties in the center of the channel. For these simulations, the same force fields and settings as for the channel configurations were used, and additionally the pressure was regulated at 1 atm with the Nosé-Hoover barostat and a damping factor of 1000 dt.

5.2.2. Diffusion Coefficients

The diffusion coefficients D_i of component i are calculated from the mean-squared-displacements (MSD $= \left\langle \sum_{j=1}^{N_i} \left(r_{j,i}(t) - r_{j,i}(0) \right)^2 \right\rangle$) following

$$D_i = \lim_{t \to \infty} \frac{\text{MSD}}{2nt}, \tag{5.3}$$

with n denoting the dimensionality (3 for an isotropic system when averaging over x, y and z, 2 for the parallel diffusion coefficient and 1 for the perpendicular diffusion coefficient), using a multiple time origin implementation with windows of 4 ns every 40 ps. The calculation of the local MSD in confinement is further adapted to take into account only particles within a specified bin. Individual particle squared displacement lines are cut off once the respective particle leaves the specified bin and a new squared displacement line is started at the respective time origin when a new particle enters the bin. As a result of this implementation, the number of particles within each bin is not constant in time and special care is taken to normalize the MSD accordingly. Furthermore, if too few particles remain continuously within the specified bin, not

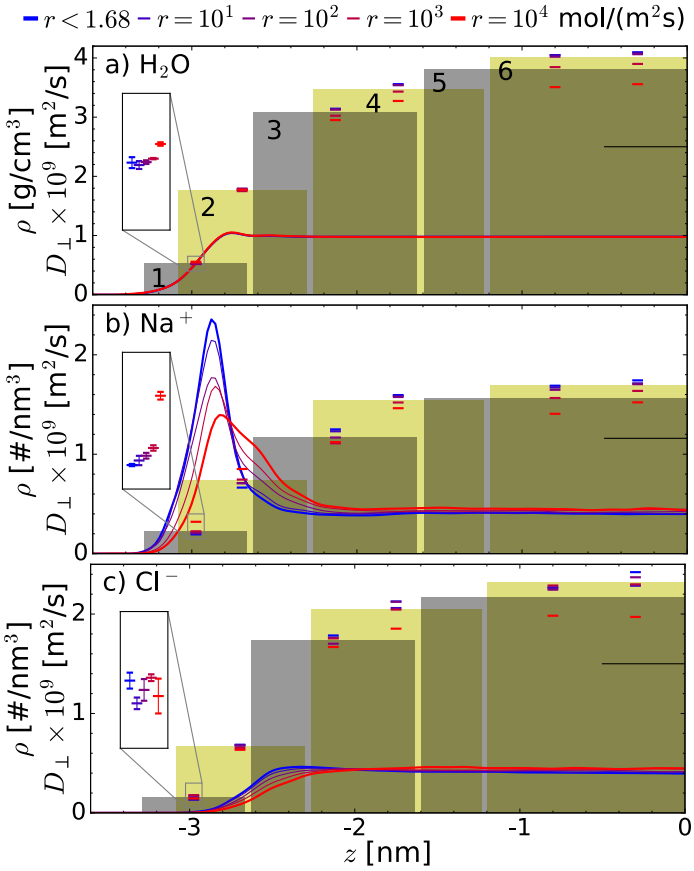

Figure 5.5: a) Water, b) Na^+ and c) Cl^- density profiles (lines) and perpendicular diffusion coefficients (symbols). The black lines display the bulk diffusion coefficients obtained from independent bulk simulations containing only water and ions (see Fig. 5.6). The shaded grey and yellow shaded areas denote the 6 bins selected for the local MSD calculation. Their height is varied to the diffusion coefficient obtained in each bin for clarity.

enough statistics can be gathered in the linear regime of the MSD-t plot to obtain the diffusion coefficient. The size of the specified bins, is thus a trade-off in which on the one hand as many particles as possible remain continuously within each bin, while on the other hand, each bin is small enough such that it only represented a small part of the entire system. We found that the trade-off is best optimized using 6 overlapping bins as shown by the shaded areas through Figs. 5.5a-c.

The parallel and perpendicular MSDs for each bin are provided in Figs. 5.7 and 5.8, respectively. The solid part of the MSDs represents the selected linear region used in Eq. (5.3) to calculate the diffusion coefficients. The resulting parallel and perpendicular diffusion coefficients are given in Figs. 5.9, 5.5 and 5.11a. Note that no finite-size correction is used for the parallel and perpendicular diffusion coefficients, while the reference bulk diffusion coefficient does include this correction. For a ho-

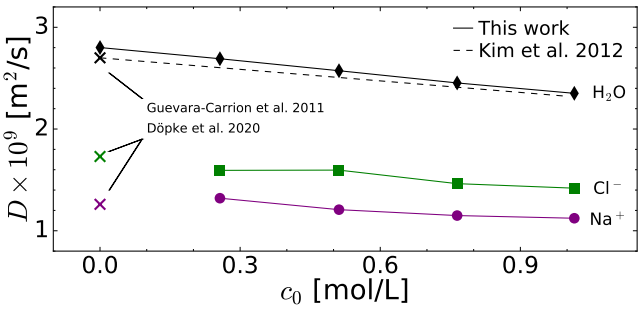

Figure 5.6: Diffusion coefficients as a function of concentration c_0 from bulk simulations containing only water and ions. The solid lines and closed symbols are from this work. The dashed line and crosses are from literature [11, 48, 242].

mogeneous system with a comparable size – our system: $L^3 = 3.5 \times 3.5 \times 6 = 74$ nm^3 -> comparable system: $L^3 = 4.2^3 = 74$ nm^3 – the finite size correction, $\xi k_B T / 6\pi\eta L$, would be in the order of 0.2×10^{-9} m^2/s (≈ 13 %) [156].

It is important to note that the horizontal leveling off of the perpendicular MSDs in the long-time limit in bins 1 to 4 (Fig. 5.8), which resemble the behavior of a solid, occurs as a result of the finite-sized bins. Particles can only leave the bins by a motion perpendicular to the surface (z-direction). Hence, all particles that remain within a given bin for extended periods of time exhibit solid-like vibrations, while the contribution of the moving particles are discarded. Consequently, only a very limited region represents the diffusive regime and can be used to obtain the perpendicular diffusion coefficients.

5.2.3. Electrokinetic Theory

The ζ-potential was evaluated for both, electro-osmosis and streaming currents using the Helmholtz-Smoluchowski theory [6, 26]. In the case of electro-osmosis, the bulk velocity was related to the ζ-potential following

$$\zeta = -\frac{\eta u_{\text{bulk}}}{\varepsilon_0 \varepsilon_r E}. \tag{5.4}$$

In the case of streaming currents, the electric flux I_{str} obtained through

$$I_{\text{str}} = \iint_{S \in \{x,y\}} \rho_e(z) u(z) \mathbf{n} ds \tag{5.5}$$

was related to the ζ-potential following

$$\zeta = -\frac{\eta}{\varepsilon_0 \varepsilon_r A_c} \frac{I_{\text{str}}}{\nabla p}. \tag{5.6}$$

A_c is the cross-sectional area of the channel (21 nm^2), with all other variables having their usual definitions.

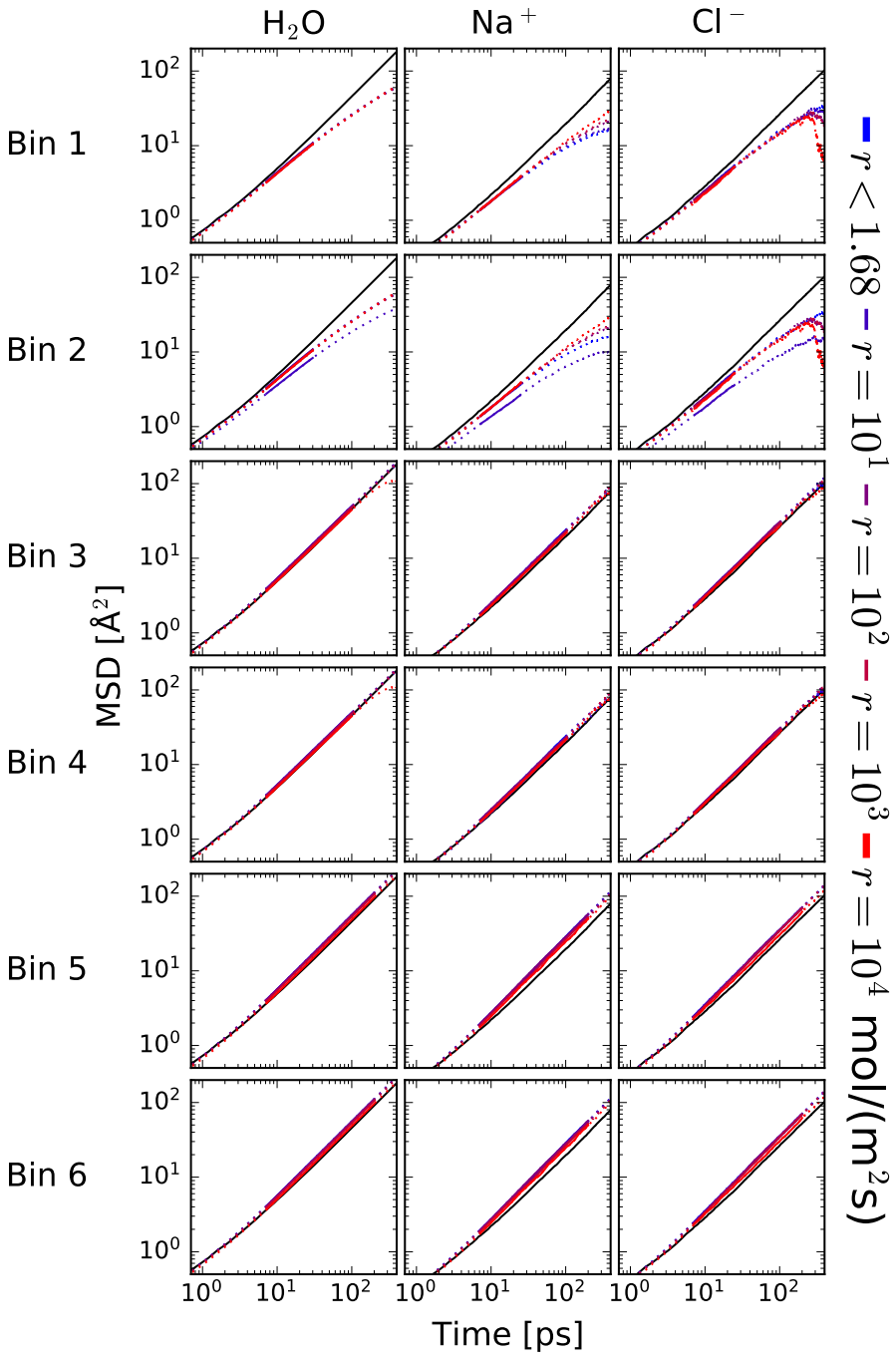

Figure 5.7: Parallel mean squared displacements (MSD) in each bin (see Fig. 5.5a for bin numbering). The black solid line is the MSD obtained from an independent bulk simulation containing only water and ions at 0.76 mol/L. The remaining solid parts denote the linear region that is used to obtain the diffusion coefficients.

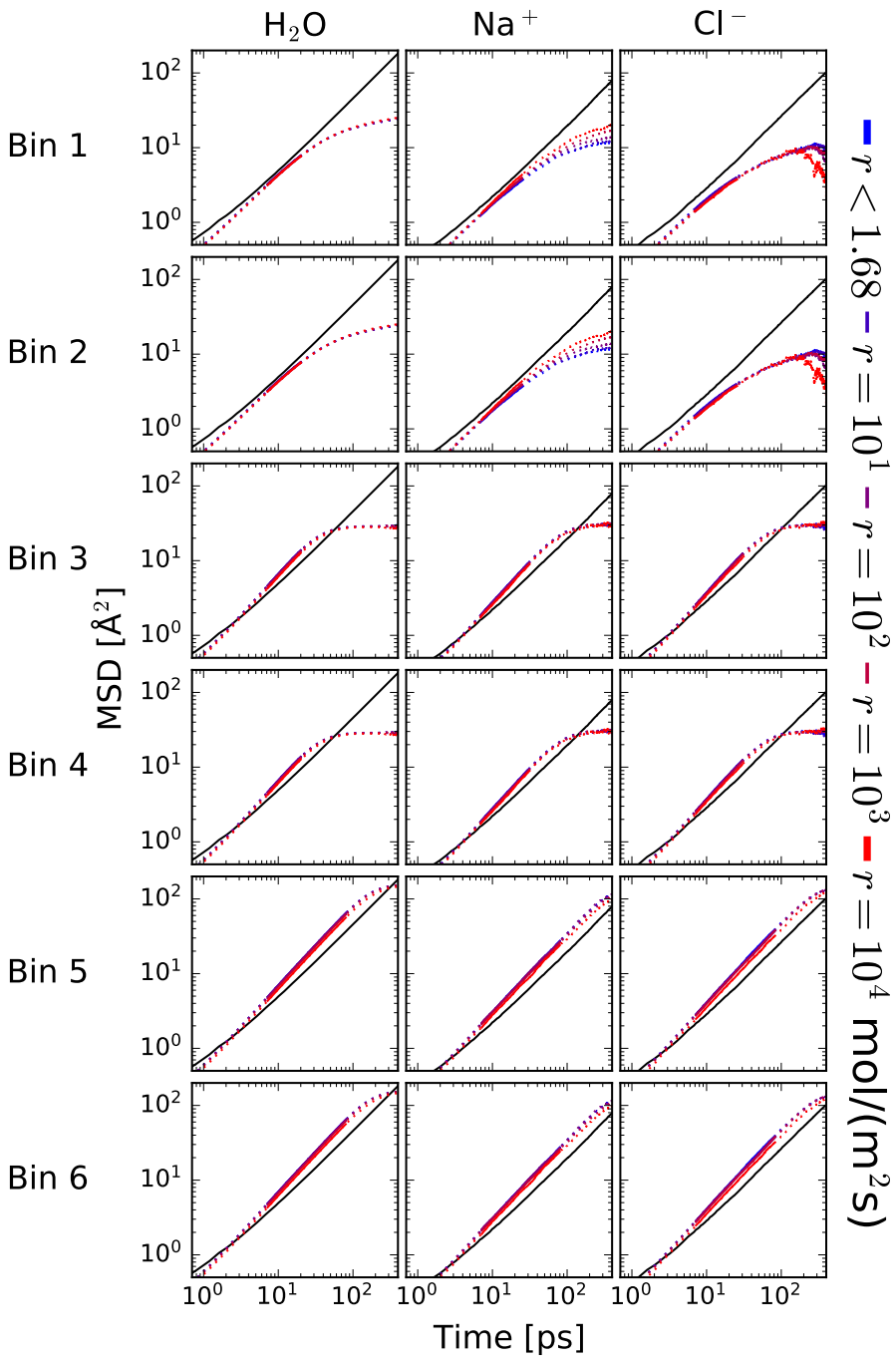

Figure 5.8: Perpendicular mean squared displacements (MSD) in each bin (see Fig. 5.5a for bin numbering). The black solid line is the MSD obtained from an independent bulk simulation containing only water and ions at 0.76 mol/L. The remaining solid parts denote the linear region that is used to obtain the diffusion coefficients.

5.3. Results

As a benchmark case, we selected a prototypical amorphous silica slit pore of approximately 6 nm height filled with a 0.66-0.74 mol/L NaCl aqueous solution at ambient conditions described above. The reaction rate r was varied between no reactions (standard non-reactive MD, equivalent to $r < 1.68$ mol/m^2/s for our simulation size/time) and $r = 10^4$ mol/m^2/s. For reference, silanol protolysis rates on silica-water interfaces were estimated in [32] to be of the order of 10^2-10^5 mol/m^2/s using dissociative MD simulations. Given the surface area [12.4 nm^2] and silanol density [4.7 SiOH/nm^2] in our system, protonation and deprotonation reactions take place between every >100 ns and 13.43 ps (see Tab. 5.1). In comparison, as will be shown later, typical Na^+ residence times are of the order of a few hundred ps so that we expect a non-negligible dependence on r.

Fig. 5.9a displays a typical cation number density profile obtained in MD simulations of silica-electrolyte interfaces. Upon increasing the protolysis reaction rate r, the cation peak in the density profile decreases, broadens and shifts away from the surface. These changes are consistent with a shift from predominantly specific to predominantly non-specific cation adsorption as demonstrated in Fig. 5.10a. In other words, for high values of r, the average time for a Na^+ ion to specifically adsorb may exceed the characteristic reprotonation time of a deprotonated site (SiO^- density/r, see Tab. 5.1). From the cation perspective, the surface charge effectively becomes more uniformly distributed as r increases. This in turn results in the reduction of specifically adsorbed cations. As expected with such less specific cation adsorption, anion adsorption is found to be less pronounced (Fig. 5.9b), while water molecules are found to orient more strongly towards the surface (Fig. 5.11b). Apart from this increased hydrophilicity, r is not found to have any other impact on the first solvation layer structure and water dynamics (Fig. 5.11). Fig. 5.9a also shows the parallel diffusion coefficients for cations (perpendicular diffusion coefficients are provided in Fig. 5.5). These data show that faster desorption and adsorption processes and the reduction of specifically adsorbed cations, as induced by higher reaction rates r, lead to faster ion dynamics in the EDL. On the one hand, non-specifically adsorbed cations are more mobile, and on the other hand, as some cations quickly desorb from a protonating SiO^- site, other cations are attracted by deprotonating SiOH sites as illustrated in Fig. 5.2b. Consequently, upon increasing the protolysis rate r, the cation diffusion coefficients near the surface increase (inset in Figs. 5.9a and 5.5b), while the average Na^+ residence time decreases (Fig. 5.12). Since barely any anions specifically adsorb, their diffusion coefficients do not show any dependence on r (Figs. 5.9b and 5.5c). Similarly, water diffusion coefficients and the fluid viscosity are found to be nearly rate independent (Figs. 5.5a and 5.11a,c).

Using the Boltzmann equation, the ion density profile can be written as $\rho(\mathbf{x}) = \rho(\infty)\exp[-\beta\mathcal{F}_r(\mathbf{x})]$, where $\beta = 1/k_BT$, $\rho(\infty)$ is the bulk density and $\mathcal{F}_r(\mathbf{x})$ is the free energy landscape corresponding to a given rate r. Considering an energy landscape possessing different adsorption sites, the density profile in z follows $\rho(z) = \left(L_xL_y\right)^{-1}\int\int\rho(\infty)\exp[-\beta\mathcal{F}_r(x,y,z)]dxdy$, where the integrals run over the surface area. This expression can be considered in two asymptotic limits depending on the reaction rate r and characteristic time τ_e over which cations relax towards lo-

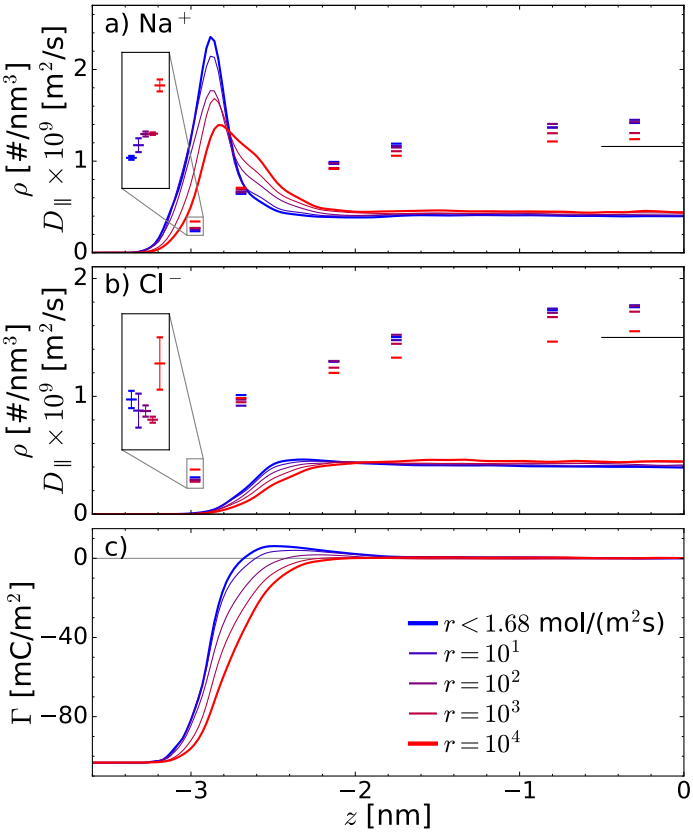

Figure 5.9: a) Na^+ and b) Cl^- density profile (lines) and parallel diffusion coefficients (symbols). Symbols in the inset are shifted on the z for clarity. The black lines display the bulk diffusion coefficients obtained from independent bulk electrolyte simulations (see Fig. 5.6). c) Screening function Γ. $z = 0$ is the channel center.

cal equilibrium. For $r\tau_e << 1$, the surface can be considered as "quenched" (non reactive). In this case, the surface contains a fraction $\alpha_\bullet$ of protonated sites MOH and a fraction $\alpha_\circ = 1 - \alpha_\bullet$ of deprotonated sites MO^- such that the density follows $\rho(z) = \rho(\infty)\langle \exp[-\beta\mathcal{F}_r(z)]\rangle$, where $\langle \exp[-\beta\mathcal{F}_r(z)]\rangle = \alpha_\bullet \exp[-\beta\mathcal{F}_\bullet(z)] + \alpha_\circ \exp[-\beta\mathcal{F}_\circ(z)]\rangle$. For $r\tau_e >> 1$, the surface can be considered as "annealed" (reactive). In this case, all surface adsorption sites are equivalent since they frequently switch between protonated and deprotonated states. The free energy of these equivalent sites is simply given by a time average $\beta\mathcal{F}_r(z) = \alpha_\bullet\beta\mathcal{F}_\bullet(z) + \alpha_\circ\beta\mathcal{F}_\circ(z)$ (we use ergodicity to replace the fraction of time spent in one site by its occurrence α). Assuming cations redistribute very fast according to the local free energy landscape, we can write the ion density as $\rho(z) = \rho(\infty)\exp[-\beta\mathcal{F}_r(z)] = \rho(\infty)\exp[-\alpha_\bullet\beta\mathcal{F}_\bullet(z) - \alpha_\circ\beta\mathcal{F}_\circ(z)]$. Provided proper boundary conditions are applied (surface charge and overall charge neutrality), these two limiting cases provide a framework to rationalize the simulated data. However, beyond such asymptotic

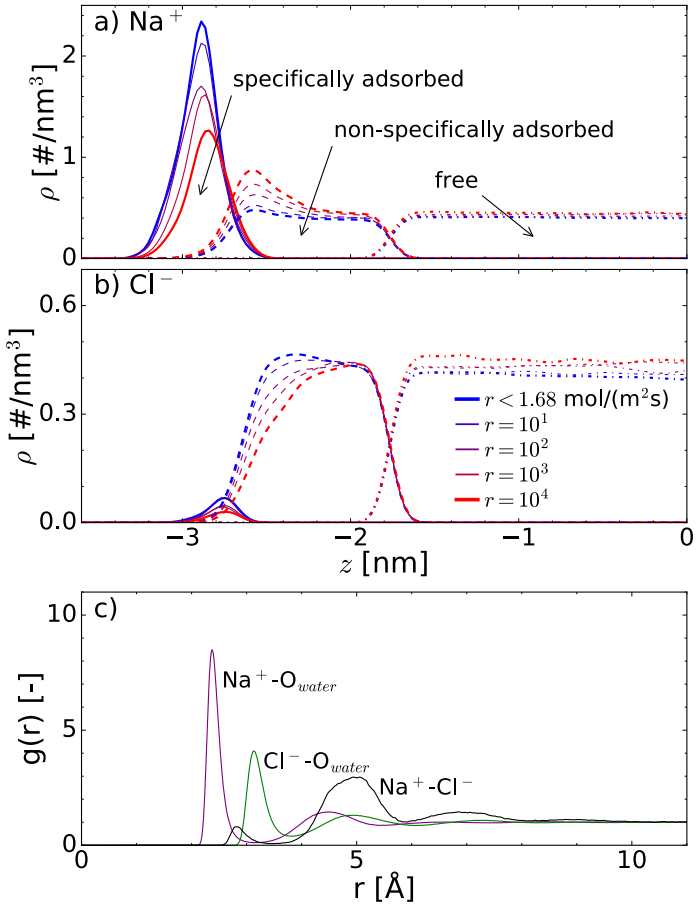

Figure 5.10: a) Na^+ and b) Cl^- density profiles from Fig. 5.9 distinguishing between the adsorption type. Specifically adsorbed when a surface atom is found within the first hydration shell (inner-sphere surface-complexes), non-specifically adsorbed ions when the first hydration shell is intact, but the ions remain under the surface influence (outer-sphere surface-complexes and ions within the diffuse layer), and free ions which present bulk behavior. Hydration shell sizes are defined by the first minima in the radial distribution functions given in c). c) Radial pair distribution functions from a bulk simulation containing only water and ions at 0.76 mol/L.

cases, obtaining an expression for intermediate reactive rates r is not straightforward as in most situations the corresponding density profile cannot be written as a single contribution (annealed surface) nor as a weighted sum of two independent contributions (quenched surface). Indeed, in these situations, the observed density profile still derives from an underlying energy profile but proper averaging that leads to $\rho(z)$ is ill defined. In particular, in such intermediate situations, there is no clear timescale separation between the relaxation time towards local equilibrium and the typical time between two protonation or deprotonation events so that one obtains density profiles that are rate dependent (in agreement with our simulation data). In

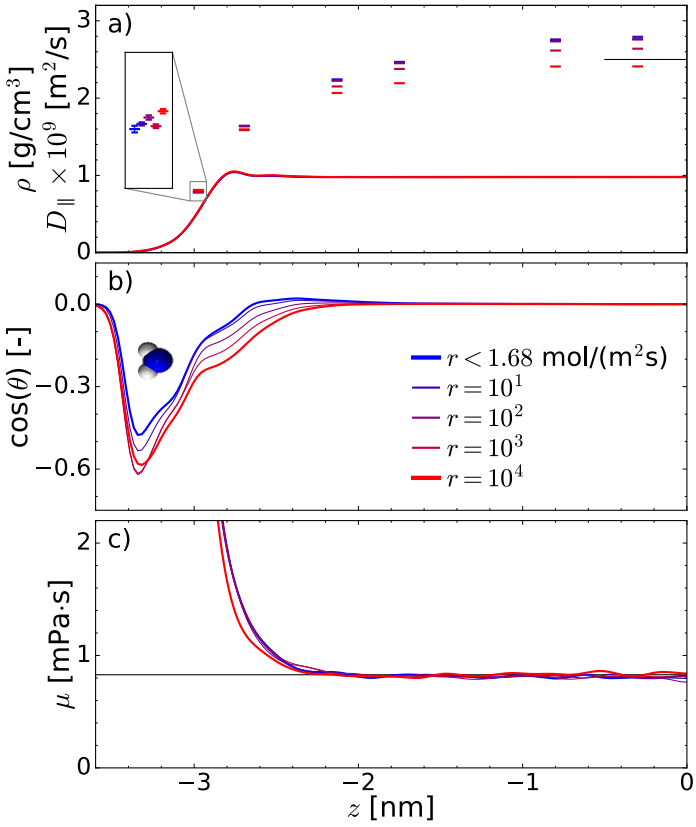

Figure 5.11: a) Water mass density profile (lines) and parallel diffusion coefficients (symbols). The black line displays the bulk diffusion coefficient obtained from independent bulk simulations containing only water and ions (see Fig. 5.6). c) Water orientation. d) Local viscosity.

the same spirit, one can see the observed density profile broadening as the result of an increased surface self-diffusivity $D_s(z)$. By writing that $D_s(z)$ corresponds to the bulk diffusivity modulated by the surface-ion interaction, one predicts that the impact of reduced surface interactions due to protolysis reactions, leads to a larger surface diffusivity [243]. In turn, such enhanced diffusivity leads to surface exploration corresponding to larger mean square displacements through the bulk phase between two relocations (re-adsorption), and hence, broader density profiles near the solid surface.

Upon increasing the reaction rate r, both ion densities increase in the channel center while the ion and water diffusion coefficients decrease (Figs. 5.9a,b, 5.11a). Although the EDL net charge is independent of r, the number of ions involved in the EDL decreases upon increasing r. In other words, cations and anions relocate in equal amounts from the EDL to the center of the channel as r increases. Such ion relocation would not notably affect the bulk ion concentration in a macroscopic channel. However, as shown in Fig. 5.1, due to the small pore height $H \approx 6$ nm (of

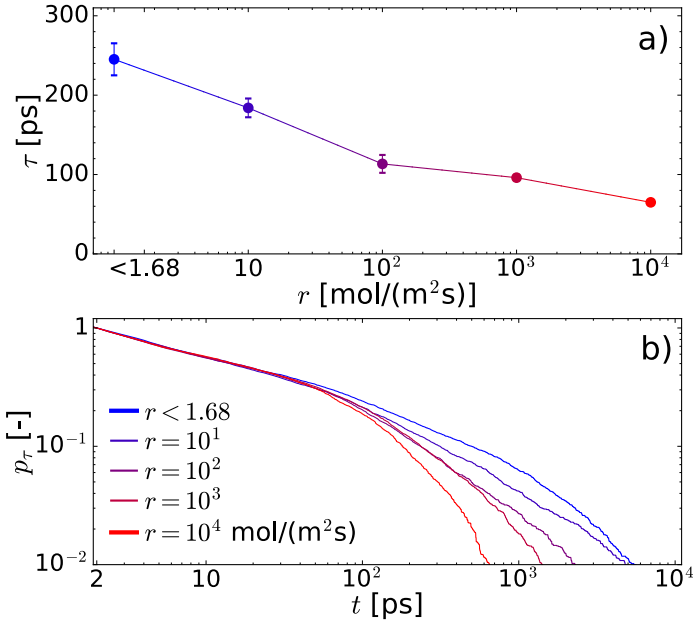

Figure 5.12: (a) Mean adsorption i.e. residence times, $\tau = \int p_\tau dt$ as a function of r. (b) Probability of adsorption p_τ given the ion is adsorbed for a minimum of 2 ps and allowing for a desorption tolerance of 2 ps.

the order of 20 times the Debye length, $\lambda_D \sim 0.35$ nm), a concentration increase from 0.66 mol/L to 0.74 mol/L can be detected when increasing r up to 10^4 mol/m^2/s. As a direct consequence of this salt concentration increase the cation, anion and water diffusion coefficients in the channel center decrease. This is in agreement with data for bulk electrolyte simulations shown in Fig. 5.6. Such an impact of the finite channel size on ion concentration and diffusion is expected to become less pronounced as λ_D/H and/or r decrease.

The ion adsorption weakening observed upon increasing r also impacts the screening of the bare surface charge density σ_0. This can best be quantified by assessing the screening function $\Gamma(z) = \sigma_0 + \int_{-\infty}^{z} e\left(\rho_{\mathrm{Na^+}}(z') - \rho_{\mathrm{Cl^-}}(z')\right) \mathrm{d}z$. As expected from the change from specific to non-specific ion adsorption upon increasing r, the screening peak in Fig. 5.9b shifts away from the surface and decreases in magnitude (the peak even disappears for the fastest reaction rates). Surface reaction kinetics can, thus, directly impact the occurrence of charge inversion ($\Gamma > 0$). This result can explain why many MD studies – carried out with a static surface charge distribution – report charge inversion under conditions for which no experimental charge inversion is found [23, 54, 130]. Another reason for such disagreement between MD simulations and experiments may be force field shortcomings as investigated in our recent work [26].

We have thus far shown that reaction kinetics can significantly impact ion adsorption, diffusion and screening of the bare surface charge. Based on these results, a

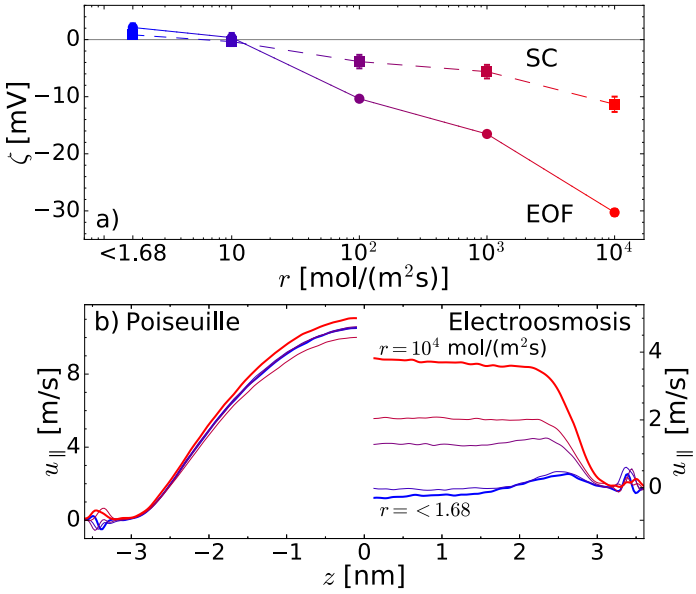

Figure 5.13: a) ζ-potential as a function of reaction rate r from streaming current (SC) and electro-osmosis (EOF) simulations. b) Poiseuille (left) and electro-osmosis (right) flow profiles resulting from a pressure drop of 75 atm and an electric field of 0.2 V/nm. These external forces have been shown to be within the linear response regime [26, 130].

strong impact of protolysis reactions on electrokinetic properties is expected. For example, the ζ-potential in Fig. 5.13a is found to decrease with increasing reaction rate r. This result can be explained from changes in the ion density distributions $\rho_{Na^+}(z)$ and $\rho_{Cl^-}(z)$ within the EDL (Figs. 5.9a,b). These distributions directly impact the measured streaming current $I_{str} \sim \int e\left(\rho_{Na^+}(z') - \rho_{Cl^-}(z')\right) u_x dz$ and electroosmotic flow $\eta\nabla^2 u_{\parallel}(z) = e\left(\rho_{Na^+}(z) - \rho_{Cl^-}(z)\right) E_x$, which, in turn, fully determine the ζ-potential through $\zeta \sim I_{str}/\Delta p_x$ and $\zeta \sim u_{\parallel,bulk}/E_x$ (following the Helmholtz-Smoluchowski theory). In other words, protolysis reactions directly influence the electrokinetic response through ion adsorption. Although the dependence of the ζ-potential on the reaction kinetics in Fig. 5.13a appears to be stronger for electro-osmosis than for streaming currents, the ion distributions corresponding to both methods are identical to those shown in Figs. 5.9a,b. Hence, the differences in ζ-potential between electro-osmosis and streaming currents must originate from within the Helmholtz-Smoluchowski theory. In fact, in agreement with previous studies [26–28], these differences vanish when $\zeta \to 0$, which occurs at a rate around 10 mol/m^2/s. It is noteworthy that, since the Poiseuille flow depends mostly on fluid properties at the center of the channel, the velocity profiles corresponding to the streaming currents shown in the left of Fig. 5.13b are independent of r. Conversely, the electroosmotic flow profiles, which are fully determined by the ion distribution within the EDL (following Navier-Stokes equation), change even qualitatively with r as shown in the right of Fig. 5.13b.

5.4. Conclusions

In conclusion, we developed a novel framework to account for surface reactions in classical MD simulations at no additional cost compared to non-reactive MD simulations. We then used this method to demonstrate that EDL properties and electrokinetic transport in a silica channel do not just depend on the static surface properties but also on proton exchange reaction kinetics. While such kinetic chemical events are not taken into consideration in available formalisms, we provide strong evidence that such processes affect both the static and dynamic properties of ions and solvent (water) within porous materials. Specifically, upon increasing the surface reaction kinetics (from no reactivity to rates encountered in experiments), cation adsorption at the negatively charged surface becomes less pronounced with decreased retention times. In turn, such decreased adsorption leads to increased local diffusion coefficients near the solid surface. These changes in the ion distribution and dynamics within the EDL also directly impact electrokinetic phenomena with – for instance – the ζ-potential reducing upon increasing the protolysis reaction rate. The quantitative and qualitative differences observed between non-reactive and reactive surface charge distributions suggest that such equilibrium surface reactions play an even more important role for the EDL structure and dynamics than has thus far been assumed. In fact, the impact of surface reactivity may even be more pronounced for surface groups with weaker covalent bonds, at higher temperature, lower pH, or for ions with longer residence times, questioning the near-universal neglect of protolysis reactions in simulation and modeling endeavours. Finally, our novel framework provides a stepping stone for more realistic interface modeling within a MD environment, potentially benefiting applications ranging from the design of anti-corrosion paints to electrochemical cells. Additional work should also include establishing a bridge between our method and fundamental approaches in which proton creation and diffusion at surfaces is probed [244]. In this context, mesoscopic strategies such as those based on the formalism of intermittent Brownian motion applied to surface adsorption and relocation in pores could prove useful in linking molecular aspects and macroscopic observations [243]. Moreover, to bridge the gap between the microscopic and mesoscopic scales, the inclusion of water ionization reactions from reactive simulations could provide a means to account for chemical events occurring at the fs time scale.

6

Conclusions

Molecular Dynamics (MD) simulations provide a powerful bottom-up approach to gain detailed atomic level insight at time- and length-scales where experimental techniques struggle or can only get partial information. It is thus crucial, to design simulations to realistically reproduce the physics at play. The most important aspects of MD simulations, can thus be said to be the force field development and results validation. The first of these aspects, force field development, has received a lot of attention in the last decades. Force fields have been developed for a multitude of different systems (proteins, colloids, water, minerals, ...) and properties (protein folding, colloidal stability, freezing of water, calcite formation, ...), their ability to reproduce systems and properties different to those initially intended however is questionable. Most authors, simply take force fields out of their designed for purposes and expect realistic results. While this approach may be reasonable in some instances, for complex systems such as interfaces, the results between MD simulations performed with different force fields vary wildly. It is no surprise, that for example combining two force fields optimized to reproduce bulk solid properties and bulk fluid properties, respectively, do not necessarily reproduce realistic ion adsorption and/or hydrophobicity. The intricacies of realistically reproducing interfacial properties and phenomena are in fact very sensitive to the specifics of the system and the balance between competing interactions. Force fields used to represent interface systems, should thus be optimized explicitly for the interface, ideally at relevant system conditions and for specifically desired properties of interest. This task however, is hindered by the severe lack of representative experimental data of interfacial phenomena that can be used constructively in force field development and optimization. Reliable optimization, validation and improvement of the representation of interfaces is thus severely lacking. In an attempt to bridge this gap, this dissertation follows a journey from evaluating the force field mix-and-match approach common for electrolytes (Ch. 2) through the evaluation of such mixed-and-matched force fields in terms of competitive ion adsorption (Ch. 3) to the optimization and validation of MD results at the interface (Ch. 4) and the development of a novel scheme to include relevant surface

reactions (Ch. 5).

In Ch. 2 it was found that in fact, the mix-and-match approach is reasonable at infinite dilution (single ion in water), with the water model dominating the overall fluid properties. As the ionic concentration increased however, the validity of mixing-and-matching deteriorated quickly, with ion pairing, thus formation of crystals in the fluid, being the main inconsistency with experimental results. When accounting for the fluid dielectric screening by scaling the ionic charges according to the Electronic Continuum Correction (ECC) idea, crystal formation could be reduced. Force fields including ECC in fact offered the most consistent and best results across the board at finite concentrations. Strictly speaking however, ECC is only valid in homogeneous systems with a continuous dielectric.

Thus we initially hesitated in using ECC for an interface system, which is inherently heterogeneous, for example, silica has a relative permittivity of approximately 4 and an electrolyte has a relative permittivity of approximately 80 depending on concentration and conditions. In Ch. 3 we thus stuck to the conventional full charges when investigating the ion-specificity on an amorphous silica surface in contact with a NaCl–$CaCl_2$ solution. Nonetheless, in Ch. 4 we revisited ECC in an interfacial system, and showed that also in such a heterogeneous system, ECC can be applied successfully.

Investigating the adsorption behavior of Na^+ and Ca^{2+} on amorphous silica in Ch. 3, it was found that the local surface structure, can sterically hinder an ion from adsorbing based on said ions hydration properties. For example, at adsorption sites deep into the surface, Na^+ ions adsorbed preferably due to their smaller hydration shell sizes, while at adsorption sites sticking out of th surface Ca^{2+} ions adsorbed preferentially owing to their larger coulombic charge. While this phenomenon has not been reported in experimental results, membranes that separate ions based on ion-size and/or hydration shell size for example, already exist. Our finding may thus provide a viable explanation for the sometimes counter-intuitive preferential adsorption that can be observed in some experimental studies.

The lingering doubt on whether our simulation accurately represent the physics at play however, rendered us to take an extra step to really validate our simulation results and to get greater certainty of the observed behavior. Thus, we searched for an experimentally measurable and in the simulation reproduceable property, specific to the interaction between the fluid and solid at the interface. On this quest, we noticed the good agreement between electro-osmosis and streaming current/potential experiments when the ζ-potential is zero. While this agreement may seem logical, it is in fact quite contrasting with the typically large differences measured in ζ-potentials between these methods when $\zeta \neq 0$. From the Helmholtz-Smoluchowski theory it became clear that the relationship between the ζ-potential and measured property in these experiments is linear with only a multiplicative constant depending which depends on for example the fluid viscosity, dielectric permittivity and/or channel size. In Ch. 4, it is thus shown that when the ζ-potential is zero, it is zero irregardless of the experimental electrokinetic method (electro-osmosis and/or streaming current/potential), and irregardless of many fluid and system properties. As such, the conditions at which $\zeta = 0$ provide a unique opportunity to compare simulations and

experiments. Exploiting this unique opportunity, we then propose a simple modification to the ion-surface interaction parameters to reproduce the experimental conditions at which the ζ potential is zero, thereby, building a symbiotic relationship between experiments and simulations. Experiments providing the macroscopic property against which the simulation is validated, increasing its trustworthiness, and simulations giving atomic level detail unavailable in experiments. While in Ch. 4 this validation method is shown for a $CaCl_2$ solution in contact with amorphous silica, by varying the pH and concentration of any solution in contact with any surface, an infinite number of conditions at which $\zeta = 0$ can be found. Thus opening the doors towards rigorously optimizing MD simulation of interfaces and obtaining with certainty atomic level detail of the interfacial phenomena. This approach should not be seen as a stand alone however, since the initial force field development and selection are also crucial to the accurate representation of the physics.

An additional consideration when dealing with interfaces is whether the current framework of simulation includes all relevant effects. For example, oxide surfaces tend of have continuous protonation and deprotonation reactions changing the surface properties locally. In classical MD simulations, these are not accounted for, and reactive MD simulations remain prohibitively expensive for larger systems and properties that require longer simulation times. We therefore devised a method, presented in Ch. 5, to effectively mimic these reactions in classical MD simulations at no additional computational cost. Essentially, surface reactions are mimicked by turning on and off proton interactions, without explicitly adding or removing the atom, and adjusting the respective surrounding atom parameters, in such a way that no explicit bond creating nor breaking are necessary. Using this approach it is found that the inclusion of protolysis reactions can hugely lower ion adsorption and residence times in the interfacial region. Even equilibrium reaction rates predicted in previous studies for silica surfaces, had a non-negligible impact. This finding provides strong evidence, that the near universal neglect of these surface reactions in classical MD simulations is unjustified. Especially when dealing with high temperatures, ions with long residence times and/or near dissolution conditions. For future works, this groundbreaking chapter describes a concept on how to include surface reactions in a simple yet computational cost effective manner, opening doors for a better understanding of the interface. This can be used in for example evaluating adsorption energies at different reaction rates or investigate the impact protolysis reactions have on ions competing to adsorb.

Combining the individual findings of this dissertation, it can be concluded that MD simulations of interfaces can be an invaluable asset to complement experiments and to offer new insights at time and length scales not accessible to experiments. It takes however a skilled person with great diligence to master so many different aspects to obtain realistic and relevant results. **First**, a careful force field selection needs to be performed, for which in many cases there is no precedent, and thus the best selection is yet to be known. An initial force field performance may be assessed on individual ion performance, but it is also crucial to determine, whether for example, the ratio of hydration properties for electrolyte mixtures is realistic, and if all the relevant surface phenomena are included, such as the protolysis reactions discussed in Ch.

5. Additionally, consideration should be given to accounting electronic polarization, either explicitly via a polarizable fore field (high computational cost), or implicitly via charge scaling following the ECC teachings (low computational cost). While the use of ECC in heterogeneous systems remains debated, in this thesis no deterioration of the physics was observed when using charge scaling. Additional force field tuning, in combination with ECC may however be necessary. **Second**, adsorption at the interface needs to be tuned. Most importantly interfacial phenomena from a microscopic perspective are not yet fully understood and known. Methods such the one presented here in Ch. 4 are thus a *must* to obtain results with any certainty. When following this diligent approach, simulations may provide great insights not available to current experimental methods, but the results will only be as good as the model, the force field optimization and the results validation allow. There is thus a long road ahead, but we have already gotten very far, so I look with optimism into the future of simulating interfaces using Molecular Dynamics.

For the future, I recommend to continue working on a symbiotic relationship between experiments, simulations and modelling. Currently, these groups are too often separated and the results they produce run past each other without any impact. I strongly believe that there is more need for collaboration and particularly accross different disciplines and groups. A simple idea in one scientific field, may be ground breaking when applied to another. To pick the fruits from combining the knowledge of multiple disciplines however, requires in depth knowledge of each of these disciplines, and fruitful collaborations. We thus need multidisciplinary researchers with good knowledge in many fields, as well as experts in a single field. For example, MD simulations may thus provide atomistic insights into local properties at the interface, which may potentially be verified and validated with experiments and subsequently used to improve continuum models in which interface properties are typically assumed to be constant and equal to bulk properties.

As a specific example for the future, one could consider the relative permittivity. This property is typically considered to be constant throughout the fluid phase, yet it is known to vary locally near the interface. Verified and validated molecular simulations could provide insight into these local variations, which may subsequently be used to derive a functional form suitable for continuum models. In order to get started along this train of thought I see the following important steps: a) optimize and/or validate a molecular simulation force field for an aqueous electrolyte-solid interface; b) calculate the local dielectric permittivity from the MD simulations and potentially determine (empirically) a functional form; c) expand and/or re-derive the theoretical framework in continuum modelling to include the possibility of a locally varying dielectric permittivity; d) analyze continuum modelling results with a locally varying dielectric permittivity and validate the results with experiments. In this manner, a circle can be closed, in which the real physics are considered at every step from experiments, while at the same time the knowledge from smaller time- and length-scales is carried over to larger time- and length-scales.

References

[1] R. Hartkamp, A. L. Biance, L. Fu, J. F. Dufrêche, O. Bonhomme, and L. Joly, *Measuring Surface Charge: Why Experimental Characterization and Molecular Modeling Should Be Coupled,* Curr. Opin. Colloid Interface Sci. **37**, 101 (2018).

[2] D. C. Grahame, *The Electrical Double Layer and the Theory of Electrocapillarity,* Chem. Rev. **41**, 441 (1947).

[3] J. Lyklema, *Fundamentals of Interface and Colloid Science: Soft Colloids*, Vol. 5 (Elsevier, 2005).

[4] N. Bloembergen, *Nonlinear Optics and Spectroscopy,* Rev. Mod. Phys. **54**, 685 (1982).

[5] G. Binnig, C. F. Quate, and C. Gerber, *Atomic Force Microscope,* Phys. Rev. Lett. **56**, 930 (1986).

[6] A. Delgado, F. González-Caballero, R. Hunter, L. Koopal, and J. Lyklema, *Measurement and Interpretation of Electrokinetic Phenomena,* J. Colloid Interface Sci. **309**, 194 (2007).

[7] P. W. Atkins and R. S. Friedman, *Molecular Quantum Mechanics* (Oxford university Press, 2011).

[8] M. P. Allen and D. J. Tildesley, *Computer Simulation of Liquids*, Vol. 1 (Oxford University Press, New York, NY, USA, 2017).

[9] H. J. C. Berendsen, J. P. M. Postma, W. F. van Gunsteren, A. DiNola, and J. R. Haak, *Molecular Dynamics With Coupling to an External Bath,* J. Chem. Phys. **81**, 3684 (1984).

[10] G. J. Martyna, D. J. Tobias, and M. L. Klein, *Constant Pressure Molecular Dynamics Algorithms,* J. Chem. Phys. **101**, 4177 (1994).

[11] M. F. Döpke, O. A. Moultos, and R. Hartkamp, *On the Transferability of Ion Parameters to the TIP4P/2005 Water Model Using Molecular Dynamics Simulations,* J. Chem. Phys. **152**, 024501 (2020).

[12] H. J. C. Berendsen, J. R. Grigera, and T. P. Straatsma, *The Missing Term in Effective Pair Potentials,* J. Phys. Chem. **91**, 6269 (1987).

[13] P. G. Kusalik and I. M. Svishchev, *The Spatial Structure in Liquid Water,* Science **265**, 1219 (1994).

[14] W. L. Jorgensen, J. Chandrasekhar, J. D. Madura, R. W. Impey, and M. L. Klein, *Comparison of Simple Potential Functions for Simulating Liquid Water,* J. Chem. Phys. **79**, 926 (1983).

[15] H. W. Horn, W. C. Swope, J. W. Pitera, J. D. Madura, T. J. Dick, G. L. Hura, and T. Head-Gordon, *Development of an Improved Four-Site Water Model for Biomolecular Simulationss: TIP4P-Ew,* J. Chem. Phys. **120**, 9665 (2004).

[16] J. L. F. Abascal and C. Vega, *A General purpose Model for the Condensed phases of Water: TIP4P/2005,* J. Chem. Phys. **123**, 234505 (2005).

[17] D. E. Smith and L. X. Dang, *Computer Simulations of NaCl Association in Polarizable Water,* J. Chem. Phys. **100**, 3757 (1994).

[18] I. S. Joung and T. E. Cheatham, *Determination of Alkali and Halide Monovalent Ion Parameters for Use in Explicitly Solvated Biomolecular Simulations,* J. Phys. Chem. B **112**, 9020 (2008).

[19] S. Mamatkulov, M. Fyta, and R. R. Netz, *Force Fields for Divalent Cations Based on Singel-Ion and Ion-Pair Properties,* J. Chem. Phys. **138**, 024505 (2013).

[20] P. Li, L. F. Song, and K. M. Merz, *Parameterization of Highly Charged Metal Ions Using the 12-6-4 LJ-Type Nonbonded Model in Explicit Water,* J. Phys. Chem. B **119**, 883 (2015).

[21] A. L. Benavides, M. A. Portillo, V. C. Chamorro, J. R. Espinosa, J. L. F. Abascal, and C. Vega, *A Potential Model for Sodium Chloride Solutions Based on the TIP4P/2005 Water Model,* J. Chem. Phys. **147**, 104501 (2017).

[22] I. Zeron, J. Abascal, and C. Vega, *A Force Field of Li^+, Na^+, K^+, Mg^{2+}, chCa2+, Cl^-, and SO_4^{2-} in Aqueous solution Based on the TIP4P/2005 Water Model and Scaled Charges for the Ions,* J. Chem. Phys. **151**, 134504 (2019).

[23] M. F. Döpke, J. Lützenkirchen, O. A. Moultos, B. Siboulet, J.-F. Dufrêche, J. T. Padding, and R. Hartkamp, *Preferential Adsorption in Mixed Electrolytes Confined by Charged Amorphous Silica,* J. Phys. Chem. C **123**, 16711 (2019).

[24] K. Vollmayr, W. Kob, and K. Binder, *Cooling-Rate Effects in Amorphous Silica: A Computer-Simulation Study,* Phys. Rev. B **54**, 15808 (1996).

[25] J. Lützenkirchen, T. Preočanin, D. Kovačević, V. Tomišić, L. Lövgren, and N. Kallay, *Potentiometric Titrations as a Tool for Surface Charge Determination,* Croat. Chem. Acta **85**, 391 (2012).

[26] M. F. Döpke and R. Hartkamp, *The Importance of Specifically Adsorbed Ions for Electrokinetic Phenomena: Bridging the Gap Between Experiments and MD Simulations,* J. Chem. Phys. **154**, 094701 (2021).

[27] A. Szymczyk, P. Fievet, M. Mullet, J. Reggiani, and J. Pagetti, *Comparison of Two Electrokinetic Methods - Electroosmosis and Streaming Potential - to Determine the Zeta-Potential of Plane Ceramic Membranes,* J. Membr. Sci. **143**, 189 (1998).

[28] G. Hurwitz, G. R. Guillen, and E. M. Hoek, *Probing Polyamide Membrane Surface Charge, Zeta Potential, Wettability, and Hydrophilicity With Contact Angle Measurements,* J. Membr. Sci. **349**, 349 (2010).

[29] M. F. Döpke, F. Westerbaan van der Meij, B. Coasne, and R. Hartkamp, *Surface Protolysis and Its Kinetics Impact the Electrical Double Layer,* Phys. Rev. Lett. **128**, 056001 (2022).

[30] M. Nogami, R. Nagao, and C. Wong, *Proton Conduction in Porous Silica Glasses With High Water Content,* J. Phys. Chem. B **102**, 5772 (1998).

[31] N. Amdursky, Y. Lin, N. Aho, and G. Groenhof, *Exploring Fast Proton Transfer Events Associated With Lateral Proton Diffusion on the Surface of Membranes,* Proc. Natl. Acad. Sci. U.S.A. **116**, 2443 (2019).

[32] G. K. Lockwood and S. H. Garofalini, *Proton Dynamics at the Water–Silica Interface via Dissociative Molecular Dynamics,* J. Phys. Chem. C **118**, 29750 (2014).

[33] T. S. Mahadevan and J. Du, *Hydration and Reaction Mechanisms on Sodium Silicate Glass Surfaces From Molecular Dynamics Simulations With Reactive Force Fields,* J. Am. Ceram. Soc. **103**, 3676 (2020).

[34] T. A. Ho and A. Striolo, *Promising Performance Indicators for Water Desalination and Aqueous Capacitors Obtained by Engineering the Electric Double Layer in Nano-Structured Carbon Electrodes,* J. Phys. Chem. C **119**, 3331 (2015).

[35] A. Striolo, A. Michaelides, and L. Joly, *The Carbon-Water Interface: Modeling Challenges and Opportunities for the Water-Energy Nexus,* Annu. Rev. Chem. Biomol. Eng. **7**, 533 (2016).

[36] V. Prasad, S. K. Kannam, R. Hartkamp, and S. P. Sathian, *Water Desalination Using Graphene Nanopores: Influence of the Water Models Used in Simulations,* Phys. Chem. Chem. Phys. **20**, 16005 (2018).

[37] J. L. Aragones, M. Rovere, C. Vega, and P. Gallo, *Computer Simulation Study of the Structure of LiCl Aqueous Solutions: Test of Non-Standard Mixing Rules in the Ion Interaction,* J. Phys. Chem. B **118**, 7680 (2014).

[38] F. Moučka and I. Nezbeda, *Water–methanol Mixtures With Non-Lorentz–Berthelot Combining Rules: A Feasibility Study,* J. Mol. Liq. **159**, 47 (2011).

[39] C. Vega and E. de Miguel, *Surface Tension of the Most Popular Models of Water by Using the Test-Area Simulation Method,* J. Chem. Phys. **126**, 154707 (2007).

[40] C. Vega and J. L. F. Abascal, *Simulating Water With Rigid Non-Polarizable Models: a General Perspective,* Phys. Chem. Chem. Phys. **13**, 19663 (2011).

[41] J. Wang, R. M. Wolf, J. W. Caldwell, P. A. Kollman, and D. A. Case, *Development and Testing of a General Amber Force Field,* J. Comput. Chem. **25**, 1157 (2004).

[42] K. Vanommeslaeghe, E. Hatcher, C. Acharya, S. Kundu, S. Zhong, J. Shim, E. Darian, O. Guvench, P. Lopes, I. Vorobyov, and A. D. Mackerell Jr., *CHARMM General Force Field: A Force Field for Drug-Like Molecules Compatible With the CHARMM All-Atom Additive Biological Force Fields,* J. Comput. Chem. **31**, 671 (2010).

[43] J. Alejandre, G. A. Chapela, F. Bresme, and J.-P. Hansen, *The Short Range Anion-H Interaction is the Driving Force for Crystal Formation of Ions in Water,* J. Chem. Phys. **130**, 174505 (2009).

[44] V. Mile, O. Gereben, S. Kohara, and L. Pusztai, *On the Structure of Aqueous cesium bromide Solutions: Diffraction Experiments, Molecular Dynamics Simulations and Reverse Monte Carlo Modeling,* J. Mol. Liq. **157**, 36 (2010).

[45] N. Modi, P. R. Singh, K. R. Mahendran, R. Schulz, M. Winterhalter, and U. Kleinekathöfer, *Probing the Transport of Ionic Liquids in Aqueous Solution Through Nanopores,* J. Phys. Chem. Lett. **2**, 2331 (2011).

[46] A. Pérez and A. Rubio, *A Molecular Dynamics Study of Water Nucleation Using the TIP4P/2005 Model,* J. Chem. Phys. **135**, 244505 (2011).

[47] F. Moučka, M. Lísal, and W. R. Smith, *Molecular Simulation of Aqueous Electrolyte Solubility. 3. Alkali-Halide Salts and their Mixtures in Water and in Hydrochloric Acid,* J. Phys. Chem. B **116**, 5468 (2012).

[48] J. S. Kim, Z. Wu, A. R. Morrow, A. Yethiraj, and A. Yethiraj, *Self-Diffusion and Viscosity in Electrolyte Solutions,* J. Phys. Chem. B **116**, 12007 (2012).

[49] J. L. Aragones, E. Sanz, and C. Vega, *Solubility of NaCl in Water by Molecular Simulations Revisited,* J. Chem. Phys. **136**, 244508 (2012).

[50] Z. R. Kann and J. L. Skinner, *A Scaled-Ionic-Charge Simulation Model that Reproduces Enhanced and Suppressed Water Diffusion in Aqueous Salt Solutions,* J. Chem. Phys. **141**, 104507 (2014).

[51] J. C. Neyt, A. Wender, V. Lachet, A. Szymczyk, A. Ghoufi, and P. Malfreyt, *How does the Electronic Continuum Model Perform in the Prediction of the Surface Tension of Salt Solutions?* Chem. Phys. Lett. **595-596**, 209 (2014).

[52] E. Pluhařová, H. E. Fischer, P. E. Mason, and P. Jungwirth, *Hydration of the Chloride Ion in Concentrated Aqueous Solutions Using Neutron Scattering and Molecular Dynamics,* Mol. Phys. **112**, 1230 (2014).

[53] R. Hartkamp and B. Coasne, *Structure and Transport of Aqueous Electrolytes: From Simple Halides to Radionuclide Ions,* J. Chem. Phys. **141**, 124508 (2014).

[54] R. Hartkamp, B. Siboulet, J.-F. Dufrêche, and B. Coasne, *Ion-Specific Adsorption and Electroosmosis in Charged Amorphous Porous Silica,* Phys. Chem. Chem. Phys. **17**, 24683 (2015).

[55] M. Ding, A. Szymczyk, and A. Ghoufi, *On the Structure and Rejection of Ions by a Polyamide Membrane in Pressure-driven Molecular Dynamics Simulations,* Desalination **368**, 76 (2015).

[56] M. B. Singh, V. H. Dalvi, and V. G. Gaikar, *Investigations of Clustering of Ions and Diffusivity in Concentrated Aqueous Solutions of Lithium Chloride by Molecular Dynamic Simulations,* RSC Adv. **5**, 15328 (2015).

[57] M. Kohagen, P. E. Mason, and P. Jungwirth, *Accounting for Electronic Polarization Effects in Aqueous Sodium Chloride via Molecular Dynamics Aided by Neutron Scattering,* J. Phys. Chem. B **120**, 1454 (2016).

[58] L. Liu and G. N. Patey, *A Molecular Dynamics Investigation of the Influence of Water Structure on Ion Conduction Through a Carbon Nanotube,* J. Chem. Phys. **146**, 074502 (2017).

[59] R. Sivakumarasamy, R. Hartkamp, B. Siboulet, J.-F. Dufrêche, K. Nishiguchi, A. Fujiwara, and N. Clément, *Selective Layer-Free Blood Serum Ionogram Based on Ion-specific Interactions With a Nanotransistor,* Nat. Mater. **17**, 464 (2018).

[60] M. Nguyen and S. W. Rick, *The Influence of polarizability and Charge Transfer on Specific Ion Effects in the Dynamics of Aqueous Salt Solutions,* J. Chem. Phys. **148**, 222803 (2018).

[61] T. R. Underwood and H. C. Greenwell, *The Water-Alkane Interface at Various NaCl Salt Concentrations: a Molecular Dynamics Study of the Readily Available Force Fields,* Sci. Rep. **8**, 352 (2018).

[62] M. H. Köhler, J. R. Bordin, and M. C. Barbosa, *2D Nanoporous Membrane for cation removal From Water: Effects of Ionic Valence, Membrane Hydrophobicity, and Pore Size,* J. Chem. Phys. **148**, 222804 (2018).

[63] M. H. Köhler, J. R. Bordin, and M. C. Barbosa, *Ion flocculation in Water: From bulk to Nanoporous Membrane Desalination,* J. Mol. Liq. **277**, 516 (2019).

[64] W. Li and Z. Jin, *Effect of Ion Concentration and Multivalence on Methane-brine Interfacial Tension and Phenomena From Molecular Perspectives,* Fuel **254**, 115657 (2019).

[65] Y. Wu, H. L. Tepper, and G. A. Voth, *Flexible Simple Point-Charge Water Model With Improved Liquid-State Properties,* J. Chem. Phys. **124**, 024503 (2006).

[66] W. L. Jorgensen, D. S. Maxwell, and J. Tirado-Rives, *Development and Testing of the OPLS All-Atom Force Field on Conformational Energetics and Properties of Organic Liquids,* J. Am. Chem. Soc. **118**, 11225 (1996).

[67] A. L. Benavides, J. L. Aragones, and C. Vega, *Consensus on the Solubility of NaCl in Water From Computer Simulations Using the Chemical Potential Route,* J. Chem. Phys. **144**, 124504 (2016).

[68] A. Benavides, M. Portillo, J. Abascal, and C. Vega, *Estimating the Solubility of 1:1 Electrolyte Aqueous Solutions: the Chemical Potential Difference Rule,* Mol. Phys. **115**, 1301 (2017).

[69] I. V. Leontyev and A. A. Stuchebrukhov, *Electronic Continuum Model for Molecular Dynamics Simulations,* J. Chem. Phys. **130**, 085102 (2009).

[70] I. Leontyev and A. Stuchebrukhov, *Accounting for Electronic polarization in Non-Polarizable Force Fields,* Phys. Chem. Chem. Phys. **13**, 2613 (2011).

[71] M. Vazdar, E. Pluhařová, P. E. Mason, R. Vácha, and P. Jungwirth, *Ions at Hydrophobic Aqueous Interfaces: Molecular Dynamics With Effective Polarization,* J. Phys. Chem. Lett. **3**, 2087 (2012).

[72] E. E. Bruce and N. F. A. van der Vegt, *Does an Electronic Continuum correction Improve Effective Short-Range Ion-Ion Interactions in Aqueous solution?* J. of Chem. Phys. **148**, 222816 (2018).

[73] A. Nikitin and G. Del Frate, *Development of Nonbonded Models for Metal Cations Using the Electronic Continuum Correction,* J. Comput. Chem. **40**, 2464 (2019).

[74] J. Åqvist, *Ion-Water Interaction Potentials Derived From Free Energy Perturbation Simulations,* J. Phys. Chem. **94**, 8021 (1990).

[75] D. Horinek, S. I. Mamatkulov, and R. R. Netz, *Rational Design of Ion Force Fields Based on Thermodynamic Solvation Properties,* J. Chem. Phys. **130**, 124507 (2009).

[76] S. Mamatkulov and N. Schwierz, *Force Fields for Monovalent and Divalent Metal Cations in TIP3P Water Based on Thermodynamic and Kinetic Properties,* J. Chem. Phys. **148**, 074504 (2018).

[77] G. A. Orozco, O. A. Moultos, H. Jiang, I. G. Economou, and A. Z. Panagiotopoulos, *Molecular Simulations of Thermodynamic and Transport Properties for the H_2O+NaCl System,* J. Chem. Phys. **141**, 234507 (2014).

[78] Z. Mester and A. Z. Panagiotopoulos, *Mean Ionic Activity Coefficients in Aqueous NaCl Solutions From Molecular Dynamics Simulations,* J. Chem. Phys. **142**, 044507 (2015).

[79] H. Jiang, Z. Mester, O. A. Moultos, I. G. Economou, and A. Z. Panagiotopoulos, *Thermodynamic and Transport Properties of H_2O+NaCl From Polarizable Force Fields,* J. Chem. Theory Comput. **11**, 3802 (2015).

[80] S. Plimpton, *Fast Parallel Algorithms for Short-Range Molecular Dynamics,* J. Comput. Phys. **117**, 1 (1995).

[81] S. Nosé, *A Molecular Dynamics Method for Simulations in the Canonical Ensemble,* Mol. Phys. **52**, 255 (1984).

[82] W. G. Hoover, *Canonical Dynamics: Equilibrium Phase-Space Distributions,* Phys. Rev. A **31**, 1695 (1985).

[83] P. V. Klimovich, M. R. Shirts, and D. L. Mobley, *Guidelines for the Analysis of Free Energy Calculations,* J. Comput.-Aided Mol. Des. **29**, 397 (2015).

[84] T. C. Beutler, A. E. Mark, R. C. van Schaik, P. R. Gerber, and W. F. van Gunsteren, *Avoiding Singularities and Numerical Instabilities in Free Energy Calculations Based on Mol. Simul.s,* Chem. Phys. Lett. **222**, 529 (1994).

[85] J. W. Pitera and W. F. van Gunsteren, *A Comparison of Non-Bonded Scaling Approaches for Free Energy Calculations,* Mol. Simul. **28**, 45 (2002).

[86] M. R. Shirts and V. S. Pande, *Solvation Free Energies of Amino Acid Side Chain Analogs for Common Molecular Mechanics Water Models,* J. Chem. Phys. **122**, 134508 (2005).

[87] T. Steinbrecher, D. L. Mobley, and D. A. Case, *Nonlinear Scaling Schemes for Lennard-Jones Interactions in Free Energy Calculations,* J. Chem. Phys. **127**, 214108 (2007).

[88] T. T. Pham and M. R. Shirts, *Identifying Low Variance Pathways for Free Energy Calculations of Molecular Transformations in Solution Phase,* J. Chem. Phys. **135**, 034114 (2011).

[89] M. Mezei, *The finite Difference Thermodynamic Integration, Tested on Calculating the Hydration Free Energy Difference Between Acetone and Dimethylamine in Water,* J. Chem. Phys. **86**, 7084 (1987).

[90] G. Hummer, L. R. Pratt, A. E. García, B. J. Berne, and S. W. Rick, *Electrostatic Potentials and Free Energies of Solvation of Polar and Charged Molecules,* J. Phys. Chem. B **101**, 3017 (1997).

[91] D. Frenkel and B. Smit, *Understanding Molecular Simulimulation: From Algorithms to Applications*, Vol. 1 (Elsevier (formerly published by Academic Press), 2002) pp. 1–638.

[92] S. H. Jamali, L. Wolff, T. M. Becker, M. de Groen, M. Ramdin, R. Hartkamp, A. Bardow, T. J. H. Vlugt, and O. A. Moultos, *OCTP: A Tool for On-the-Fly Calculation of Transport Properties of Fluids With the Order-n Algorithm in LAMMPS,* J. Chem. Inf. Model. **59**, 1290 (2019).

[93] D. Dubbeldam, D. C. Ford, D. E. Ellis, and R. Q. Snurr, *A New Perspective on the Order-n Algorithm for Computing Correlation Functions,* Mol. Simul. **35**, 1084 (2009).

[94] I.-C. Yeh and G. Hummer, *System-Size Dependence of Diffusion Coefficients and Viscosities From Molecular Dynamics Simulations With Periodic Boundary Conditions,* J. Phys. Chem. B **108**, 15873 (2004).

[95] M. W. Chase, *NIST-JANAF Thermochemical Tables for Oxygen Fluorides,* J. Phys. Chem. Ref. Data **25**, 551 (1996).

[96] R. Schmid, A. M. Miah, and V. N. Sapunov, *A New Table of the Thermodynamic Quantities of Ionic Hydration: Values and some Applications (Enthalpy–Entropy Compensation and Born Radii),* Phys. Chem. Chem. Phys. **2**, 97 (2000).

[97] Y. Marcus, *Ion Properties* (CRC Press, 1997).

[98] H. Friedman and C. Krishnan, *Water: a Comprehensive Treatise,* by F. Franks, Plenum Press, New York **6** (1973).

[99] G. Neilson and J. Enderby, *The Coordination of Metal Aquaions,* (Academic Press, 1989) pp. 195 – 218.

[100] T. Yamaguchi, M. Yamagami, H. Ohzono, H. Wakita, and K. Yamanaka, *Chloride-Ion Hydration in Supercritical Water by Neutron Diffraction,* Chem. Phys. Lett. **252**, 317 (1996).

[101] M. A. González and J. L. F. Abascal, *The Shear Viscosity of Rigid Water Models,* J. Chem. Phys. **132**, 096101 (2010).

[102] J. Kestin, M. Sokolov, and W. A. Wakeham, *Viscosity of Liquid Water in the Range -8 °C to 150 °C,* J. Phys. Chem. Ref. Data **7**, 941 (1978).

[103] M. W. Mahoney and W. L. Jorgensen, *Diffusion Constant of the TIP5P Model of Liquid Water,* J. Chem. Phys. **114**, 363 (2001).

[104] A. A. Chen and R. V. Pappu, *Quantitative Characterization of Ion Pairing and Cluster Formation in Strong 1:1 Electrolytes,* J. Phys. Chem. B. **111**, 6469 (2007).

[105] L. Pegado, O. Marsalek, P. Jungwirth, and E. Wernersson, *Solvation and ion-pairing properties of the aqueous sulfate anion: Explicit versus effective electronic polarization,* .

[106] E. Pluhařová, P. E. Mason, and P. Jungwirth, *Ion Pairing in Aqueous Lithium Salt Solutions With Monovalent and Divalent Counter-AnIons,* J. Phys. Chem. A **117**, 11766 (2013).

[107] R. Fuentes-Azcatl and M. C. Barbosa, *Sodium Chloride, NaCl/ϵ: New Force Field,* J. Phys. Chem. B. **120**, 2460 (2016).

[108] W. M. Haynes, *CRC handbook of Chemistry and physics* (CRC Press, 2014).

[109] W. J. Hamer and Y. Wu, *Osmotic Coefficients and Mean Activity Coefficients of Univalent Electrolytes in Water at 25°C,* J. Phys. Chem. Ref. Data **1**, 1047 (1972).

[110] C. H. Bennett, *Efficient Estimation of Free Energy Differences From Monte Carlo Data,* J. Comput. Phys. **22**, 245 (1976).

[111] J. C. Eijkel and A. Van Den Berg, *Nanofluidics: What Is It and What Can We Expect From It?* Microfluid. and Nanofluidics **1**, 249 (2005).

[112] S. Prakash, A. Piruska, E. N. Gatimu, P. W. Bohn, J. V. Sweedler, and M. A. Shannon, *Nanofluidics: Systems and Applications,* IEEE Sens. J. **8**, 441 (2008).

[113] I. C. Bourg and G. Sposito, *Molecular Dynamics Simulations of the Electrical Double Layer on Smectite Surfaces Contacting Concentrated Mixed Electrolyte (NaCl–CaCl2) Solutions,* J. Colloid Interface Sci. **360**, 701 (2011).

[114] S. Ong, X. Zhao, and K. B. Eisenthal, *Polarization of Water Molecules at a Charged Interface: Second Harmonic Studies of the Silica/Sater Interface,* Chem. Phys. Lett. **191**, 327 (1992).

[115] S. V. Patwardhan, F. S. Emami, R. J. Berry, S. E. Jones, R. R. Naik, O. Deschaume, H. Heinz, and C. C. Perry, *Chemistry of Aqueous Silica Nanoparticle Surfaces and the Mechanism of Selective Peptide Adsorption,* J. Am. Chem. Soc. **134**, 6244 (2012).

[116] F. Rancan, Q. Gao, C. Graf, S. Troppens, S. Hadam, S. Hackbarth, C. Kembuan, U. Blume-Peytavi, E. Rühl, J. Lademann, and A. Vogt, *Skin Penetration and Cellular Uptake of Amorphous Silica Nanoparticles With Variable Size, Surface Functionalization, and Colloidal Stability,* ACS Nano **6**, 6829 (2012).

[117] M. Corno, M. Delle Piane, P. Choquet, and P. Ugliengo, *Models for Biomedical Interfaces: a Computational Study of Quinone-Functionalized Amorphous Silica Surface Features,* Phys. Chem. Chem. Phys. **19**, 7793 (2017).

[118] A. Rimola, D. Costa, M. Sodupe, J.-F. Lambert, and P. Ugliengo, *Silica Surface Features and Their Role in the Adsorption of Biomolecules: Computational Modeling and Experiments,* Chem. Rev. **113**, 4216 (2013).

[119] N. Liu, Y. Hui Liu, P. Feng, L. Qiang Zhu, Y. Shi, and Q. Wan, *Enhancing the pH Sensitivity by Laterally Synergic Modulation in Dual-Gate Dlectric-Double-Layer Transistors,* Appl. Phys. Lett. **106**, 073507 (2015).

[120] M. Kosmulski, *The pH-Dependent Surface Charging and the Points of Zero Charge,* J. Colloid Interface Sci. **253**, 77 (2002).

[121] D. Argyris, N. R. Tummala, A. Striolo, and D. R. Cole, *Molecular Structure and Dynamics in Thin Water Films at the Silica and Graphite Surfaces,* J. Phys. Chem. C **112**, 13587 (2008).

[122] D. Argyris, D. R. Cole, and A. Striolo, *Dynamic Behavior of Interfacial Water at the Silica Surface,* J. Phys. Chem. C **113**, 19591 (2009).

[123] A. A. Hassanali and S. J. Singer, *Static and Dynamic Properties of the Water/Amorphous Silica Interface: a Model for the Undissociated Surface,* J. Comput. Mater. Des. **14**, 53 (2007).

[124] A. A. Hassanali and S. J. Singer, *Model for the Water-Amorphous Silica Interface: The Undissociated Surface,* J. Phys. Chem. B **111**, 11181 (2007).

[125] I. C. Bourg and C. I. Steefel, *Molecular Dynamics Simulations of Water Structure and Diffusion in Silica Nanopores,* J. Phys. Chem. C **116**, 11556 (2012).

[126] M. Collin, S. Gin, B. Dazas, T. Mahadevan, J. Du, and I. C. Bourg, *Molecular Dynamics Simulations of Water Structure and Diffusion in a 1 nm Diameter Silica Nanopore as a Function of Surface Charge and Alkali Metal Counterion Identity,* J. Phys. Chem. C **122**, 17764 (2018).

[127] C. D. Lorenz and A. Travesset, *Charge Inversion of Divalent Ionic Solutions in Silica channels,* Phys. Rev. E **75**, 061202 (2007).

[128] C. D. Lorenz, P. S. Crozier, J. A. Anderson, and A. Travesset, *Molecular Dynamics of Ionic Transport and Electrokinetic Effects in Realistic Silica Channels,* J. Phys. Chem. C **112**, 10222 (2008).

[129] N. R. Haria and C. D. Lorenz, *Ion Exclusion and Electrokinetic Effects Resulting From Electro-Osmotic Flow of Salt Solutions in Charged Silica Nanopores,* Phys. Chem. Chem. Phys. **14**, 5935 (2012).

[130] N. R. Haria and C. D. Lorenz, *Atomistic Description of Pressure-Driven Flow of Aqueous Salt Solutions Through Charged Silica Nanopores,* J. Phys. Chem. C **119**, 12298 (2015).

[131] H. Zhang, A. A. Hassanali, Y. K. Shin, C. Knight, and S. J. Singer, *The Water-Amorphous Silica Interface: Analysis of the Stern Layer and Surface Conduction,* J. Chem. Phys. **134**, 024705 (2011).

[132] T. A. Ho, D. Argyris, D. R. Cole, and A. Striolo, *Aqueous NaCl and CsCl Solutions Confined in Crystalline Slit-Shaped Silica Nanopores of Varying Degree of Protonation,* Langmuir **28**, 1256 (2012).

[133] I. C. Bourg, S. S. Lee, P. Fenter, and C. Tournassat, *Stern Layer Structure and Energetics at Mica-Water Interfaces,* J. Phys. Chem. C **121**, 9402 (2017).

[134] S. Hocine, R. Hartkamp, B. Siboulet, M. Duvail, B. Coasne, P. Turq, and J. F. Dufrêche, *How Ion Condensation Occurs at a Charged Surface: A Molecular Dynamics Investigation of the Stern Layer for Water-Silica Interfaces,* J. Phys. Chem. C **120**, 963 (2016).

[135] S. Prakash, H. A. Zambrano, K. K. Rangharajan, E. Rosenthal-Kim, N. Vasquez, and A. T. Conlisk, *ElectroKinetic Transport of Monovalent and Divalent Cations in Silica Nanochannels,* Microfluid. Nanofluid. **20**, 1 (2016).

[136] Y. Qiu and Y. Chen, *CounterIons and Water Molecules in Charged Silicon Nanochannels: the Influence of Surface Charge Discreteness,* Mol. Simul. **41**, 1187 (2015).

[137] M. Chen, D. Jiang, K. Jiang, and Y. Qiu, *Investigation of Charge Inversion in Silicon Nanochannels With Molecular Dynamics Simulation,* Proc. Inst. Mech. Eng. Part N J. Nanoeng. Nanosyst. **230**, 51 (2016).

[138] A. Sam, S. K. Kannam, R. Hartkamp, and S. P. Sathian, *Water Flow in Carbon Nanotubes: The Effect of Tube Flexibility and Thermostat,* J. Chem. Phys. **146**, 234701 (2017).

[139] K. Besteman, M. A. G. Zevenbergen, H. A. Heering, and S. G. Lemay, *Direct Observation of Charge Inversion by Multivalent Ions as a Universal Electrostatic Phenomenon,* Phys. Rev. Lett. **93**, 170802 (2004).

[140] F. H. J. van der Heyden, D. Stein, K. Besteman, S. G. Lemay, and C. Dekker, *Charge Inversion at High Ionic Strength Studied by Streaming Currents,* Phys. Rev. Lett. **96**, 224502 (2006).

[141] T. Rijnaarts, E. Huerta, W. van Baak, and K. Nijmeijer, *Effect of Divalent Cations on RED Performance and Cation Exchange Membrane Selection to Enhance Power Densities,* Environ. Sci. Technol. **51**, 13028 (2017).

[142] S. Adapa and A. Malani, *Role of Hydration Energy and Co-Ions Association on Monovalent and Divalent Cations Adsorption at Mica-Aqueous Interface,* Sci. Rep. **8**, 12198 (2018).

[143] Z. Y. Wang, P. Zhang, and Z. Ma, *On the physics of both Surface overcharging and Charge Reversal at Heterophase Interfaces,* Phys. Chem. Chem. Phys. **20**, 4118 (2018).

[144] B. W. H. van Beest, G. J. Kramer, and R. A. van Santen, *Force Fields for Silicas and Aluminophosphates Based on Ab Initio Calculations,* Phys. Rev. Lett. **64**, 1955 (1990).

[145] J. Geske and M. Vogel, *Creating realistic Silica Nanopores for Molecular Dynamics Simulations,* Mol. Sim. **43**, 13 (2017).

[146] R. L. Mozzi and B. E. Warren, *The Structure of Vitreous Silica,* J. Appl. Crystallogr. **2**, 164 (1969).

[147] J. H. Konnert and J. Karle, *The Computation of Radial Distribution Functions for Glassy Materials,* Acta Crystallogr. **29**, 702 (1973).

[148] D. I. Grimley, A. C. Wright, and R. N. Sinclair, *Neutron Scattering From Vitreous Silica IV. Time-of-Flight Diffraction,* J. Non. Cryst. Solids **119**, 49 (1990).

[149] F. S. Emami, V. Puddu, R. J. Berry, V. Varshney, S. V. Patwardhan, C. C. Perry, and H. Heinz, *Force Field and a Surface Model Database for Silica to Simulate Interfacial Properties in Atomic Resolution,* Chem. Mater. **26**, 2647 (2014).

[150] S. Halbert, S. Ispas, C. Raynaud, and O. Eisenstein, *Modelling the Surface of Amorphous Dehydroxylated Silica: The Influence of the Potential on the Nature and Density of Defects,* New J. Chem. **42**, 1356 (2018).

[151] L. T. Zhuravlev, *The Surface Chemistry of Amorphous Silica. Zhuravlev Model,* Colloids Surf., A **173**, 1 (2000).

[152] P. Ugliengo, M. Sodupe, F. Musso, I. J. Bush, R. Orlando, and R. Dovesi, *Realistic Models of Hydroxylated Amorphous Silica Surfaces and MCM-41 Mesoporous Material Simulated by Large-Scale Periodic B3LYP Calculations,* Adv. Mater. **20**, 4579 (2008).

[153] S. H. Garofalini, *Molecular Dynamics Computer Simulations of Silica Surface Structure and Adsorption of Water Molecules,* J. Non. Cryst. Solids **120**, 1 (1990).

[154] A. Comas-Vives, *Amorphous SiO_2 Surface Models: Energetics of the Dehydroxylation Process, Strain, Ab Initio Atomistic Thermodynamics and IR Spectroscopic Signatures,* Phys. Chem. Chem. Phys. **18**, 7475 (2016).

[155] J. P. Ewen, H. Gao, M. H. Müser, and D. Dini, *Shear Heating, Flow, and Friction of Confined Molecular Fluids at High Pressure,* Phys. Chem. Chem. Phys. **21**, 5813 (2019).

[156] I. C. Yeh and M. L. Berkowitz, *Ewald Summation for Systems With Slab Geometry,* J. Chem. Phys. **111**, 3155 (1999).

[157] R. T. Cygan, J.-J. Liang, and A. G. Kalinichev, *Molecular Models of Hydroxide, Oxyhydroxide, and Clay Phases and the Development of a General Force Field,* J. Phys. Chem. B **108**, 1255 (2004).

[158] M. Pouvreau, J. A. Greathouse, R. T. Cygan, and A. G. Kalinichev, *Structure of Hydrated GibbSite and Brucite Edge Surfaces: DFT Results and Further Development of the ClayFF Classical Force Field With Metal-O-H Angle Bending Terms,* J. Phys. Chem. C **121**, 14757 (2017).

[159] R. K. Mishra, A. K. Mohamed, D. Geissbühler, H. Manzano, T. Jamil, R. Shahsavari, A. G. Kalinichev, S. Galmarini, L. Tao, H. Heinz, R. Pellenq, A. C. van Duin, S. C. Parker, R. J. Flatt, and P. Bowen, *cemff: A Force Field Database for Cementitious Materials Including Validations, Applications and Opportunities,* Cem. Concr. Res. **102**, 68 (2017).

[160] J.-P. Ryckaert, G. Ciccotti, and H. J. Berendsen", *Numerical Integration of the Cartesian Equations of Motion of a System With Constraints: Molecular Dynamics of n-alkanes,* J. Comput. Phys. **23**, 327 (1977).

[161] M. A. Brown, A. Goel, and Z. Abbas, *Effect of Electrolyte Concentration on the Stern Layer Thickness at a Charged Interface,* Angew. Chemie Int. Ed. **55**, 3790 (2016).

[162] R. Rahnemaie, T. Hiemstra, and W. H. van Riemsdijk, *A New Surface Structural Approach to Ion Adsorption: Tracing the Location of Electrolyte Ions,* J. Colloid Interface Sci. **293**, 312 (2006).

[163] J. Lyklema, *Nomenclature, Symbols, Definitions and Measurements for Electrified Interfaces in Aqueous Dispersions of Solids (Recommendations 1991),* Pure Appl. Chem. **63**, 895 (1991).

[164] L. Henke, N. Nagy, and U. J. Krull, *An AFM Determination of the Effects on Surface Roughness Caused by Cleaning of FUsed Silica and Glass Substrates in the Process of Optical Biosensor Preparation,* Biosens. Bioelectron. **17**, 547 (2002).

[165] M. Rezaei, A. R. Azimian, A. R. Pishevar, and D. J. Bonthuis, *Viscous Interfacial Layer Formation Causes Electroosmotic Mobility Reversal in Monovalent Electrolytes,* Phys. Chem. Chem. Phys. **20**, 22517 (2018).

[166] A. T. Celebi, B. Cetin, and A. Beskok, *Molecular and Continuum Perspectives on Intermediate and Flow Reversal Regimes in Electroosmotic Transport,* J. Phys. Chem. C **123**, 14024 (2019).

[167] S. ben Jabrallah, F. Malloggi, L. Belloni, L. Girard, D. Novikov, C. Mocuta, D. Thiaudière, and J. Daillant, *Electrolytes at Interfaces: Accessing the First Nanometers Using X-Ray Standing Waves,* Phys. Chem. Chem. Phys. **19**, 167 (2017).

[168] D. Lis, E. H. G. Backus, J. Hunger, S. H. Parekh, and M. Bonn, *Liquid Flow Along a Solid Surface Reversibly Alters Interfacial Chemistry,* Science **344**, 1138 (2014).

[169] C. Lian, K. Xian, H. Liu, and J. Wu, *Flow Effects on Silicate Dissolution and Ion Transport at an Aqueous Interface,* Phys. Chem. Chem. Phys. **21**, 6970 (2019).

[170] B. Siboulet, S. Hocine, R. Hartkamp, and J.-F. Dufrêche, *Scrutinizing Electro-Osmosis and Surface Conductivity With Molecular Dynamics,* J. Phys. Chem. C **121**, 6756 (2017).

[171] T. M. Squires and M. Z. Bazant, *Induced-Charge Electro-Osmosis,* J. Fluid Mech. **509**, 217 (2004).

[172] R. Sadr, M. Yoda, Z. Zheng, and A. Conlisk, *An Experimental Study of Electro-Osmotic Flow in rectangular Microchannels,* Journal of fluid Mechanics **506**, 357 (2004).

[173] A. Y. Grosberg, T. T. Nguyen, and B. I. Shklovskii, *Colloquium: The physics of Charge Inversion in Chemical and Biological Systems,* Rev. Mod. Phys. **74**, 329 (2002).

[174] Y. Chen, Z. Ni, G. Wang, D. Xu, and D. Li, *Electroosmotic Flow in Nanotubes With High Surface Charge Densities,* Nano Lett. **8**, 42 (2008).

[175] S. Dewan, V. Carnevale, A. Bankura, A. Eftekhari-Bafrooei, G. Fiorin, M. L. Klein, and E. Borguet, *Structure of Water at Charged Interfaces: A Molecular Dynamics Study,* Langmuir **30**, 8056 (2014).

[176] M. Kohagen, P. E. Mason, and P. Jungwirth, *Accurate Description of Calcium Solvation in Concentrated Aqueous Solutions,* J. Phys. Chem. B **118**, 7902 (2014).

[177] M. Quesada-Pérez, E. González-Tovar, A. Martín-Molina, M. Lozada-Cassou, and R. Hidalgo-Álvarez, *Overcharging in Colloids: Beyond the Poisson-Boltzmann Approach,* ChemPhysChem **4**, 234 (2003).

[178] O. Lenz and C. Holm, *Simulation of Charge Reversal in Salty Environments: Giant overcharging?* Eur. Phys. J. E **26**, 191 (2008).

[179] I. Semenov, S. Raafatnia, M. Sega, V. Lobaskin, C. Holm, and F. Kremer, *Electrophoretic Mobility and Charge Inversion of a Colloidal Particle Studied by Singel-Colloid Electrophoresis and Molecular Dynamics Simulations,* Phys. Rev. E **87**, 022302 (2013).

[180] R. Li and B. A. Todd, *Multivalent Ion Screening of Charged Glass Surface Studied by Streaming Potential Measurements,* J. Chem. Phys. **139**, 194704 (2013).

[181] M. H. Badizad, M. M. Koleini, R. Hartkamp, S. Ayatollahi, and M. H. Ghazanfari, *How do Ions Contribute to Brine-Hydrophobic Hydrocarbon Interfaces? An in Silico Study,* J. Colloid Interface Sci. **575**, 337 (2020).

[182] B. Jeon, S. K. R. S. Sankaranarayanan, A. C. T. van Duin, and S. Ramanathan, *Atomistic Insights Into Aqueous Corrosion of Copper,* J. Chem. Phys. **134**, 234706 (2011).

[183] B. Lowe, Y. Maekawa, Y. Shibuta, T. Sakata, C.-K. Skylaris, and N. Green, *Dynamic Behaviour of the Silica-Water-bio Electrical Double Layer in the presence of a Divalent Electrolyte,* Phys. Chem. Chem. Phys. **19**, 2687 (2017).

[184] D. Bohra, J. H. Chaudhry, T. Burdyny, E. A. Pidko, and W. A. Smith, *Modeling the Electrical Double Layer to Understand the Reaction Environment in a CO_2 Electrocatalytic System,* Energy Environ. Sci. **12**, 3380 (2019).

[185] I. Siretanu, D. Ebeling, M. P. Andersson, S. S. Stipp, A. Philipse, M. C. Stuart, D. Van Den Ende, and F. Mugele, *Direct Observation of Ionic Structure at Solid-Liquid Interfaces: a Deep Look Into the Stern Layer,* Sci. Rep. **4**, 4956 (2014).

[186] T. Lagström, T. A. Gmür, L. Quaroni, A. Goel, and M. A. Brown, *Surface Vibrational Structure of Colloidal Silica and Its Direct Correlation With Surface Charge Density,* Langmuir **31**, 3621 (2015).

[187] Z. Zhang, P. Fenter, L. Cheng, N. C. Sturchio, M. J. Bedzyk, M. Předota, A. Bandura, J. D. Kubicki, S. N. Lvov, P. T. Cummings, A. A. Chialvo, M. K. Ridley, P. Bénézeth, L. Anovitz, D. A. Palmer, M. L. Machesky, and D. J. Wesolowski, *Ion Adsorption at the Rutile-Water Interface: Linking Molecular and Macroscopic Properties,* Langmuir **20**, 4954 (2004).

[188] M. S. Azam, A. Darlington, and J. M. Gibbs-Davis, *The Influence of Concentration on Specific Ion Effects at the Silica/Water Interface,* J. Phys.: Condens. Matter **26**, 244107 (2014).

[189] J. Lützenkirchen, T. Scharnweber, T. Ho, A. Striolo, M. Sulpizi, and A. Abdelmonem, *A Set-Up for Simultaneous Measurement of Second Harmonic Generation and Streaming Potential and Some Test Applications,* J. Colloid Interface Sci. **529**, 294 (2018).

[190] O. Theodoly, L. Cascão Pereira, V. Bergeron, and C. J. Radke, *A Combined Streaming-Potential Optical Reflectometer for Studying Adsorption at the Water/Solid Surface,* Langmuir **21**, 10127 (2005).

[191] P. Leroy, N. Devau, A. Revil, and M. Bizi, *Influence of Surface Conductivity on the Apparent Zeta Potential of Amorphous Silica Nanoparticles,* J. Colloid Interface Sci. **410**, 81 (2013).

[192] T. A. Gmür, A. Goel, and M. A. Brown, *quantifying Specific Ion Effects on the Surface Potential and Charge Density at Silica Nanoparticle? Aqueous Electrolyte Interfaces,* J. Phys. Chem. C **120**, 16617 (2016).

[193] S. Li, P. Leroy, F. Heberling, N. Devau, D. Jougnot, and C. Chiaberge, *Influence of Surface Conductivity on the Apparent Zeta Potential of Calcite,* J. Colloid Interface Sci. **468**, 262 (2016).

[194] Z. Brkljača, D. Namjesnik, J. Lützenkirchen, M. Předota, and T. Preočanin, *Quartz/Aqueous Electrolyte Solution Interface: Molecular Dynamic Simulation and Interfacial Potential Measurements,* J. Phys. Chem. C **122**, 24025 (2018).

[195] A. M. Darlington, T. A. Jarisz, E. L. DeWalt-Kerian, S. Roy, S. Kim, M. S. Azam, D. K. Hore, and J. M. Gibbs, *Separating the pH-Dependent Behavior of Water in the Stern and Diffuse Layers With Varying Salt Concentration,* J. Phys. Chem. C **121**, 20229 (2017).

[196] M. M. Sartin, W. Sung, S. Nihonyanagi, and T. Tahara, *Molecular Mechanism of Charge Inversion Revealed by Polar Orientation of Interfacial Water Molecules: A Heterodyne-Detected Vibrational Sum Frequency Generation Study,* J. Chem. Phys. **149**, 024703 (2018).

[197] D. Biriukov, P. Fibich, and M. Předota, *Zeta Potential Determination From Molecular Simulations,* J. Phys. Chem. C **124**, 3159 (2020).

[198] R. M. Venable, Y. Luo, K. Gawrisch, B. Roux, and R. W. Pastor, *Simulations of Anionic Lipid Membranes: Development of Interaction-Specific Ion Parameters and Validation Using NMR Data,* J. Phys. Chem. B **117**, 10183 (2013).

[199] D. Biriukov, O. Kroutil, and M. Předota, *Modeling of solid–liquid interfaces using scaled charges: Rutile (110) surfaces,* .

[200] E. Duboué-Dijon, M. Javanainen, P. Delcroix, P. Jungwirth, and H. Martinez-Seara, *A practical guide to Biologically relevant Molecular Simulations With Charge Scaling for Electronic polarization,* J. Chem. Phys. **153**, 050901 (2020).

[201] K. Szymanek, R. Charmas, and W. Piasecki, *A Study on the Mechanism of Ca^{2+} Adsorption on TiO_2 and Fe_2O_3 With the Usage of Calcium Ion-selective Electrode,* Chemosphere **242**, 125162 (2020).

[202] A. Yaroshchuk and V. Ribitsch, *Role of Channel Wall Conductance in the Determination of ζ-Potential From Electrokinetic Measurements,* Langmuir **18**, 2036 (2002).

[203] B. L. Werkhoven, J. C. Everts, S. Samin, and R. van Roij, *Flow-Induced Surface Charge Heterogeneity in Electrokinetics due to Stern-Layer Conductance Coupled to Reaction Kinetics,* Phys. Rev. Lett. **120**, 264502 (2018).

[204] A. Riese, *Adsorption of Radium and thorium onto Quartz and Kaolinite: A Comparison of Solution/Surface Equilibria Models* (Ph. D. Thesis. Colorado School of Mines, Boulder, CO., 1982).

[205] M. Karlsson, C. Craven, P. M. Dove, and W. H. Casey, *Surface Charge Concentrations on Silica in Different 1.0 M Metal-Chloride background Electrolytes and Implications for Dissolution Rates,* Aquat. Geochem. **7**, 13 (2001).

[206] A. T. Celebi and A. Beskok, *Molecular and Continuum Transport Perspectives on Electroosmotic Slip Flows,* J. Phys. Chem. C **122**, 9699 (2018).

[207] M. Laliberté and W. E. Cooper, *Model for Calculating the Density of Aqueous Electrolyte Solutions,* J. Chem. Eng. Data **49**, 1141 (2004).

[208] M. Laliberté, *A Model for Calculating the Heat Capacity of Aqueous Solutions, With Updated Density and Viscosity Data,* J. Chem. Eng. Data **54**, 1725 (2009).

[209] R. W. Hockney and J. W. Eastwood, *Computer Simulation Using Particles* (Hilger, 1989).

[210] H. Lorentz, *Über die Anwendung des Satzes vom Virial in der Kinetischen Theorie der Gase,* Ann. Phys. **248**, 127 (1881).

[211] M. Rashwan, B. Rehl, A. Sthoer, A. M. Darlington, M. S. Azam, H. Zeng, Q. Liu, E. Tyrode, and J. M. Gibbs, *Structure of the Silica/Divalent Electrolyte Interface: Molecular Insight Into Charge Inversion With Increasing pH,* J. Phys. Chem. C **124**, 26973 (2020).

[212] A. Zaragoza, M. A. Gonzalez, L. Joly, I. López-Montero, M. A. Canales, A. L. Benavides, and C. Valeriani, *Molecular Dynamics Study of Nanoconfined TIP4P/2005 Water: how Confinement and Temperature Affect Diffusion and Viscosity,* Phys. Chem. Chem. Phys. **21**, 13653 (2019).

[213] W.-L. Hsu, H. Daiguji, D. E. Dunstan, M. R. Davidson, and D. J. Harvie, *Electrokinetics of the Silica and Aqueous Electrolyte solution Interface: Viscoelectric Effects,* Adv. Colloid Interface Sci. **234**, 108 (2016).

[214] W.-L. Hsu, D. J. E. Harvie, M. R. Davidson, D. E. Dunstan, J. Hwang, and H. Daiguji, *Viscoelectric Effects in Nanochannel Electrokinetics,* J. Phys. Chem. C **121**, 20517 (2017).

[215] F. Liu, A. Klaassen, C. Zhao, F. Mugele, and D. van den Ende, *Electroviscous Dissipation in Aqueous Electrolyte Films With Overlapping Electric Double Layers,* J. Phys. Chem. B **122**, 933 (2018).

[216] H. Butt, K. Graf, and M. Kappl, *Physics and Chemistry of Interfaces* (John Wiley & Sons, 2006).

[217] L. Boltzmann, *Studien über das Gleichgewicht der lebenden Kraft,* Wiss. Abh. **1**, 49 (1868).

[218] J. Lützenkirchen, *Surface Complexation Modelling* (Elsevier, 2006).

[219] R. J. Hunter, *Zeta Potential in Colloid Science: principles and Applications*, Vol. 2 (Academic Press, 2013).

[220] W. Sutherland, *LXXV. A Dynamical Theory of Diffusion for non-Electrolytes and the Molecular Mass of Albumin,* Philos. Mag. **9**, 781 (1905).

[221] A. Einstein, *Über die von der Molekularkinetischen Theorie der Wärme Geforderte Bewegung von in Ruhenden Flüssigkeiten Suspendierten Teilchen,* Ann. Phys. **322**, 549 (1905).

[222] C. Zukoski and D. Saville, *An Experimental Test of Electrokinetic Theory Using Measurements of Electrophoretic Mobility and Electrical Conductivity,* J. Colloid Interface Sci. **107**, 322 (1985).

[223] J. Lyklema, *On the Slip Process in Electrokinetics,* Colloids Surf., A **92**, 41 (1994).

[224] S. Dukhin, *ElectroChemical Characterization of the Surface of a small Particle and nonequilibrium Electric Surface Phenomena,* Adv. Colloid Interface Sci. **61**, 17 (1995).

[225] S. Dukhin, R. Zimmermann, and C. Werner, *A Concept for the Generalization of the standard Electrokinetic Model,* Colloids Surf., A **195**, 103 (2001).

[226] F. Rubio-Hernández, F. Carrique, and E. Ruiz-Reina, *The Primary Electroviscous Effect in Colloidal Suspensions,* Adv. Colloid Interface Sci. **107**, 51 (2004).

[227] M. Ashida, M. Sasaki, H. Kan, T. Yasunaga, K. Hachiya, and T. Inoue, *Kinetics of Proton Adsorption-Desorption at TiO_2-H_2O Interface by Means of Pressure-Jump Technique,* J. Colloid Interface Sci. **67**, 219 (1978).

[228] L. R. J. Scarratt, K. Kubiak, P. Maroni, G. Trefalt, and M. Borkovec, *Structural and Double Layer Forces Between Silica Surfaces in Suspensions of Negatively Charged Nanoparticles,* Langmuir **36**, 14443 (2020).

[229] P. Ober, W. Q. Boon, M. Dijkstra, E. H. Backus, R. van Roij, and M. Bonn, *Liquid Flow Reversibly Creates a Macroscopic Surface Charge Gradient,* Nat. Commun. **12**, 4102 (2021).

[230] M. Kagan, G. K. Lockwood, and S. H. Garofalini, *Reactive Simulations of the Activation Barrier to Dissolution of Amorphous Silica in Water,* Phys. Chem. Chem. Phys. **16**, 9294 (2014).

[231] B. M. Lowe, C.-K. Skylaris, and N. G. Green, *Acid-Base Dissociation Mechanisms and Energetics at the Silica–Water Interface: An Activationless Process,* J. Colloid Interface Sci. **451**, 231 (2015).

[232] P. M. Dove and C. J. Nix, *The Influence of the Alkaline Earth Cations, Magnesium, Calcium, and Barium on the Dissolution Kinetics of Quartz,* Geochim. Cosmochim. Acta **61**, 3329 (1997).

[233] S. A. Carroll, R. S. Maxwell, W. Bourcier, S. Martin, and S. Hulsey, *Evaluation of Silica-Water Surface Chemistry Using NMR Spectroscopy,* Geochim. Cosmochim. Acta **66**, 913 (2002).

[234] M. Wilson and T. R. Walsh, *Hydrolysis of the Amorphous Silica Surface. I. Structure and Dynamics of the Dry Surface,* J. Chem. Phys. **113**, 9180 (2000).

[235] T. R. Walsh, M. Wilson, and A. P. Sutton, *Hydrolysis of the Amorphous Silica Surface. II. Calculation of Activation Barriers and Mechanisms,* J. Chem. Phys. **113**, 9191 (2000).

[236] H.-P. Cheng, R. N. Barnett, and U. Landman, *Structure, collective Hydrogen Transfer, and Formation of $Si(OH)_4$ in SiO_2-$(H_2O)n$ Clusters,* J. Chem. Phys. **116**, 9300 (2002).

[237] C. Mischler, J. Horbach, W. Kob, and K. Binder, *Water Adsorption on Amorphous Silica Surfaces: a Car-Parrinello Simulation Study,* J. Phys. Condens. Matter **17**, 4005 (2005).

[238] Y.-W. Chen and H.-P. Cheng, *Interaction Between Water and Defective Silica Surfaces,* J. Chem. Phys. **134**, 114703 (2011).

[239] A. C. T. van Duin, S. Dasgupta, F. Lorant, and W. A. Goddard, *ReaxFF: A Reactive Force Field for Hydrocarbons,* J. Phys. Chem. A **105**, 9396 (2001).

[240] T. S. Mahadevan and S. H. Garofalini, *Dissociative Water Potential for Molecular Dynamics Simulations,* J. Phys. Chem. B **111**, 8919 (2007).

[241] T. S. Mahadevan and S. H. Garofalini, *Dissociative Chemisorption of Water onto Silica Surfaces and Formation of Hydronium Ions,* J. Phys. Chem. C **112**, 1507 (2008).

[242] G. Guevara-Carrion, J. Vrabec, and H. Hasse, *Prediction of Self-Diffusion Coefficient and Shear Viscosity of Water and Its Binary Mixtures With Methanol and Ethanol by Molecular Simulation,* J. Chem. Phys. **134**, 074508 (2011).

[243] C. Bousige, P. Levitz, and B. Coasne, *Bridging Scales in Disordered Porous Media by Mapping Molecular Dynamics onto Intermittent Brownian Motion,* Nat. Commun. **12**, 1043 (2021).

[244] J. Comtet, B. Grosjean, E. Glushkov, A. Avsar, K. Watanabe, T. Taniguchi, R. Vuilleumier, M.-L. Bocquet, and A. Radenovic, *Direct Observation of Water-mediated Singel-proton Transport Between hBN Surface Defects,* Nat. Nanotechnol. **15**, 598 (2020).

Curriculum Vitæ

Max Felipe DÖPKE

11-02-1993 Born in Troisdorf, Germany.

Education

2012–2015 BSc. in Aerospace Engineering
Delft University of Technology, Delft, The Netherlands

2015–2018 MSc. in Aerospace Engineering
Delft University of Technology, Delft, The Netherlands

2018-2023 PhD. in Molecular Simulation
Delft University of Technology, Delft, The Netherlands
Thesis: Adsorption and Electrokinetics at Silica-Electrolyte Interfaces: A Molecular Simulation Study
Promotor: Prof. dr. J. T. Padding
Co-promotor: Dr. R. M. Hartkamp

List of Publications

1. **M. F. Döpke**, J. Lützenkirchen, O. A. Moultos, B. Siboulet, J. F. Dufrêche, J. T. Padding and R. Hartkamp, *Preferential adsorption in mixed electrolytes confined by charged amorphous silica*, The Journal of chemical physics, **123(27)**, 16711-16720 (2019).

2. **M. F. Döpke**, O. A. Moultos and R. Hartkamp, *On the transferability of ion parameters to the TIP4P/2005 water model using molecular dynamics simulations*, The Journal of chemical physics, **152(2)**, 024501 (2020).

3. **M. F. Döpke** and R. Hartkamp, *The importance of specifically adsorbed ions for electrokinetic phenomena: Bridging the gap between experiments and MD simulations*, The Journal of chemical physics, **154(9)**, 094701 (2021).

4. **M. F. Döpke**, F. W. van der Meij, B. Coasne and R. Hartkamp, *Surface Protolysis and Its Kinetics Impact the Electrical Double Layer*, Physical Review Letters, **128(5)** 056001 (2022).

Acknowledgements

Obtaining a PhD is the culmination journey much longer than 4 years which would not be possible without the support of family, friends, colleagues, teachers and strangers. While the new journey has already begun, I want to look back and thank all those that helped me get to this point.

First of all, I would like to thank my promotor Johan and co-promotor Remco for supporting me, guiding me and motivating me through this PhD. Without your trust and help I would not have been able to succeed. I would also like to thank you for all the feedback, all those red marked up drafts and all the critical questions on my simulations, that made me a better researcher. Thank you also for giving me the freedom to pursue my own ideas, to find my own path, to have my own failures and for being there when I needed lifting up. Remco, I also want to thank you for treating me as a friend and not just an employee or student and for being available literally 24/7 to help out. I believe I could not have gotten better supervision.

To my collaborators Otto, Johannes, Jean-François, Bertrand, Benoit, I want to thank you for all those fruitful discussions. It was a truly great experience to work with you and learn from you. I always looked forward to those unconventional coffee breaks with you Otto. They were a very welcoming distraction to my usual days. Thank you, Johannes, for showing me all those experimental techniques I had read about in real life and always being there to answer any experimental related questions.

To my colleagues and friends, thank you for making the days fun and always being there to help. Máté, thank you for all discussions and for getting me started with LAMMPS and GROMACS. I also had a lot of fun working together in supervising the molecular simulation assignment. Remco, your kindfulness is truly fascinating. You always took time to discuss ideas, gave me feedback and helped me revise presentations and papers. Thank you also for reviewing this dissertation. Alper, thank you for your incredible brain. I have never met a person with such skill to remember in which paper you read what information, and thank you for allowing me to also benefit from that skill. Also many thanks for those fantastic Turkish coffee breaks and meals. To the rest of you, Sebastian, Tim, Metin and Christos, thank you for all the discussions, jokes and we had all the nonsense that was talked about on an almost daily basis. Your presence made the days fly by. Henricus, Karlo, Karim, Peter and Val, thank you for your friendship since our first days in Delft, thank you for supporting me and standing by me during this ridiculous quest to do a PhD. To my parents, thank you for giving me all the opportunities I had when growing up and tolerating and answering all my ”why” questions. I would like to thank you for looking out for me and choosing the right school when I was a child, placing the first stones of my own path, and supporting me throughout all my choices, even when you disagreed. To my brother, you also contributed your fair share by always being

there for me, sometimes annoying, but always with brotherly love. To my friend Jorge, we spent so many hours of our life together, I cannot begin to describe how thankful I am for your friendship and how much I value that it still persists despite the distance.

To the love of my life Mandy, it would be futile to describe what you mean to me. You are always there for me and I always looked forward to sharing my experiences with you. If something good happened to me, I could never wait to tell you, and if something bad happened, I could only tolerate it, because I had you to complain to. And finally, Theodore and Elena, thank you for being my children, it goes without saying that I love you. Thank you for teaching me that joy can be found in the simplest of things.

To all those forgotten, thank you so much for having been a part of the journey that got me here and made me who I am today.